Next Generation PIRL for Surgery and Bio-Diagnostics

Dissertation
zur Erlangung des Doktorgrades
an der Fakultät für Mathematik, Informatik und Naturwissenschaften
Fachbereich Physik
der Universität Hamburg

vorgelegt von
Sebastian Alexey Joachim Kruber
aus Deggendorf

Hamburg
2018

Gutachter/innen der Dissertation:	Prof. Dr. Dwayne R.J. Miller Prof. Dr. Franz X. Kärtner
Zusammensetzung der Prüfungskommission:	Prof. Dr. Dwayne R. J. Miller Prof. Dr. Franz X. Kärtner Prof. Dr. Günter Huber Prof. Dr. Daniela Pfannkuche Dr. Andreas Maier
Vorsitzende/r der Prüfungskommission:	Prof. Dr. Daniela Pfannkuche
Datum der Disputation:	12.07.2018
Vorsitzender Fach-Promotionsausschusses:	Prof. Dr. Wolfgang Hansen
Leiter des Fachbereichs Physik:	Prof. Dr. Michael Potthoff
Dekan der Fakultät MIN:	Prof. Dr. Heinrich Graener

Abstract

Recent studies show that scar-free surgery is possible with picosecond laser pulses tuned to the strong absorption band of water in the Mid-IR. A way to generate these pulses is with an optical parametric amplifier (OPA) pumped by a picosecond infrared laser (PIRL). The PIRL that was used in the first studies was a rather expensive and high-maintenance design with a limited output power of 1.7 W. It consisted of a mode-locked oscillator with an attached regenerative amplifier. Within this work, a simple, compact and robust master oscillator power amplifier (MOPA) design is developed and tested for its viability as a next generation PIRL (NextGenPIRL). The design consists of a Q-switched Nd:YAG/Cr^{4+}:YAG based microchip laser and a two-pass Nd:YAG based crystal-fiber amplifier. Via simulations of the microchip design with a numerical model and a subsequent experimental investigation, multi-longitudinal mode behavior is identified to be responsible for a substantial deterioration of the stability of the microchip laser. Several methods to enforce single mode lasing are given and experimentally verified. The final stability-optimized Q-switched microchip laser runs in a single longitudinal mode at pulse repetition frequencies (PRF) of up to 5 kHz with a standard deviation of only 0.74% from the average pulse energy of 17.4 µJ. The pulse duration is as short as 226 ps. Together with the amplifier an output power of up to 8.2 W is achieved with an exceptional beam quality factor of 1.24. An analysis of the amplifier utilizing the Franz-Nodvik model shows that the output power is so far only limited by the available pump power. The presented MOPA laser system proofs to be a viable design for the NextGenPIRL, with the potential for being highly scalable.

Kurzzusammenfassung

Aktuelle Studien zeigen, dass bei Inzisionen in Gewebe unter Verwendung von Pikosekunden Laser Pulsen im mitteninfraroten Wellenlängenbereich eine narbenfreie Chirurgie möglich ist. Diese Laserpulse können durch einen parametrischen Verstärker (Optical Parametric Amplifier - OPA), der durch einen Pikosekunden-Infrarot-Laser (PIRL) gepumpt wird, erzeugt werden. Bei dem für die Studien verwendeten PIRL handelte es sich um ein kosten- und wartungsintensives Lasersystem, das zudem in seiner Ausgangsleistung auf 1.7 W beschränkt war. Das Lasersystem bestand aus einem modengekoppelten Oszillator mit einem nachgeschalteten regenerativen Verstärker. Gegenstand dieser Arbeit ist die Entwicklung einer neuen Generation von Pikosekundenlasern (Next Generation PIRL - NextGenPIRL), die sich durch einen kompakten Aufbau und einen stabilen und wartungsarmen Betrieb auszeichnen. Das Laserkonzept basiert zum einen auf einem gütegeschlateten Oszillator bestehend aus einem Nd:YAG/Cr^{4+}:YAG Kurzpuls-Mikrochiplaser und zum anderen auf einen Leistungsverstärker bestehend aus einer einkristallinen Nd:YAG Faser. Sowohl numerische Simulationen als auch experimentelle Untersuchungen zeigen, dass die Stabilität des Oszillators durch ein anspringen von mehreren longitudinale Moden stark beeinträchtigt wird. Es werden mehrere Verfahren und Methoden zur Mehrfachmodenunterdrückung vorgestellt und auch experimentell verifiziert. Der aus diesen Verfahren entstandene stabilitätsoptimierte Mikrochip-Laser arbeitet im Einmodenbetrieb und produziert 226 ps kurze Pulse mit einer Energie von 17.4 µJ bei einer Pulswiederhohlungsrate von 5 kHz. Die Standartabweichung der einzelnen Pulsenergien von ihrem Mittelwert liegt innerhalb von nur 0.74%. In Kombination mit dem Faserverstärker wird eine gesamte Ausgangsleistung von 8.2 W erreicht, wobei der Strahlqualitätsfaktor nicht den Wert von 1.24 überschreitet. Eine Analyse des Verstärkers unter Zuhilfenahme des von Franz und Nodvik entwickelten Verstärkermodells zeigt, dass die Ausgangsleistung des aufgebauten Systems soweit nur durch die zur Verfügung stehende Pumpleistung beschränkt ist. Das in dieser Arbeit vorgestellte Laserdesign erweist sich als vielversprechendes NextGenPIRL-Konzept mit dem Potential zu einer hohen Skalierbarkeit hin zu noch höheren Ausgangsleistungen.

Contents

Acronyms

Cr^{4+}:YAG Tetravalent Chromium doped Yttrium Aluminium Garnet

DIVE Desorption by Impulsive Vibrational Excitation

ESA Excited State Absorption

FEM Finite Element Method

FWHM Full Width at Half Maximum

IHDVE Impulsive Heat Deposition by Vibrational Excitation

KTA Potassium Titanyle Arsenate

LIDT Laser Induced Damage Threshold

MOPA Master Oscillator Power Amplifier

Nd:YAG Neodymium doped Yttrium Aluminium Garnet

NextGenPIRL Next Generation PIRL

OPA Optical Parametric Amplifier

PIRL Picosecond Infrared Laser

PRF Pulse Repetition Frequency

SA Saturable Absorber

SESAM Semiconductor Saturable Absorber Mirror

SR Strehl Ratio

VBG Volume Bragg Grating

Yb:YAG Ytterbium doped Yttrium Aluminium Garnet

Chapter 1

Introduction

1.1 From the Sun to the PIRL

The use of light as a method of tissue dissection and coagulation has a long-standing history. In 1949, long before the invention of lasers, Prof. Gerhard Meyer-Schwickrath successfully applied the method of photo-coagulation as means to halt progressive retinal detachment [1]. He collected sun light with a self-made telescope placed on the rooftop of the ophthalmic clinic at the University of Hamburg, steered it through a series of mirrors into the operating room and focused it into the eyes of the patients. After a series of successful operations, the adventurous optical construction was replaced with a high intensity vapor discharge lamp developed within a cooperation with the company Carl Zeiss. Nowadays, photo-coagulation goes beyond the field of ophthalmology [2] where the deposited heat leads to precision scars. It is also used in other medical areas like phono-surgery [3] and dermatology [4] to treat capillary malformation by selective destruction of vasculature.

Whereas Meyer-Schwickrath was using the full spectrum of the sunlight to perform the first application of photo-coagulation, vascular-selective lasers are now the preferred sources of light in treating retinal detachment and capillary malformation [5]. Blood has a high absorption in the visible spectrum due to its hemoglobin (Hb) and oxy-hemoglobin (HbO_2) content with absorption coefficients of up to $2957\,\mathrm{cm}^{-1}$ at a wavelength of 432 nm [6]. Lasers emitting monochromatic light offer the possibility to selectively address certain tissue types.

When using a laser as a tool for tissue incision or removal it is not sufficient to just ensure localized energy deposition inside the tissue. The thermally driven ablation process in soft tissues is based on a phase change of the water-content from liquid to gas. The necessary energy has to be deposited within a short period of time in order to super-heat the tissue while at the same time confining the energy inside the irradiated volume. Anderson and Parrish [5] introduced this concept of ablation under thermal confinement. They chose a laser at a wavelength that was strongly absorbed by their chosen target tissue and with a pulse duration short enough, so that thermal diffusion during the deposition of heat could be neglected.

This way, they were able to deposit energy thermally confined at their target with minimal heating of the neighboring not ablated tissue.

Most effective tissue ablation with optimized thermal confinement in the ablated volume and least perturbation to adjacent areas as possible is done nowadays with Q-switched lasers which address water as a chromophore [7]. Several processes are involved in the ablation process with nanosecond laser pulses targeted at water. Firstly, water molecules are highly absorbent in the Mid-IR, especially around 2.93 µm wavelength where three vibration modes overlap and build up to an absorption coefficient of 13,300 cm^{-1} [8]. The water starts to heat up quickly within a confined volume above its boiling point towards a metastable state [9]. At the spinodial temperature of ≈300 °C the super-heated water becomes unstable and relaxes into a mixed state of vapor and saturated liquid. The pressure of the generated vapor is in the order of 9.2 MPa, which is already high enough to rupture the inter-cellular matrix (ICM) of soft tissues. The combined process of bubble nucleation through heterogeneous nucleation and the described spinodal decomposition is referred to as phase-explosion [7].

Possible sources for a phase-explosion driven ablation are Q-switched Erbium lasers operating in the 50 to 100 ns pulse duration regime. Apritz *et al.*[10] confirmed that the pressure rise induced by spinodial decomposition is high enough to overcome the tensile strengths of soft tissues like liver, by studying the ablation plumes produced with a Q-switched Erbium laser. In case of tissues with a higher tensile strength like skin, the previously applied fluence of 1.7 J/cm^2 had to be raised to 5.1 J/cm^2 for efficient ablation. A time delay in the ablation process by several nanoseconds showed that the pressure generated from a single spinodial decomposition process was not high enough to overcome the tensile strength of skin, but it has to be performed several times to generate enough vapor pressure to rupture the tissue. A process which Vogel *et al.*[7] describe with confined boiling.

A way to increase the ablation efficiency several fold and to further minimize collateral damage to non-ablated tissue is to ablate under the condition of stress confinement [11]. The rapid heating of the irradiated tissue leads to the generation and propagation of thermoelastic stresses. Vodopyanov *et al.*[12] were the first to investigate these shock waves in water induced by 80 ps short laser pulses at 2.94 µm wavelength. Pressures of up to 2 GPa were measured, which can lead to an extra heating of the non-irradiated tissue of up to ΔT=57 °C. The extra heat facilitates the ablation process by raising the temperature at the border of the irradiated volume temporarily above the spinodial limit [7].

Dingus and Scammon [13] hypothesized that the tensile stress generated by these thermoelastic stress waves being reflected back from the tissues surface into the irradiated area can lead to tissue fracture, even if the tissue is heated below the spinodial point of water. Oraevsky *et al.*[14] showed experimentally that ablation of liver tissue is possible through stress waves generated by laser irradiation under

stress confinement, even if the temperature is raised by only 30 °C, which is far below the spinodial limit. Hence, the stress waves generated by ablation under stress confinement can rupture the tissue matrix by them self, and they have a catalytic effect on the phase explosion [7, 15].

Franjic *et al.*[16] were the first to successfully ablate tooth enamel within the regime of thermal and stress confinement with a laser targeting the vibration modes of water at 2.94 µm. Due to the high level of stress confinement the ablation threshold was as low as 0.5 J/cm^2, which is up to ten times lower than the threshold determined under thermal confinement only [17, 18, 19]. Franjic *et al.*[16] called the ablation process under stress confinement which targets the vibration modes of water the Impulsive Heat Deposition by Vibrational Excitation (IHDVE) process, which was later renamed to Desorption by Impulsive Vibrational Excitation (DIVE) [20]. The laser that generates the pulses that drive the ablation under stress confinement was called Picosecond Infrared Laser (PIRL).

Since the first experiment under the DIVE regime, several studies followed. Amini-Nik *et al.*[20] performed healing studies on mice skin. They were able to show that incisions performed with a PIRL showed substantially less damage to the extracellular matrix and to the cells surrounding the ablated volume than when performed with a surgical scalpel or a gain-switched microsecond Er:YAG laser. After nine days of wound healing the width of the remaining scar from the DIVE incision was only half of what was produced with either one of the other methods. Petersen *et al.*[21] compared PIRL incisions in rat skin with other ones performed by surgical knives. After 21 days of wound healing, the average scar width of PIRL incisions were 1.3 times smaller than in the case of blade based incisions. The scars produced by the PIRL were not visible by visual inspections, but only by microscopic analysis of stained histological sections.

Incisions performed by DIVE offer a well-defined ablation area with sharp edges. Hess *et al.*[22] ablated excised cadaver human vocal folds and performed an environmental scanning electron microscope (ESEM) analysis. The channel margins of the incisions were sharp edged and appeared rectangular. Single collagen fibers without any signs of damage were visible in the bottom layer of the ablated channel.

Several other studies showed similar results. Capillaries directly adjacent to the PIRL incisions did not show any obvious injury (Böttcher *et al.*[23, 24]). Only clinically negligible mean and peak temperature rises of 2 °C or less were seen during the DIVE driven ablation of porcine skin (Jowett *et al.*[25, 26]). Thermal effects were limited to the first layer of cells adjacent to the PIRL incision (Linke *et al.*[27]).

Today, further studies on DIVE ablation and its applications in surgery and in bio-diagnostics are performed at the clinic of the University of Hamburg (Universitäts-Klinikum Hamburg-Eppendorf, UKE) under the supervision of Prof. Dr.

Hartmut Schlüter [28, 29, 30], at the Max-Planck Institute for the Structure and Dynamics of Matter (MPSD) under the supervision of Prof. Dr. Dwayne Miller [31, 32, 33] and at the University of Toronto under the supervision of Dr. Arash Zarrine-Afsar [34, 35, 36].

1.2 Next Generation PIRL

When targeting the vibration modes of water, the stress confinement condition sets an upper limit on the laser pulse duration. The idea behind stress confinement is that stress or sound waves should not leave the irradiated volume during laser exposure. This way all generated stresses and shock waves can contribute to the ablation process either by directly rupturing the tissue or by having a catalytic effect on the phase-explosion. The simplest expression for the condition of stress confinement is given by the time that a sound wave needs to travel through the irradiated volume along the shortest distance, which is usually the penetration depth of the laser. With the speed of sound c_s and the absorption coefficient α for the laser beam in the tissue, the condition on the laser pulse duration τ_p is $\tau_p < \frac{1}{c_s \alpha}$. Soft tissue consists mostly of water, for which c_s can be estimated with 1500 m/s [37] and the absorption coefficient for light with a wavelength of 2.94 µm was measured by Bertie and Lan [8] to be 13,300 cm^{-1}. Hence, the laser pulse duration for ablation under stress confinement in the case of 2.94 µm laser radiation should not exceed 500 ps.

The second condition is that the energy density within the irradiated volume has to reach an ablation threshold. Franjic *et al.*[38] investigated DIVE by a numerical hydrodynamic modeling for the case of ablating pure water. When a laser fluence of 0.7 J/cm^2 is applied, an ≈2 µm thick layer is excited in the supercritical state with T >647.1 K and p >22.1 MPa. This supercritical volume is rapidly expanding and transforming into a liquid-vapor mixture. Deeper layers that are heated below supercritical temperatures experience large tensile stress components that can lead to a phase-explosion as described by Vogel *et al.*[9] and Vodopyanov *et al.*[12]. Hence, the ablation with DIVE consists partly of a direct transformation through homogeneous nucleation from a supercritical state into a liquid-vapor mixture within the first few micrometers of depth. Whereas in deeper layers, the ablation takes place in the form of a tensile stress assisted phase explosion with mixed homogeneous and heterogeneous nucleation events. The simulations from Franjic *et al.*[38] and the experiments on biological tissue [16] showed, that a fluence of 0.5 J/cm^2 is required for ablation within the DIVE regime.

A typical setup for DIVE driven ablation experiments consists of a PIRL with attached Optical Parametric Amplifier (OPA), some beam guiding, a focusing

lens and an electronically driven steering mirror to scan the laser beam along the chosen tissue (see Petersen *et al.*[21]). The beam quality factor of the 2.94 µm wavelength beam after the OPA is typically M^2 ≈5, the beam before the lens is widened up to 10 mm in diameter in order to increase the focusability and the working distance between the lens and the tissue is approximately 10 cm. To reach the necessary fluence of 0.5 J/cm^2, the laser pulse has to have an energy of at least 137 µJ. With the OPA working typically at 10 % conversion efficiency from the pump to the idler, the minimum pulse energy for a PIRL is 1.37 mJ.

For the first experimental investigations of the DIVE process a laser system has been setup by Franjic *et al.*[16] consisting of an oscillator, amplifier and an OPA. The mode-locked Nd:YLF based oscillator produced 100 ps pulses with 3 nJ of pulse energy. Single pulses have been selected at 1 kHz Pulse Repetition Frequency (PRF) by a pulse-picker and then amplified by a regenerative amplifier to 1.7 mJ resulting in a slightly longer pulse length of 140 ps. The wavelength conversion to the Mid-IR was implemented with a Potassium Titanyle Arsenate (KTA) based OPA with collinear type-II phase matching. The OPA was seeded by a fiber coupled distributed feedback (DFB) diode laser and the resulting idler pulses had a wavelength of 2.96 µm and a pulse energy of 170 µJ at a PRF of 1 kHz. The pulse duration of the idler was 105 ps.

The laser operated within the DIVE regime. Its pulse energy with 170 µJ was high enough to reach ablation threshold and the pulse duration was shorter than the stress relaxation time of 500 ps in water. But with the given output power of 0.17 W, only small incisions could be made and only low ablation rates could be achieved [20]. For advanced medical procedures and experiments, the need came up for a laser system with a higher output power, that is also easier to maintain than a system with a regenerative amplifier and a mode-locked oscillator.

A possible route is the usage of a simple and robust Q-switched microchip laser, that produces pulses with a length of 100 ps to 400 ps and with a pulse energy that is high enough to be amplified to the mJ-level with only one double-pass amplifier. This kind of low-maintenance system would offer the advantage of long-term stability without the need for re-alignment. It would also be very cost-effective as the oscillator basically consists of a single bonded crystal with no other optics and the amplifier does not need an electro-optic device. This design could also be made very compact, so that the transport between the lab and the medical clinic would be easy to accomplish.

Commercial Master Oscillator Power Amplifier (MOPA) systems producing 100 ps to 400 ps pulses with energies in the mJ-range at kHz repetition frequency are hard to find. The product portfolio of Coherent Inc. (Santa Clara, USA) includes several laser systems producing very short pulses in the 1 ps to 10 ps range with several Watts of output power. But their pulse energy does not reach the mJ-level. Their pulse energy of a few 10 µJ are already high enough to achieve

optical breakdown in metal or glass for plasma driven ablation, which is what they are designed for. The company also offers Q-switched MOPA systems producing pulses with an energy of several mJ and average output powers of up to 80 W. These designs preliminary are used to pump other laser sources like Titanium doped Sapphire lasers or optical parametric oscillators, that cannot be continuously pumped as they have either short upper laser level lifetimes in their gain material or short photon lifetimes in their cavity. Hence, these designs are optimized towards producing high pulse energies while the pulse durations can be as long as several nanoseconds. Due to the lack of applications, there is a gap in available laser sources between the two described laser designs.

The aim of this thesis is to fill this gap, by implementing a Master Oscillator Power Amplifier (MOPA) design that produces pulses with a few-100 ps in duration and energies in the mJ-range, with the application being DIVE based ablation. Limitations and laser effects appearing in that design are identified and scaling capabilities for this new laser design named the Next Generation PIRL (NextGenPIRL) are investigated.

- The route to the NextGenPIRL starts with a brief introduction into the laser theory within chapter 2. The presented theory is referred to throughout this work.
- An overview of implemented Q-switched microchip designs found in literature will be given in chapter 3. The most promising design is chosen as a proposed new oscillator for the NextGenPIRL.
- The proposed microchip laser is investigated in detail, first by probing it in simulations within chapter 4. The model to simulate the laser is based on the rate equations derived in the theory chapter. Several effects like multi-longitudinal mode lasing and temperature dependent emission cross sections are added to the model and the influences of these effects on the laser's performance are explained in detail.
- Finally, the proposed microchip laser is set up and tested experimentally (chapter 5). The measured laser pulse characteristics are compared to simulations. Especially the stability and the appearing multi-mode effects are investigated in detail with respect to the predictions from the simulation and to results reported in the literature.
- Several approaches to enhance the stability of the microchip laser are explained in chapter 6. Two new microchip lasers are presented, which are designed according to these stability optimization guidelines.

- In the end, a novel crystal-fiber based two-pass amplifier is presented that brings the pulses from the stability optimized microchip laser to the several-Watt level (chapter 7). It is revealed if the criteria for the NextGenPIRL are met with the proposed MOPA design. The chapter ends with a concept to scale the amplifier to higher output powers without increasing the thermal load.

Chapter 2

Laser Theory

In the following chapter a brief overview of the laser theory is described. After a short introduction of the stimulated emission, a set of rate equations will be formulated to describe photons within a laser cavity. Laser modes will be described together with the effect of thermal lensing. This chapter will end with both rate equations and laser mode description for Q-switched microchip lasers.

2.1 From Einstein to the Rate Equations

2.1.1 Einstein's Stimulated Emission

According to quantum mechanics a molecule has a discrete set of eigenstates Z_n with inner energy E_n. In 1916 Albert Einstein proposed a hypothesis for energy transfer between molecules seen as Planck-Resonators and an electromagnetic field [39]. In the first case of 'Ausstrahlung' (emission) a molecule in the state Z_m can emit the radiant energy $E_m - E_n$ with the frequency ν without any external stimulus by changing its state to Z_n. The probability dW for this process to occur within a time period dt is

$$dW = A_{mn}dt \tag{2.1}$$

with the Einstein coefficient A_{mn} for spontaneous emission. With the sum over all possible end-states Z_n a radiative lifetime τ_m analog to the lifetime of a radioactive decay can be defined as

$$\tau_m = \frac{1}{A_m} \qquad \text{with} \qquad A_m = \sum_n A_{mn} \tag{2.2}$$

In the second case called 'Einstrahlung' (irradiation) an energy transfer between an existing electromagnetic field and a Planck-Resonator leads to a change of the energy state of the resonator. This energy transfer is valid for both directions $Z_m \leftrightarrow Z_n$. Analog to the spontaneous emission, this 'Zustandsänderung durch Einstrahlung' can be described as a probability dW over the time period dt

with the radiation density ρ and the Einstein coefficients for absorption B_{nm} and stimulated emission B_{mn}.

$$dW = B_{nm}\rho dt \tag{2.3}$$
$$dW = B_{mn}\rho dt \tag{2.4}$$

In the figure 2.1 all three processes are shown schematically.

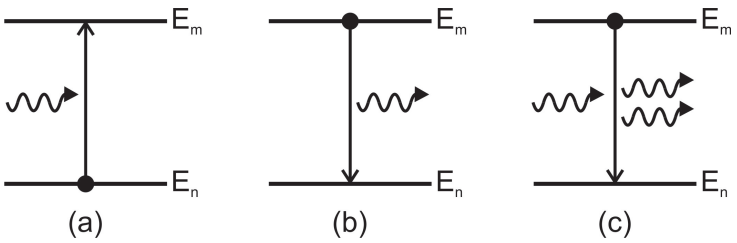

Figure 2.1: *Schematic drawing of absorption (a), spontaneous emission (b), stimulated emission (c)*

Planck's law can be deduced from these simple assumptions, which will arise in the relations between the Einstein coefficients. The equation for a canonical ensemble with the probability W_n to find the molecule in the state Z_n is

$$W_n = g_n e^{-\frac{E_n}{kT}} \tag{2.5}$$

with the Boltzmann constant k and a weighting factor g_n which can be interpreted as a degeneracy factor. Assuming that a system with energy transfer between a radiant field and molecules is in equilibrium when there are as many absorption processes as spontaneous and stimulated emissions it can be said that

$$g_n e^{-\frac{E_n}{kT}} B_{nm}\rho = g_m e^{-\frac{E_m}{kT}} (B_{mn}\rho + A_{mn}) \tag{2.6}$$

If the radiation density should approach infinity together with the temperature, the Einstein coefficients of absorption and stimulated emission only differ through their states degeneracy factor.

$$g_n B_{nm} = g_m B_{mn} \tag{2.7}$$

From the said condition of equilibrium Planck's law arises, which can be seen as a confirmation of Einsteins model.

$$\rho = \frac{\frac{A_{mn}}{B_{mn}}}{e^{\frac{E_m - E_n}{kT}} - 1} \tag{2.8}$$

Together with the known Planck's law [40] and the 'Lichtenergiequantum' (photon's energy) $E_{ph} = E_m - E_n = h\nu$, the velocity of light $c_n = cn$ in an optical medium with refractive index n the relation between spontaneous and stimulated emission is revealed.

$$\frac{A_{mn}}{B_{mn}} = \frac{8\pi h\nu^3 n^3}{c^3} \tag{2.9}$$

2.1.2 Emission Cross Section

The differential equations 2.4 can be combined to describe absorption and stimulated emission for homogeneously distributed ions which can only be in two discrete degenerate eigenstates and a homogeneous radiation density. The ion density of the lower state is denoted as n_0 and for the upper state n_1. The radiation density consists of photons all having the same frequency ν_{10}, which corresponds to the energy difference between ion state 1 and 0.

$$\frac{dn_1}{dt} = \rho(B_{01}n_0 - B_{10}n_1) = \rho B_{10}(\frac{g_1}{g_0}n_0 - n_1) \tag{2.10}$$

Equation 2.10 describes transitions between the upper and the lower level, due to stimulated emission and absorption. For each electron transition from the upper level 1 to the lower level 0 one photon is emitted and the energy density ρ gains one photon with energy $h\nu$, whereas in case of absorption one photon of the same energy is annihilated. This can be written in form of a differential equation for the radiation density by

$$\frac{d\rho}{dt} = \rho B_{10} h\nu(n_1 - \frac{g_1}{g_0}n_0) \tag{2.11}$$

At this point the radiation density ρ and the Einstein coefficient are not frequency dependent. The energy levels of the eigenstates are seen as discrete and the emitted light is seen as monochromatic with the energy $h\nu_{10}$. In many laser gain media the ions are embedded in a medium. The interaction between the host medium and the ions deform the transition spectrally, thus the transition is not limited to a fixed energy $h\nu_{10}$ anymore. The deformation or broadening can be described with a normalized line-shape function $g(\nu)$ and equation 2.11 becomes

$$\frac{d\rho(\nu)}{dt} = \rho(\nu)B_{10}g(\nu)h\nu(n_1 - \frac{g_1}{g_0}n_0) \quad \text{with} \quad \int g(\nu)d\nu = 1 \tag{2.12}$$

This more realistic description allows a frequency dependent radiation density. But of course for any interaction to happen the line-shape factor $g(\nu)$ at the frequency ν should be non-zero.

At this point the stimulated emission cross section $\sigma_{10}(\nu)$ can be introduced as a replacement for the Einstein-coefficient for stimulated emission. With using the Einstein-relation (equation 2.9) it can then be rewritten in terms of spontaneous emission

$$\begin{aligned} \sigma_{10}(\nu) &= \frac{h\nu g(\nu) B_{10}}{c} \\ \sigma_{10}(\nu) &= \frac{A_{10} c^2}{8\pi n^2} g(\nu) \end{aligned} \tag{2.13}$$

2.1.3 Population Inversion

In the last section two rate equations were derived for the interaction between radiation described by a radiation energy density and an optically active material described by two possible energy states with densities n_0 and n_1. When no external energy source is applied, the system will progress towards an equilibrium state between absorption and stimulated emission until, according to equation 2.12 and in case of identical degeneracies for the two states, the populations of the upper and the lower state are identical. At this point no further amplification, which is seen as the difference between absorption and stimulated emission, will occur. For amplification to occur, the difference between the ions being in the upper state to the ions being in the lower state has to be positive and that difference is called the population inversion density Δn.

There are several ways to fill up the upper state again or continuously. One is the use of a light source, the pump light, which pumps energy back into the system by absorption. The pump light can be incoherent, but due to the stimulated emission being phase-preservative, the generated or amplified photon field is coherent. Such a system can be seen as a converter for incoherent to coherent light and it belongs to the category of devices for Light Amplification by Stimulated Emission of Radiation or short LASER.

In a two-level system the pump light will have to have the same frequency as the generated radiation, so the incoherent pump light would not just pump energy into the system, but also extract energy due to stimulated emission. One way to circumvent pump light amplification is three and four level based ion transitions. In a three level system (see figure 2.2), a third energy level exists with energy E_3, which is slightly above the upper level with energy E_2. The pump light with frequency ν_{03} will excite electrons from the lower level with energy $E_0 = 0$ to the so called pump band. From here the ion needs to have a fast relaxation into the upper level, which in turn needs a slow relaxation into the lower level or better said a long lifetime. What the pump light effectively does is repopulating the upper state within the medium without influencing the wanted radiation density

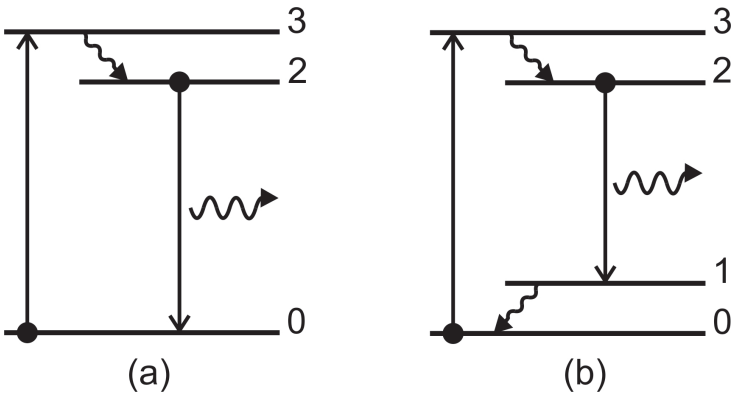

Figure 2.2: *Schematic drawing of energy levels of a three level laser (a) and a four level laser (b)*

with the frequency ν_{20}. This way a system is found that can transform incoherent to coherent light.

In a four level laser (see figure 2.2) another level appears right above the ground level, which is the new lower laser level. The lowest level is then called the ground level with energy E_0, and the new lower laser level has the energy E_1. Starting from the ground level, the pump light with frequency ν_{03} excites electrons into the pump band with energy E_3, and the quickly relaxes into the upper laser level with energy E_2. The transition from the second to the first level corresponds to the stimulated emission with radiation frequency $\nu_{21} = \frac{E_2 - E_1}{h}$. From the lower laser level a fast relaxation back to the ground level completes the cycle.

A four level laser can be advantageous because the lower laser level is never populated, thus the population inversion is always the population density of the upper laser level. No or close to no re-absorption from the lower n_1 level to the upper level n_2 occurs within the medium. But this is only the case, if the relaxation rate from the lower laser level to the ground level is infinite. The case where the lower laser level has a finite non-zero lifetime will be addressed in detail later.

2.1.4 Rate Equations

In order to make use of the stimulated emission, a laser typically consists of a gain medium with length l_g placed between two mirrors. One mirror is highly reflective for the laser wavelength, whereas the second mirror is partially reflective with a reflectivity of R_{oc}. The second mirror is also called the output coupling mirror as it couples a part of the laser light out of the cavity. The photon energy density from chapter 2.1 can be rewritten as the photon density ϕ with $\phi = \frac{\rho}{h\nu}$ and the rate

equations 2.10 and 2.12 can be written for a four level system as

$$\frac{dn_g}{dt} = \sigma_g c \phi n_g \tag{2.14}$$

$$\frac{d\phi}{dt} = \frac{\phi}{t_{rt}}(2\sigma_g n_g l_g - ln(1/R_{oc})) \tag{2.15}$$

Here it was assumed that each photon in the cavity passes the gain medium two times each round trip which takes t_{rt} seconds. The population of the upper laser level was defined as n_g and the lower laser level was assumed to be empty due to an infinite depopulation rate. Furthermore, each round trip the fraction $ln(1/R_{oc})$ of the photons is coupled out of the cavity. These rate equations will be the basic equations to describe q-switched microchip laser.

2.2 Laser Modes in an Optical Resonator

An optical resonator can be seen as a system in which light beams are traveling forth and back between two mirrors and in between through several optical elements. The circulating beams lose on the one hand energy due to diffraction on the optical elements and due to absorption in the optical elements or just by bouncing out of the resonator. On the other hand they gain energy due to stimulated emission when they pass through a gain medium. The beams inside the resonator which survive these processes and resonate forth and back are the modes of an optical resonator. In this chapter only stable standing wave resonators are treated. A good review of the theory of laser beams and resonators can be found from Kogelnik and Li [41].

2.2.1 Longitudinal Modes

In order for the laser resonator to work, several conditions have to be fulfilled, one of which is the frequency condition. Much like in a Fabry-Perot resonator, the only frequencies that exist are those that form a standing wave and thus interfere positively with each other. In mathematical terms, only those frequencies ν within the resonator of optical length L_{opt} can exist, which satisfy the round trip phase-condition $\phi(\nu) = 2\pi\nu \times \frac{2L_{opt}}{c} = 2\pi \times q$ with integers q. Hence, the possible frequencies within a standing-wave resonator are given by

$$\nu_q = q \times \frac{c}{2L_{opt}}, \qquad q = integer. \tag{2.16}$$

These longitudinal modes form a frequency comb with equally spacing of $\Delta\nu = \frac{c}{2L_{opt}}$. Figure 2.3 shows the electric field intensity of three adjacent longitudinal modes. They are all in phase close to the cavity end-mirrors, but start to de-phase when deviating away from the mirrors. The two adjacent axial modes (q) and $(q+1)$ are exactly out of phase at the resonators center. The two next-neighbors (q) and $(q+2)$ are completely out of phase at a quarter resonator length away from each end-mirror, and in phase at the center of the cavity.

2.2.2 Transversal Modes

For an accurate description of light beams within a resonator, the wave nature of light including diffraction effects have to be taken into account. An electromagnetic field in free space can be described by the scalar wave equation. For monochromatic waves with a wavelength of λ and a wavenumber of $k = 2\pi/\lambda$ the scalar wave equation reduces to the Helmholtz equation

$$[\nabla^2 + l^2]\tilde{E}(x, y, z) = 0 \tag{2.17}$$

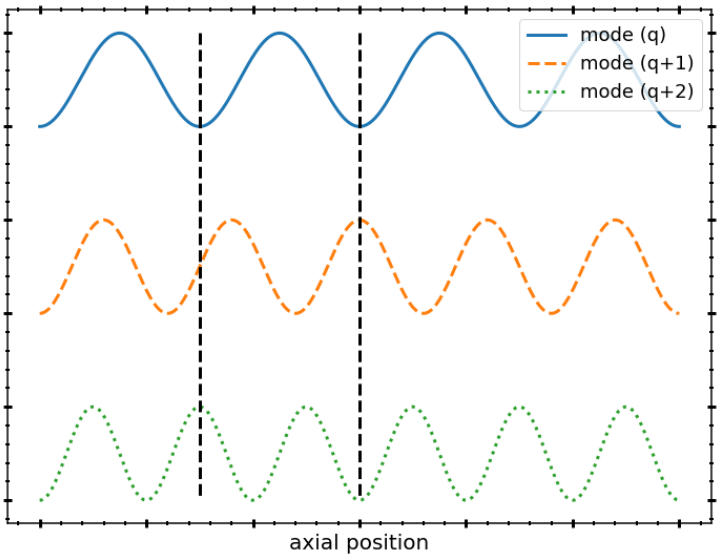

Figure 2.3: *Electric field intensities of three neighboring resonator modes between two end-mirrors. Dashed lines mark the cavity center and the first quarter. Intensities of mode q and $q+1$ are out of phase at the center. Intensities of mode q and $q+2$ are out of phase at the first and last quarter.*

with an electric field distribution $\tilde{E}(x,y,z)$ that oscillates in time. Common laser setups generate light beams that circulate along an optical axis where the width of the light beam is relatively narrow compared to the length of the resonator. These beams are well collimated and can be treated with the paraxial approximation. In the paraxial wave approximation the spatial variation in the electric field $\tilde{E}(x,y,z)$ of a wave propagating along an optical axis z is primarily given by a spatial period $k = 2\pi/\lambda$ of one wavelength λ together with a slowly varying complex wave amplitude $\tilde{u}(x,y,z)$:

$$\tilde{E}(x,y,z) = \tilde{u}(x,y,z)e^{ikz} \tag{2.18}$$

When it is assumed that the amplitude $\tilde{u}$ varies so slowly with z that its second derivatives $\partial^2\tilde{u}/\partial z^2$ can be neglected, the wave equation 2.17 reduces to the paraxial wave equation

$$\frac{\partial^2\tilde{u}}{\partial x^2} + \frac{\partial^2\tilde{u}}{\partial y^2} - 2ik\frac{\partial\tilde{u}}{\partial z} = 0. \tag{2.19}$$

The simplest solution to the paraxial wave equation is a spherical wave originating at the point (x_0, y_0, z_0) with wavefront curvature radius $R(z) = R_0 + z - z_0$

$$\tilde{u}(x,y,z) = \frac{1}{R(z)}exp\left[-ik\frac{(x-x_0)^2+(y-y_0)^2}{2R(z)}\right]. \tag{2.20}$$

The crux about this solution is that it extends out to infinity for every plane along the optical axes, and there can only be a finite amount of energy within a real laser resonator. Another solution for the paraxial wave equation can be obtained when the radius of curvature in the spherical wave is replaced by a complex variable which is called the beam propagation factor $\tilde{q}(z) = \tilde{q}_0 + z - z_0$. Both the propagation factor and the exponent in the solution for the spherical wave can be separated in an imaginary and a real component.

$$\frac{1}{\tilde{q}(z)} = \frac{1}{q_r(z)} - i\frac{1}{q_i(z)} \tag{2.21}$$

$$\tilde{u}(x,y,z) = \frac{1}{\tilde{q}(z)} exp\Bigg[- ik\frac{x^2+y^2}{2q_r(z)} - k\frac{x^2+y^2}{2q_i(z)} \Bigg] \tag{2.22}$$

The first and imaginary term in the exponent looks like the exponent in the solution for the spherical wave and $q_r(z)$ can be interpreted again as the radius of curvature with $q_r(z) = R(z)$. The second and real term in the exponent is quadratic and when separated from the first term it resembles a Gaussian profile with a radius of $w^2(z) = \frac{\lambda}{\pi} q_i(z)$. The new solution with complex beam propagation factor is called a Gaussian spherical wave and it can be written as

$$\tilde{u}(x,y,z) = \frac{1}{\tilde{q}(z)} exp\Bigg[- ik\frac{x^2+y^2}{2R(z)} - \frac{x^2+y^2}{w^2(z)} \Bigg] \tag{2.23}$$

The Gaussian spherical wave retrieved from the spherical wave describes the fundamental or Gaussian transverse mode of a laser beam with a beam waist of $w(z)$ and a wavefront radius of curvature of $R(z)$ that propagates along the optical axes z. The propagation of such a beam can entirely be handled with its propagation factor $\tilde{q}(z)$. There are more solutions to the paraxial wave equation, which represent the higher order transversal modes of a laser resonator.

Now that we have a description for the transverse profile of a laser beam, we are one step away of describing the transversal mode in a laser resonator. As already mentioned, the propagation factor q contains the information of the laser mode width ω and wavefront curvature R by its definition

$$\frac{1}{\tilde{q}(z)} = \frac{1}{q_r(z)} - i\frac{1}{q_i(z)} \tag{2.24}$$

$$= \frac{1}{R(z)} - i\frac{\lambda}{\pi\omega^2(z)} \tag{2.25}$$

When a Gaussian beam with a propagation factor q_1 propagates through a paraxial element described by the matrix $M = \left(\begin{smallmatrix} A & B \\ C & D \end{smallmatrix}\right)$, the Gaussian beam after the element can again be described by its new beam propagation factor q_2. The law of

transformation is

$$q_2 = \frac{Aq_1 + B}{Cq_1 + D} \tag{2.26}$$

In the case of a standing wave oscillator with several optical elements M_n, we are looking for a stable mode that is self-consistent after each round trip. We start from a reference plane at $z = 0$ where the laser mode has some propagation factor q_1. One laser cavity round trip can be described with one single matrix M. After one round trip, the laser mode should be self-consisted, or

$$q_2 = \frac{Aq_1 + B}{Cq_1 + D} = q_1 = q \tag{2.27}$$

This equation can be rewritten in a quadratic form over $\frac{1}{q}$ with two solutions q_a, q_b with

$$\frac{1}{q_a}, \frac{1}{q_b} = \frac{D - A}{2B} \pm \frac{1}{B}\sqrt{\left(\frac{A + D}{2}\right)^2 - 1} \tag{2.28}$$

From these equations we can derive a criteria for a paraxial resonator to have a stable Gaussian mode solution, with

$$\left|\frac{A + D}{2}\right| < 1 \tag{2.29}$$

The fundamental Gaussian transversal laser mode in a stable paraxial resonator can be easily retrieved with equation 2.28 and the stability criteria 2.29. More solutions to the paraxial wave equation can be found within the textbooks of Siegman [42] and Köchner [43].

2.3 Thermal Lensing

Optically transparent solid-state materials like glass and laser crystals change their refractive index with temperature. This effect can be described with the coefficient for temperature dependent refractive index (dn/dT). Within this work, diode end-pumped and side-cooled crystals are employed as laser gain media. For this case it is reasonable to assume that the laser pump is absorbed along the optical axes (see figure 2.4) and a thermal gradient forms with $\Delta T(r,z) = T(r,z) - T(r_0,z)$, where r is the distance from the optical axes z and r_0 is the crystal's radius. This starting point was used by Koechner [44] and Innocenzi [45] to derive a formulation for the focal length, which is described in detail in this chapter.

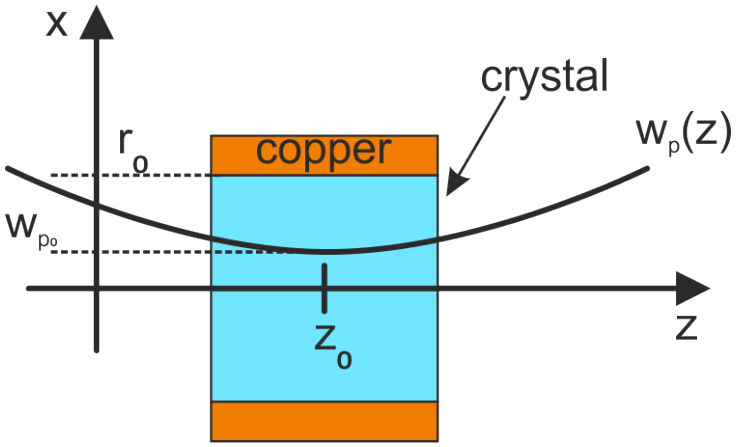

Figure 2.4: *Schematic drawing of an end-pumped cylindrical crystal with radius r_0, side cooled with a copper heat sink, pump mode has a radius of $w_p(z)$ with beam waist $w_{p,0}$ at position z_0.*

In order to obtain the temperature distribution $T(r,z)$ within the crystal the Poisson equation has to be solved. Within this work only side-cooled crystals are used, thus a good assumption is to see the heat-flow within the crystal as radial-only. Hence, the Poisson equation can be written with the thermal conductivity K_c and the deposited heat $Q(r,z)$ as

$$\nabla^2 T(r,z) = -\frac{Q(r,z)}{K_c} = \frac{\partial^2}{\partial r^2} T(r,z) + \frac{1}{r}\frac{\partial}{\partial r} T(r,z) \tag{2.30}$$

The boundary conditions are: Constant temperature T_0 on the side-face of the cylindrical crystal with radius r_0, radial-symmetric temperature profile with the maximum temperature in the center at $r = 0$, no cooling at the end-faces at

$z = 0, l$.

$$T(r_0, z) = T_0, \quad \left.\frac{\partial T(r,z)}{\partial r}\right|_{r=0} = 0, \quad \left.\frac{\partial T(r,z)}{\partial z}\right|_{z=0,l} = \infty \tag{2.31}$$

The deposited heat $Q(r, z)$ is the heat fraction η_h of the absorbed pump power $P_{p,abs}(r, z)$ per volume.

$$Q(r,z) = \frac{dP_{heat}(r,z)}{dV} = \eta_h \frac{dP_{p,abs}(r,z)}{dV} \tag{2.32}$$

With $dP/dV = dI/dz$ and $dP_{p,trans}/dz = -dP_{p,abs}/dz$ the deposited heat can also be described in terms of transmitted pump intensity $I_{p,trans}(r, z)$

$$Q(r,z) = -\eta_h \frac{dP_{p,trans}(r,z))}{dV} = -\eta \frac{dI_{p,trans}(r,z)}{dz} \tag{2.33}$$

The heat fraction η_h is the fraction of the absorbed pump power that is converted to heat. A possible assumption is that in a four level laser, each absorbed pump photon with a wavelength of λ_p generates one emission photon with a wavelength of λ_l and the rest is converted into phonons. The heat fraction then is

$$\mu_h = 1 - \frac{\lambda_p}{\lambda_e}. \tag{2.34}$$

A more comprehensive description of the heat fraction is given in [46] where not only lasing but also florescence decay is taken into account.

The intensity of a Gaussian pump beam transmitted through the crystal can be written as

$$I_{p,trans}(r,z) = \frac{2P_{p,0}}{\pi\omega_p^2(z)} e^{-\frac{2r^2}{\omega_p^2(z)}} e^{-\alpha_p z}, \tag{2.35}$$

with an initial power of the pump beam of $P_{p,0}$, an absorption coefficient of α_p and a pump mode radius of $\omega_p(z)$. The pump mode itself is assumed to have a Gaussian beam profile with a beam quality factor M_p^2 and it is focused at position z_0 with a waist radius of ω_{p0}.

$$\omega_p^2(z) = \omega_{p0}^2 \left[1 + \left(\frac{M_p^2 \lambda_p (z - z_0)}{\pi n \omega_{p0}^2}\right)^2\right] \tag{2.36}$$

Solving the differential equation 2.30 with the given parameters and the boundary conditions 2.31, the temperature distribution is

$$\Delta T(r,z) = \eta_h P_{p,0} \frac{\alpha_p e^{-\alpha_p z}}{4\pi K_c} \left[ln\left(\frac{r_0^2}{r^2}\right) + E_1\left(\frac{2r_0^2}{\omega_p^2(z)}\right) - E_1\left(\frac{2r^2}{\omega_p^2(z)}\right)\right] \tag{2.37}$$

where E_1 is the exponential integral function defined as

$$E_1(x) = \int_1^\infty \frac{e^{-xt}}{t} dt. \tag{2.38}$$

The thermal gradient induces an optical path difference OPD(r) orthogonal to the optical axes. The three dominant terms are the change in refractive index with temperature described by the coefficient dn/dT, the thermal expansion of the crystal with the according coefficient of thermal expansion α_T, the bulging of the end-faces due to the expansion of the crystal. The OPD distribution within the pumped crystal then is

$$\frac{d\text{OPD}(r,z)}{dz} = \left[\frac{dn}{dT} + 2C_r n^3 \alpha_T + (n-1)(1+\nu_p)\alpha_T)\right] \Delta T(r,z) \tag{2.39}$$

where C_r is the photo-elastic coefficient, n is the refractive index, ν_p is the Poisson ratio. If the cavities end-mirror is coated on the crystals end-face, the term $(n-1)$ has to be replaced by n.

The total optical path difference can be calculated by inserting equation 2.37 into 2.39 and integrating along the optical axes ($z = 0..l$). In order to simplify the integration the pump beam radius $w_p(z)$ can be assumed to be constant within the crystal and set as $w_{p,avg}$. The total path difference can be written as

$$\text{OPD}(r) = A_0 \times \left[ln\left(\frac{r_0^2}{r^2}\right) + E_1\left(\frac{2r_0^2}{\omega_{p,avg}^2}\right) - E_1\left(\frac{2r^2}{\omega_{p,avg}^2}\right)\right] \tag{2.40}$$

with the parameter

$$A_0 = \frac{\eta_h P_{p,0}}{4\pi K_c (1-e^{-\alpha_p l})} \times \left[\frac{dn}{dT} + (n-1)(1+\nu_p)\alpha_T + 2C_r n^3 \alpha_T\right] \tag{2.41}$$

To get the thermal lens from equation 2.40, it can be expanded into a power series. On the other side, the OPD of an ideal lens with focal length f is parabolic.

$$\text{OPD}_f(r) = -\frac{r^2}{2f} + \text{OPD}_0. \tag{2.42}$$

Considering only the quadratic term from 2.40 and using 2.42 the focal length of the thermal lens can be approximated with

$$f = \frac{\omega_{p,avg}^2}{4A_0}. \tag{2.43}$$

This equation is used very often as it is simple and precise enough for most cases. It shall be referred to as the parabolic approximation of the thermal lens.

2.3.1 Strehl-Ratio Corrected Focal Length

As can be seen in figure 2.5, the parabolic term from the power series of the equation 2.40 is dominant only for small radii ($r << \omega_{p,avg}$). This approximation is thus only valid for small laser mode radii ($\omega_l << \omega_{p,avg}$). In most laser setups the radius of the laser mode is comparable to the radius of the pump mode and the approximation brings a considerate error with it.

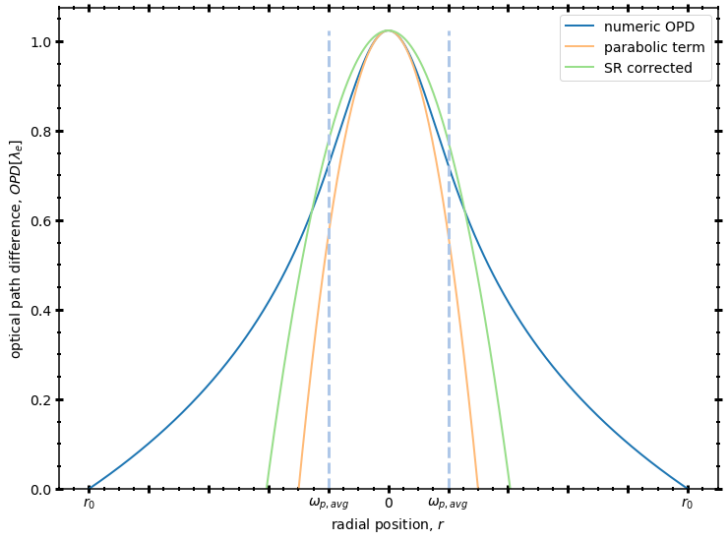

Figure 2.5: *Optical path difference (OPD) for an end-pumped laser crystal. OPD values are given in units of the lasing wavelength λ_e. The average pump mode radius is $\omega_{p,avg}$. The numeric OPD(r) and the parabolic approximation OPD$_f(r)$ coincide only for small radii ($r << \omega_{p,avg}$).*

According to the diffraction theory [47] the focus of a light beam is where the normalized intensity is at its maximum. As the laser mode is aberrated by the thermal lens, there might be a more precise way to approximate the thermal lens than by just looking at the second order terms. By definition, the Strehl Ratio (SR) of a beam is the ratio of the peak aberrated image intensity compared to the maximum attainable intensity using an ideal optical system limited only by diffraction over the system's aperture. The SR without an aperture is defined as

$$SR = \langle e^{i2\pi\Delta\varphi/\lambda_l} \rangle, \tag{2.44}$$

where λ_l is the beam's wavelength and $\Delta\varphi$ is the phase aberration referred to a parabolic lens with a focal length of f:

$$\Delta\varphi(r) = \mathrm{OPD}(r) - \mathrm{OPD}(0) - \frac{r^2}{2f} \tag{2.45}$$

To use the SR for the laser mode, the aperture that is given by the cylindrical laser crystal with radius r_0 has to be considered and the SR has also to be weighted by the Gaussian intensity distribution of the laser beam [48]. The SR for the laser mode is

$$SR = \frac{|\int_0^{r_0} exp(i2\pi\Delta\varphi/\lambda_l) exp(-\frac{r^2}{\omega_0^2}) r dr|^2}{|\int_0^{\infty} exp(-\frac{r^2}{\omega_0^2}) r dr|^2}. \tag{2.46}$$

A more precise focal length f_{SR} for a certain OPD(r) can be found where the SR(f) has its maximum. In figure 2.6 the numerically calculated OPD from figure 2.5 is used to calculate the SR over a span of possible focal lengths f. The SR reaches its maximum at 1.85 times the parabolic focal length. This value is the SR-corrected focal length, and its OPD is plotted in figure 2.5.

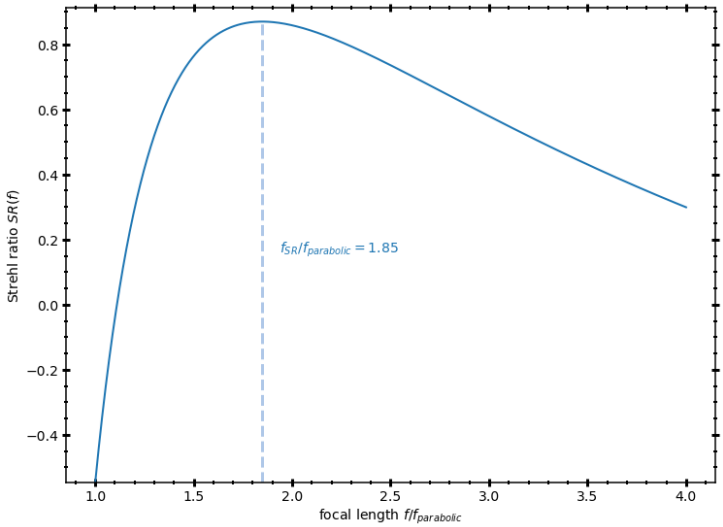

Figure 2.6: *Strehl ratio SR(f) for the numeric OPD from figure 2.5 plotted over focal lengths f normalized to the focal length of the parabolic terms $f_{parabolic}$. The SR has its maximum at f_{SR}.*

Fan *et al.*[49] derived a simple approximation for the SR-corrected thermal lens by introducing the correction factor $r = \frac{f_{SR}}{f_I}$. The SR-corrected thermal lens is given as

$$f_{SR,Fan} = \frac{\omega_{p,avg}^2}{4A_0} \times \left[1 + 2\left(\frac{\omega_l}{\omega_{p,avg}}\right)^2\right]. \tag{2.47}$$

From Fan's approximation it can be seen that in typical laser setups, where the pump beam has the same width as the laser beam, the corrected focal length is three times as long as in the case of the parabolic approximation. But the analytical solution from Fan is only an approximation valid only within a strict parameter

regime. In this work the SR-correction has been done by solving equation 2.46 numerically.

2.3.2 Averaged Pump Beam Waist

The pump beam radius $\omega_p(z)$ varies along the optical axes z. For the calculation of the thermal lens an averaged pump radius was used. To derive an expression for the average pump radius $\omega_{p,avg}$ we first have to divide the crystal into thin slices dz and then integrate the single lenses $df(z)$ to the total focal length along the crystal with length l according to

$$\frac{1}{f} = \int_0^l d\frac{1}{f(z)}. \tag{2.48}$$

The single lens slices $d\frac{1}{f}$ are defined by the pump waist $\omega_p(z)$ and the pump absorption according to equation 2.35. Hence, the integral can be written as

$$\frac{1}{f} = \int_0^l d\frac{1}{f(z)} = \int_0^l \frac{4A_0}{\omega_p(z)} \frac{\alpha e^{-\alpha z}}{1-e^{-\alpha l}} dz. \tag{2.49}$$

We again use equation 2.43 to get for the averaged pump beam waist

$$\frac{1}{\omega_{p,avg}^2} = \int_0^l \frac{\alpha e^{-\alpha z}}{\omega_p(z)(1-e^{-\alpha l})} dz. \tag{2.50}$$

This integral can be solved numerically for any pump beam $\omega_p(z)$ given by equation 2.36 and for any material with absorption α and length l.

The parabolic approximation of the thermal lens (2.43) is a fast way to approximate the thermal lens. In cases where the laser mode radius is similar or even bigger then the pump mode, the correction either by solving the SR integral (2.6) or by using Fan's approximation (2.47) should be used to get a more precise value. The correction for the averaged pump beam radius (2.50) becomes interesting when the length of the gain medium reaches two times the Rayleigh length of the pump beam.

2.4 Q-switched Laser

The principle of Q-switched lasers was investigated early on by Hellwarth and McLung [50, 51, 52] in the sixties. The basic idea is that the onset of lasing at lasing threshold is suppressed by introducing an extra loss inside the cavity. With the extra loss the population inversion density n_g within the gain medium can now be raised far above the lasing threshold n_t. After a certain time of continued pumping, when for example a defined initial population density n_i is reached, the extra loss inside the cavity is rapidly removed. The laser has now an initial population inversion density n_i that is far higher than its lasing threshold, $n_i >> n_t$. Due to the resulting high gain inside the cavity the photon density ϕ reaches high levels quickly. A giant laser pulse is formed.

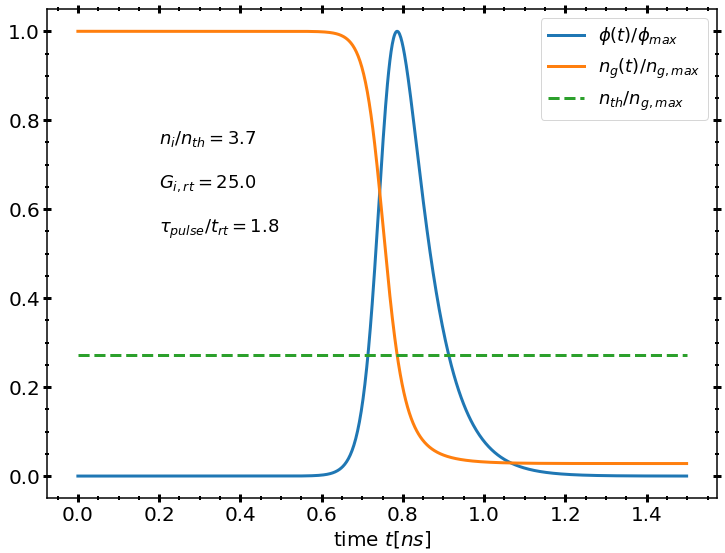

Figure 2.7: *Schematic example for the dynamics of rapidly Q-switched microchip laser. The initial population inversion density n_i is set to a value of 3.7 times the lasing threshold n_{th}. Population inversion density $n_g(t)$ is normalized to its initial value and the photon density ϕ is normalized to its peak value.*

Figure 2.7 shows the formation of a giant laser pulse. Plotted are the inversion density n_i inside the gain medium, set to an initial value of 3.7 times the lasing threshold n_{th}. Shown is also the photon density ϕ inside the cavity. At $t = 0$ a virtual extra loss inside the cavity is removed rapidly and the laser pulse represented by the photon density ϕ inside the cavity starts to build up. The initial population inversion density in this example is by a factor of 3.7 above the lasing threshold which results in a very high gain of 25 per photon round-trip. The photon density raises until it peaks at the point where the excess population inversion is exhausted

and the population inversion density is back to threshold level. From there on the photon density drops rapidly until all photons are coupled out of the laser cavity through the output coupling mirror.

2.4.1 Rapid Q-switching

The rate-equations for rapidly Q-switched lasers where first derived by Wagner and Lengyel [53]. Assuming the gain medium with length l_g within the laser resonator of optical length l_{opt} is uniformly pumped and the photon density is axially uniform, both the population inversion density and the photon density can be treated as spatially averaged values with $n_g = n_g(t)$ and $\phi = \phi(t)$. The laser starts to lase as soon as the extra-loss from the Q-switch is rapidly removed from the cavity. The gain and losses per round-trip time $t_{rt} = 2l_{opt}/c$ are determined by two passes through the gain medium with emission cross section σ_g, one reflection at the output coupling mirror with reflectivity R_{oc} and the dissipative optical loss per round-trip L_{rt}. The total gain can be written as a change in photon density over time with

$$\frac{d\phi}{dt} = \frac{\phi}{t_{rt}}(2\sigma_g n_g l_g - ln(1/R_{oc}) - L_{rt}) \tag{2.51}$$

As the photon density raises, the population inversion diminishes with

$$\frac{dn_g}{dt} = -\gamma\sigma_g c\phi n_g \tag{2.52}$$

where γ is the population reduction factor and c is the speed of light. In this work only four-level laser gain media are treated, so the population reduction factor can be set to one. The power output after the output coupler can be obtained from the intra-cavity photon density by

$$P(t) = \frac{1}{2}h\nu_e cAl_{opt}\ln(1/R_{oc})\phi(t), \tag{2.53}$$

where $h\nu_e$ is the photon energy and A is the area of the transversal laser mode. To derive the total pulse energy, the output power has to be integrated over time from the onset of lasing at time point zero to the end of the laser pulse at infinity. With the help of equation 2.52, the time integral can be written as a integral along the inversion density ranging from the initial population inversion density n_i at lasing onset to the final population inversion density n_f.

$$E_p = \int_0^\infty P(t)dt = \frac{h\nu_e A}{2\sigma_g}\ln\left(\frac{1}{R_{oc}}\right)\int_{n_f}^{n_i}\frac{dn_g}{n_g} = \frac{h\nu_e A}{2\sigma_g}\ln\left(\frac{1}{R_{oc}}\right)\ln\left(\frac{n_i}{n_f}\right) \tag{2.54}$$

The threshold inversion density can be obtained easily when it is viewed as the point in time when the total gain is zero with $\frac{d\phi}{dt} = 0$.

$$n_t = \frac{1}{2\sigma_g l_g}\left[\ln\left(\frac{1}{R_{oc}}\right) + L_{rt}\right] \tag{2.55}$$

By taking the quotient of the rate equations 2.51 and 2.52 the new differential equation can be integrated along the inversion density to yield the solution

$$\phi(t) = \frac{l_g}{l_{opt}}\left[n_i - n_g(t) - n_t \ln\left[\frac{n_i}{n_g(t)}\right]\right]. \tag{2.56}$$

The final inversion density is reached when the pulse is complete and the photon density is back to zero. Setting $\phi(t) = 0$ results in a numerically solvable relation between initial inversion density, threshold inversion density, final inversion density.

$$n_i - n_f = n_t \ln\left(\frac{n_i}{n_f}\right) \tag{2.57}$$

The peak photon density ϕ_{max} and thus the peak output power P_{max} are reached when the excess inversion density is exhausted and the inversion density is back to the value of the threshold inversion density. Setting $n(t) = n_t$ in equation 2.56 an using equation 2.53 we obtain for the peak power

$$P_{max} = \frac{A l_g h\nu c}{2 l_{opt}} \ln\left(\frac{1}{R_{oc}}\right)\left[n_i - n_t\left[1 + \ln\left(\frac{n_i}{n_t}\right)\right]\right]. \tag{2.58}$$

Assuming the generated pulse has a Gaussian form, a pulse shape factor of 0.86 [54] can be applied to estimate the Full Width at Half Maximum (FWHM) with

$$\tau_p \approx 0.86\frac{E_p}{P_{max}} = \frac{1.72 l_{opt}}{c\left[\ln\left(\frac{1}{R_{oc}}\right) + L\right]} \cdot \frac{n_i - n_f}{n_i - n_t\left[1 + \ln\left(\frac{n_i}{n_t}\right)\right]} \tag{2.59}$$

The obtained equations represent a very simple set of tools to estimate output pulse energy and duration for a rapidly q-switched laser. They can be used to optimize a laser design regarding wanted pulse parameters. When for example a short laser pulse is wanted, the easiest way to get there is to shorten the cavity length l_{opt}. This can be seen in equation 2.59, where the pulse duration τ_p scales linearly with the optical cavity length l_{opt}. This effect is easily understood if the Q-switched laser is seen as a energy storage device. Energy is stored within the gain medium in the form of population inversion and it is transferred into photons when a laser pulse is formed. The laser pulse is described by the photon density inside the cavity. The higher the photon density, the more and the faster energy is transferred from the population inversion into the photon field. A lengthening of

the laser cavity increases the laser mode volume thus lowers the photon density. Ultimately it takes longer for the energy inside the gain medium to get transferred into the laser pulse. From that view it makes sense that if short pulse durations are needed, the laser cavity should be as short as feasible.

2.4.2 Q-switching by a Saturable Absorber

There are several ways to introduce loss inside a cavity. One is to use a saturable absorber like Tetravalent Chromium doped Yttrium Aluminium Garnet (Cr^{4+}:YAG). The saturable absorber Cr^{4+}:YAG is best described by a four level system with two absorption cross sections, σ_{abs} for the absorption from the ground state and σ_{esa} for the excited state absorption (see figure 2.8). The absorptivity of the saturable absorber is given by the unsaturated initial transmission $T_0 = e^{-\sigma_{abs} n_{abs,0} l_{abs}}$, where $n_{abs,0}$ is the population density in the ground state and l_{abs} is the length of the absorber.

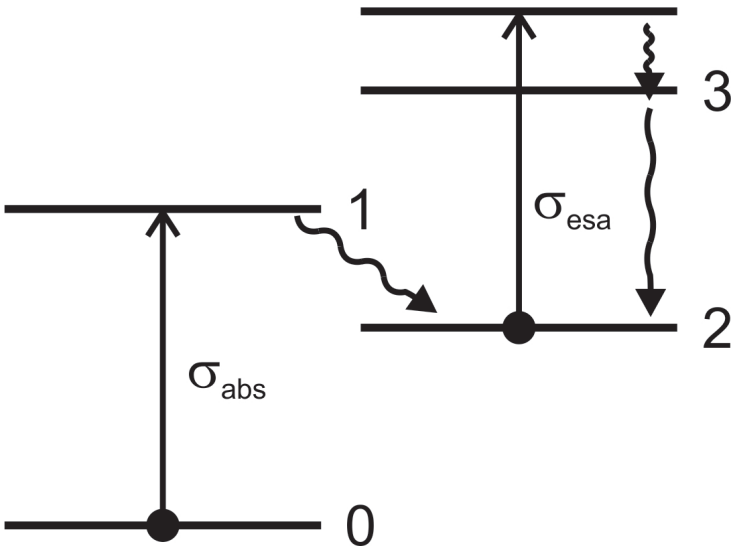

Figure 2.8: *Schematic drawing of the energy levels of Cr^{4+}:YAG. Absorption from ground state 0 with absorption cross section σ_{abs}. Phonon relaxation from level 1 to level 2. Excited state absorption from level 2 to level 3, with excited state absorption cross section σ_{esa}. Phonon relaxation back to level 2.*

When the population inversion density inside the cavity has reached the raised threshold level, the cavity starts to lase and the absorber starts to bleach out becoming more transparent. The bleaching effect is due to the excited state absorption cross section being lower than the cross section of the ground state and also the excited state lifetime being longer the laser pulse. The transmission of the

absorber can raise up to the point where it is completely bleached with the corresponding transmission of $T_{\text{bleached}} = e^{-\sigma_{esa} n_{abs,1} l_{abs}}$, where $n_{abs,1}$ is the population density of the excited state. With this in mind we can formulate a new set of rate equations for Q-switched lasers with saturable absorbers.

$$\begin{aligned}
\frac{d\phi}{dt} &= \frac{\phi}{t_{rt}}(2\sigma_g n_g l_g - 2\sigma_{abs} n_{abs,0} l_{abs} - 2\sigma_{esa} n_{abs,1} l_{abs} && (2.60)\\
&\quad -ln(1/R_{oc}) - L) && (2.61)\\
\frac{dn_g}{dt} &= -\sigma_g c \phi n_g && (2.62)\\
\frac{dn_{abs,0}}{dt} &= -\sigma_{abs} c \phi n_{abs,0} && (2.63)\\
n_{abs,0}(0) &= n_{abs,0}(t) + n_{abs,1}(t) && (2.64)
\end{aligned}$$

The initial population inversion density within the gain medium $n_i = n_g(0)$ is defined as the raised lasing threshold, or in other words it is given as the population inversion density where the photon density change over time switches to positive values with $d\phi/dt = 0$.

$$n_i = \frac{2\sigma_{abs} n_{abs,0} l_{abs} + ln(1/R_{oc}) + L}{2\sigma_g l_g} \tag{2.65}$$

Compared to the rate equations for the rapidly q-switched laser 2.52, the rate equations for q-switched laser with saturable absorber 2.60 include several new terms. The differential equation for the photon density was extended by ground state and excited state absorption of the Saturable Absorber (SA). The equation for the population inversion density within the gain medium stays the same. Two new equation for the population density of the saturable absorbers ground state and excited state are added.

The new terms have several effects on the pulse formation. For one the q-switching is now slower than in the rapid case. The gain within the cavity raises slowly while the saturable absorber bleaches out. The generated pulses are thus longer than in the rapidly q-switched case. Also, during the time the saturable absorber is bleaching out, photons are absorbed by the saturable absorbers ground state, and when the saturable absorber is bleached, photons are still absorbed due to the excited state absorption. Hence, the pulse energy will be lower than in the rapidly q-switched case.

To visualize this effects, an example cavity setup was taken (see design MC01 in table 3.2) and the rate equations have been solved for this cavity for both rapid q-switching and for the q-switching with saturable absorber. The solution is shown in figure 2.9. Plotted are the photon densities ϕ, the population inversion

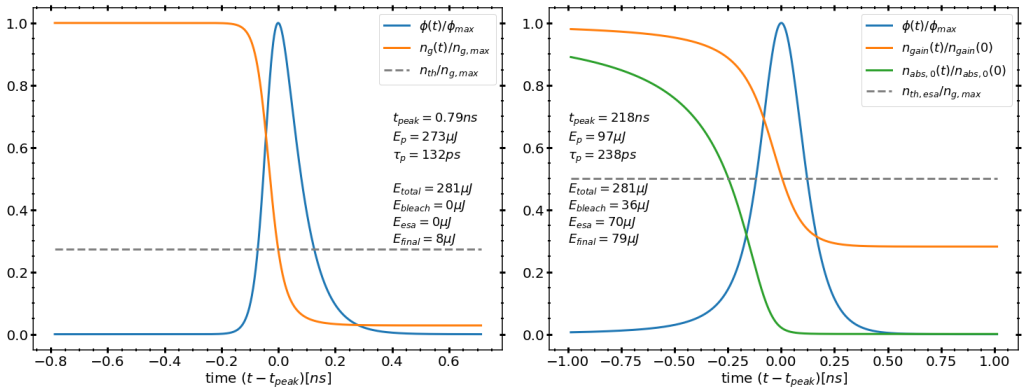

(a) *Rapid Q-switching* **(b)** *Q-switching with saturable absorber*

Figure 2.9: *Schematic drawing of the dynamics within the laser cavity for (a) rapid q-switching and (b) q-switching with a saturable absorber. Plotted are the photon densities ϕ, the population inversion density of the gain medium n_g and the lower level population of the saturable absorber $n_{abs,0}$. The cavity design parameters from table 3.2 have been used. The laser mode radius was set to 78 µm.*

density of the gain medium n_g, the lower level population of the saturable absorber $n_{abs,0}$. The initial population inversion density $n_g(0)$ for the rapid q-switched case was set to be equal to the case where a saturable absorber with initial transmission of T_0 =20% was used. The output coupler is set to a very low value of R_{oc} =30% which is close to the optimal value of 27% given by the optimization method of Degnan [55].

The extracted values from the solutions of the rate equations are the pulse buildup time t_{peak}, the pulse energy E_p and the pulse duration τ_p. Besides the laser pulse being far longer in the case of Q-switching with saturable absorber, the pulse buildup-time is also considerably longer. This is because the first photons emitted by the gain medium are immediately absorbed by the saturable absorber, and it takes a few hundred nanoseconds for the absorber to bleach out to a point where the net-gain is high enough to generate a laser pulse that effectively extracts the stored energy. At the point where the absorber is bleached out (timepoint $t - t_{pulse} \approx -0.15$ ns), the round trip gain left within the cavity has a value of $G_{rt} \approx 2.0$. In the case of rapidly q-switching, the very high initial round trip gain of $G_{rt} = \frac{1}{T_0^2 R_{oc}} \approx 25$ leads to a considerably shorter pulse duration and pulse buildup time.

Another value which is extracted from the numerically solved rate equations is the energy stored in the gain medium E_{total}. It is given in comparison to the channels to which the energy can be transferred to. In the rapid q-switched case, no energy is lost within the saturable absorber, so neither in bleaching it (E_{bleach})

nor in the excited state absorption (E_{esa}). Adding a saturable absorber raises the lasing threshold n_{th} due to the extra term $-2\sigma_{esa}n_{abs,1}l_{abs}$ in the rate equation. The raised threshold is directly responsible for less energy being extracted from the gain medium, and the remaining energy within the gain medium (E_{final}) after the laser pulse is considerably higher when a saturable absorber is used. All in all the saturable absorber is a way to implement q-switching, but it adds a lot of losses and results in lower extraction efficiency then in the ideal rapid q-switched case.

	Example Microchip Laser
gain material	1.1 at.% Neodymium doped YAG, 2.5 mm long
saturable absorber	Cr^{4+} doped YAG, 2.5 mm long
	initial transmission $T_0 = 20\%$
end-caps	un-doped YAG, 0.5 mm long
	convex curvature with radius $R = 400$ mm
diameter	bonded chip cut-out diameter $d = 3$ mm
coatings	input: HR @1064 nm, AR @808 nm
	output: PR30% @1064 nm

Table 2.1: *Design parameter for Q-switched Microchip laser used as an example setup. The design consists of a gain medium bonded on a saturable absorber, then again two un-doped end-caps are bonded on the side-faces. Input coupling mirror for the pump is on the gain mediums side and the output coupler is on the saturable absorbers side. Both are coated directly on the end-caps.*

2.4.3 Thermal Lensing in Q-switched Lasers

So far a laser mode diameter was assumed for the solutions of the rate equations. In chapter 2.2.2, it was shown that the laser mode size depends on the optical elements within the cavity, one of which is the thermal lens forming in the gain medium due to pump absorption (see section 2.3).

In general, it makes sense to match the size of the pumping mode to the size of the laser mode. If the pumping mode is bigger, the deposited energy is only partially accessible as the laser mode does not spatially overlap with the whole pumped region. If the pump mode is smaller than the laser mode, a higher local inversion density has to be reached to get to the needed spatially averaged initial inversion density. The higher the local inversion density, the more losses appear due to two-ion processes like up-conversion or cross-relaxation. The total deposited heat per pump period can be easily estimated with the needed initial population inversion plus the pump parameter that are given in chapter 2.3. In

practice, one starts by assuming a pump mode size, and then iterates between calculating the laser mode size and re-setting the pump mode size to that new value, until it converges to a constant value.

As already mentioned, the laser mode size depends on the total amount of heat deposited in the crystal. With a fixed laser design, raising the PRF deposits more heat in the gain medium, therefore creating a stronger thermal lens, which cases a smaller laser mode size and ultimately in a reduced pulse energy. Figure 2.10 shows the pulse energy for our example microchip laser setup as a function of PRF. In chapter 2.3, it is shown that there are different ways to calculate the thermal lens. The method from Innocenzi [45] is the easiest to apply and it gives a good first estimate for the laser mode width and thus the pulse energy E_p. The pulse energy is also plotted for the case where the Strehl-Ratio correction is applied ($E_{p,SR}$). The SR-correction averages the focal length of the laser mode over the whole laser mode size, and it results in a reduction of the thermal lens. Hence, the laser mode becomes bigger and so does the pulse energy. The second correction plotted as $E_{p,SR,SA}$ includes the calculation of a second thermal lens within the saturable absorber (which is then also SR-corrected). Due to the saturable absorber absorbing a considerate amount of the emitted photons, a temperature gradient similar to the one in the gain medium forms. The combination of SR-correction and second thermal lens results in a laser mode size and pulse energy that is smaller than in the approximation by Innocenzi.

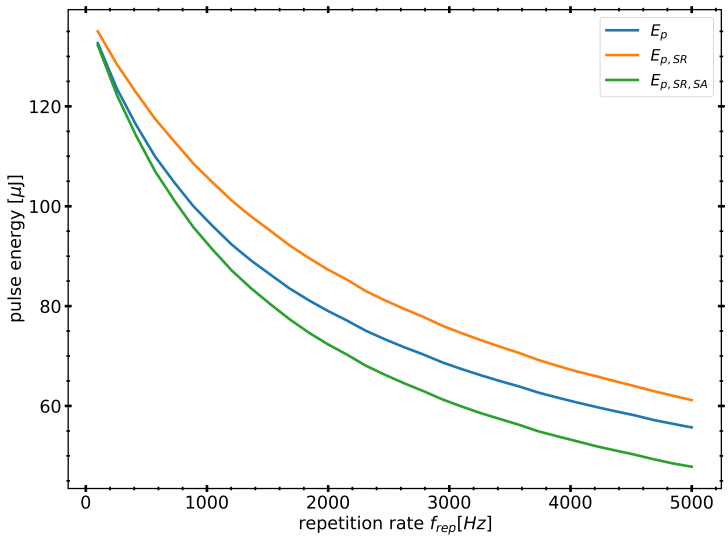

Figure 2.10: *Pulse energies over repetition rate (PRF) in case of the example microchip setup. Pulse energies according to Innocenzi (E_p), with SR-correction ($E_{p,SR}$), including second thermal lens inside the saturable absorber ($E_{p,SR,SA}$) are given.*

Chapter 3

Q-Switched Microchip Laser

Diode pumped passively Q-switched microchip lasers represent a very simple and intrinsically robust and reliable type of monolithic laser resonator. When a gain crystal is bonded onto a saturable absorber and the cavity mirrors are coated directly onto the end-faces, the resulting microchip laser can have cavity lengths from a few mm down to 200 µm or even less. With their short cavities, passively Q-switched microchip lasers are able to produce pulse lengths in the sub-ns range down to a few-10 ps. Their pulse energies range from 100 nJ at MHz PRF up to several hundred µJ at 100 Hz PRF. As their cavities do not contain any movable parts but consist solely of a single bonded crystal, they are intrinsically insensitive to vibrations and misalignment. A schematic drawing of such a microchip lasers is shown in figure 3.1, where a Neodymium doped Yttrium Aluminium Garnet (Nd:YAG) crystal is used as the gain medium and a Cr^{4+}:YAG crystal acts as the saturable absorber.

An alternative to the passive q-switching with a saturable absorber would be active q-switching with either an electro-optic or an acousto-optic modulator. The active methods have several advantages over the passive one. The time point for lasing onset is electronically trigger-able, which reduces the timing-jitter. The pulse energy is variable during operation as the initial transmission is not fixed by the saturable absorber. Another advantage is a considerable lower loss within the cavity after its Q-value is switched to high as no excited state absorptions are present. On the other hand have these active modulators a certain length of at least 10 mm, which will result in a total cavity length that does not allow few-100ps pulses. Hence, an active Q-switching cavity was not pursued within this work.

In this chapter an overview of published passively Q-switched microchip laser designs is given (section 3.1). Based on these publications a microchip design is proposed that can be used as an oscillator for the NextGenPIRL (section 3.2). The chapter includes a discussion about how to optimize that design towards the DIVE application and also some restrictions of the design due to the Laser Induced Damage Threshold (LIDT).

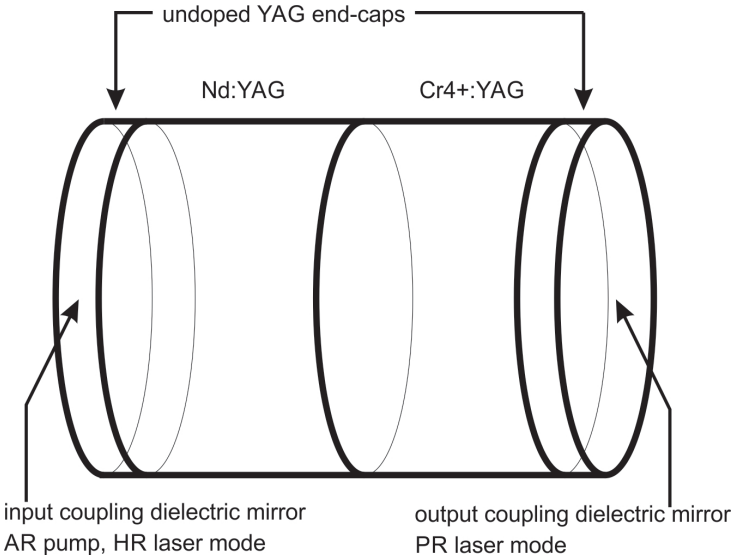

Figure 3.1: *Schematic drawing of a monolithic Q-switched microchip laser. The gain medium (Nd:YAG) is bonded directly on the Q-switch (Cr^{4+}:YAG). Two undoped end-caps are bonded onto the outer surfaces and the cavity mirrors are coated directly on the end-caps.*

3.1 Published Microchip Lasers

The shortest pulse lengths of passively Q-switched microchip lasers can be achieved when a high gain material like Nd:YVO_4 (Neodymium doped Yttrium Vanadate) is bonded on a Semiconductor Saturable Absorber Mirror (SESAM). The SESAM has a fair modulation depth of typically 10 to 20 percent and it does not contribute to the length of the cavity. Braun *et al.*[56] used for the gain material a very short and highly doped Nd:YVO_4 crystal. The high absorption cross section of Nd:YVO_4 together with the high doping of 3 at.% resulted in an absorption length for the pump beam of only 100 µm and thus a crystal length of only 200 µm was enough to get a good pump absorption. The achieved pulse lengths varied between 56 ps and 68 ps with pulse energies of 62 nJ at 85 kHz PRF and 370 nJ at 160 kHz PRF respectively. Even shorter pulses can be achieved when the cavity length is further reduced. In the design of Spüler *et al.*[57] a microchip laser with a 185 µm short crystal generated 37 ps pulses. The shortest pulses so far have been reported by Butler *et al.*[58], where a 110 µm short cavity led to a pulse duration of only 22 ps. Although the pulses from these SESAM based microchip lasers are very short, their pulse energy is very low. As is shown before in the theory chapter, the pulse energy in Q-switched lasers depends on the amount of stored energy before the lasing threshold is reached. With the high emission cross section

of Nd:YVO_4 and the limited modulation depth of SESAMss only sub-µJ energy levels are achievable with this kind of lasers. To breach this limitation, different gain materials with lower emission cross sections have been tried. Spüler *et al.*[59] used a highly doped Ytterbium doped Yttrium Aluminium Garnet (Yb:YAG) crystal. But even with the low emission cross section of $2.5 \times 10^{-20}\text{cm}^2$ the highest pulse energy achieved was still only 1.1 µJ.

To get to higher pulse energies, a different saturable absorber material with a higher modulation depth has to be used. Tetravalent chromium doped crystals like Cr^{4+}:YAG are strongly absorbing in the near infrared and their initial transmission can be scaled far beyond of what is possible with a SESAM. Zhou *et al.*[60] and Wang *et al.*[61] reported about monolithic self-q-switched co-doped Cr^{4+},Nd:YAG lasers. In their design the gain crystal Nd:YAG is co-doped with tetravalent chromium ions. The single monolithic crystal acted both as gain medium and as saturable absorber. The resulting cavities were short enough to generate pulses with durations down to 290 ps at a pulse energy of 8 µJ. But as the tetravalent chromium ions are also highly absorbent at the pump wavelength, this design proved to be not viable for high PRFs. The absorption of the pump light by the saturable absorber led to a high thermal load and the lasers could not be operated at PRFs above 100 Hz.

Zayhowski and Dill [62] reported on a passively Q-switched microchip laser with separately grown Nd:YAG and Cr^{4+}:YAG crystals. They cut and polished the two crystals, bonded them together and coated the end-mirrors directly on the end-faces. The resulting passively Q-switched microchip lasers produced pulses with a duration of 337 ps and a pulse energy of 11 µJ at up to 6 kHz PRF. Besides delivering a fair pulse energy at several kHz PRF, the laser was reported to run in a single longitudinal and in a single transversal mode. It was reported to be very stable with a pulse-to-pulse amplitude jitter of less the 0.5%. A few years later Zayhowski reported on a series of Q-switched microchip lasers with varying design parameters [63]. The initial transmission of the saturable absorber, the reflectivity of the output coupling mirror and the cavity length were varied to optimize the microchip lasers towards either high pulse energy or short pulse duration 3.1. The generated pulses are reported to be as short as 218 ps, the pulse energies were up to 250 µJ and average powers of up to 605 mW were reached.

	microchip design				laser pulse			
year, reference	L_{opt} [mm]	T_0 [%]	R_{oc} [%]	w_p [µm]	τ [ps]	E_p [µJ]	f_{rep} [kHz]	P_{avg} [mW]
1994, [62]	1.36	87	94	50	337	11	6.0	66
1998, [63]	1.36	86	80	50	218	4.0	5.0	20
1998, [63]	11.8	40	40	63	390	110	5.5	605
1998, [63]	21.8	40	40	63	700	225	2.0	450
1998, [63] (*)	11.3	26	26	63	310	200	1.0	200
1998, [63]	18.6	26	26	63	380	250	1.0	250

Table 3.1: *Outline of published Q-switched Microchip lasers with pulse durations below 1 ns. The design HPMCL-3 is marked with a (*)*

3.2 Design Considerations

Zayhowski's reports show that passively Q-switched microchip lasers are a promising source for the generation of few 100 ps pulses at a few-kHz PRF with pulse energies in the 10 to 100 µJ range. The achieved pulse duration are below of what is needed for the DIVE process and the pulse energies are high enough to be amplified by a simple multipass-amplifier without the need for sophisticated regenerative amplifiers. The design from Zayhowski named HPMCL-3 [63] is chosen as a starting point for the proposed microchip laser. That design can be optimized by shortening the pulse duration further down closer to what was used in the first DIVE studies performed by Franjic *et al.*[16] and higher pulse energy might also be possible.

3.2.1 Shortening the Pulse Duration

The pulse duration of a passively Q-switched microchip laser strongly depends on the length of the cavity. In the model for rapidly Q-switched lasers, the pulse duration τ_p scales linearly with the optical cavity length l_{opt}. This effect is easily understood if the microchip laser is seen as an energy storage device. The energy is stored in the form of population inversion and it is transformed into photons when a pulse is formed. The higher the photon density inside the cavity, the faster the energy is transferred from the population inversion into the photon field. A lengthening of the laser cavity lowers the photon density as the emitted photons are distributed over a larger volume. Ultimately it takes longer for the energy inside the gain medium to get transferred into the laser pulse. From that view, it makes sense that in order to get short pulse durations the cavity should be as

short as feasible. Another way to shorten the laser pulses is to decrease the initial transmission from the saturable absorber. Again from the view point of stored energy, the lower the initial transmission, the higher the population inversion density when the pulse forms. High inversion density means higher gain and thus faster energy extraction.

Decreasing the initial transmission of the saturable absorber does not just shorten the pulse duration. As more energy is stored in the gain medium before the lasing threshold is reached, more energy is available to be extracted from a single laser pulse. Counteracting to the increase in stored energy is the increased thermal lensing. With increased energy to be stored in the gain medium, a stronger pumping is necessary which leads to a stronger thermal lensing and ultimately to a smaller transversal laser mode size.

Figure 3.2 shows simulated pulse durations and pulse energies for varying initial transmissions of the saturable absorber. For the calculation the example microchip laser design (MC01) was used together with the rate equations from chapter 2.4.2 and a fixed transversal mode radius. It can be seen that the pulse duration shortens with lowered initial transmission, and that the pulse energy increases as more energy is stored in the gain medium before the initial population inversion is reached.

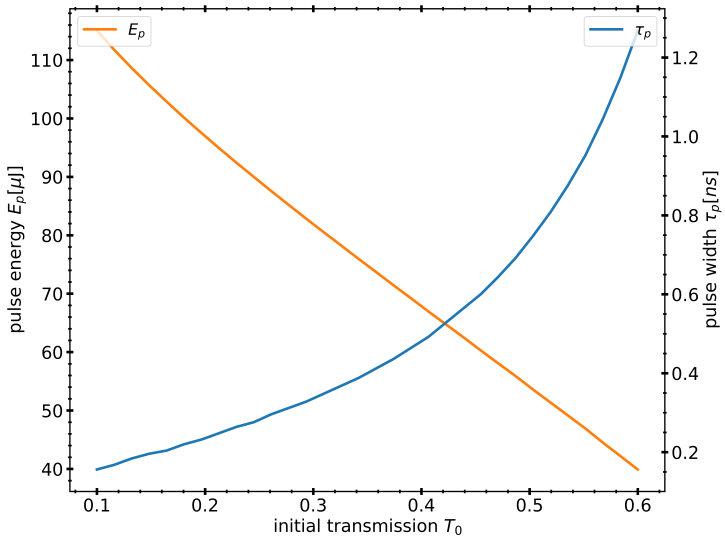

Figure 3.2: *Simulated pulse durations τ_p and pulse energies E_p plotted along varying initial transmission T_0. The microchip geometry from table 2.1 was used, the reflectivity of the output coupler is set to 30% and no calculation of the thermal lensing was done but the laser mode radius was set at 78 µm.*

3.2.2 Laser Induced Damage Threshold

With shortening of the cavity and increasing the pulse energy, the peak fluence after the output coupling mirror $F_{peak,oc}$ will also increase. The LIDT has to be checked in that case. It was shown by Stuart *et al.*[64] that the fluence at damage threshold scales with $\sqrt{\tau}$.

$$F_{peak,oc} = \frac{2E_p}{\pi w_0^2} \qquad and \tag{3.1}$$

$$F_{LIDT} = F_{LIDT,10ns}\sqrt{\tau/10ns} \tag{3.2}$$

The simulated output fluence can be plotted together with the scaled damage threshold over varying initial transmissions of the absorber. Starting from a typical value for the damage threshold of dielectric coatings of $7.5\,\mathrm{J/cm^2}$ at a pulse length of 10 ns, figure 3.3 shows that the peak fluence of the generated laser pulses reaches the damage threshold at an initial transmission of approximately $T_0 \approx 16\%$. This can be seen as a lower limit to the initial transmission for which the laser pulses start to damage the microchip lasers output coupling mirror.

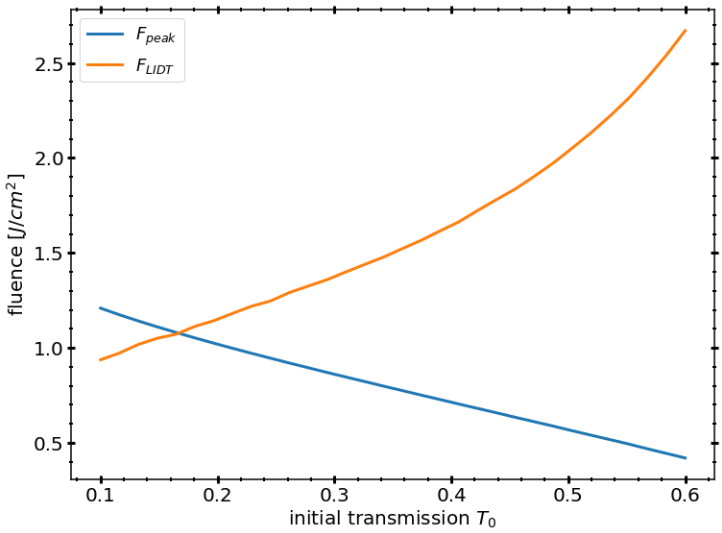

Figure 3.3: *Peak fluence at output coupling mirror F_{peak} of simulated example microchip laser. Laser induced damage threshold F_{LIDT} according to the simulated pulse length and scaled by the $\sqrt{\tau}$-law.*

3.3 Discussion

From the published microchip lasers so far, the HPMCL-3 design from Zayhowski stands out. Its pulse duration is very close to what is needed for the DIVE effect and the pulse energy of that design is high enough to be amplified to the needed mJ-level by a simple multipass amplifier module. The design is the basis for the proposed microchip that should act as a seed for the NextGenPIRL. By shortening the optical length and by decreasing the initial transmission of the saturable absorber the pulse duration should be further decreased. For that purpose the end-caps of the proposed seed are chosen to be shorter. Zayhowski used 1 mm long ones on both end-faces, to suppress end-bulging and to increase the damage threshold. Shortening the length by a factor of two should still leave enough thickness to suppress bulging and increase damage threshold. The initial transmission of the absorber with $T_0 = 26\%$ is lowered to 20%, which is still above the lower limit of 16% for damage free operation. The length of the gain medium was also reduced from 3 mm down to 2.5 mm. The resulting proposed microchip laser design (MC01) for the NextGenPIRL is shown in table 3.2.

	end-cap l[mm]	gain l[mm]	SA l[mm]	end-cap l[mm]	optical length l[mm]	initial trans. T_0[%]	output coupler R_{oc}[%]
HPMCL-3	1.0	3.0	2.25	1.0	13.2	26	26
MC01	0.5	2.5	2.5	0.5	10.9	20	30

Table 3.2: *Design parameter for Q-switched Microchip laser used as the proposed design (MC01) in comparison with the design by Zayhowski (HPMCL-3). Both designs consist of a gain medium (Nd:YAG) bonded on a saturable absorber (Cr^{4+}:YAG) and with two un-doped end-caps bonded on the side-faces.*

Chapter 4

Simulating the Microchip Laser

A model for calculating the laser pulse parameters for a given Q-switched microchip laser design has been given in chapter 2, where a set of rate equations (equations 2.60) have to be solved. The thermal lens which determines the laser mode size in a plane-plane cavity can be calculated according to equation 2.43. The calculation of the thermal lens can be done more precisely when two corrections are added to the model, with the Strehl-Ratio correction (equation 2.46) being one and the adding of a second thermal lens within the saturable absorber being the other. These corrections make a more precise determination of the laser mode size possible. In this section more corrections and extensions to the previously given model are shown in detail. These extensions will be vital to understand the characteristics of the proposed Q-switched microchip lasers (MC01, table 3.2) for the NextGenPIRL.

The first extension of the model includes the lower level lifetime of the gain material (section 4.1). It will be shown that this effect stretches the Q-switched laser pulses and also lowers the pulse energy. Furthermore, a non-zero lifetime of the lower laser level can result in satellite pulse generation. It will be investigated if the proposed microchip laser (MC01) is prone to generate these pulses. The next extension is a temperature dependent emission cross section (section 4.2). This effect also changes the laser pulse parameter. This time the change is dependent on the temperature within the gain region of the laser crystal. A complex model will be introduced that enables to simulate the temperature dependence of the complete emission spectrum of Nd:YAG.

A major extension to the model of Q-switched lasers is introduced in section 4.3. The photon field inside the cavity will be treated with modulations according to the longitudinal mode frequency. It will be shown that in single longitudinal mode operation the pulse energy is severely reduced due to spatial hole burning. The spatially modulated photon field results in further effects, namely the generation of L-mode satellite pulses (sections 4.4), mode-beating within one laser pulse (section 4.5) and mode-hopping between consecutive laser pulses (section 4.6). These effects will be explained in detail and it will be shown how they influence the stability of the proposed microchip laser.

4.1 Lower Level Lifetime

The model derived in the theory chapter treats the gain medium of the Q-switched laser as a four level laser. This treatment is only valid if the lower laser level has a lifetime that is far shorter than the photon lifetime within the cavity (see Degnan *et al.*[65]). In case the lifetime of the lower laser level τ_l becomes comparable to the photon lifetime within the cavity, the afore derived rate equations (2.60) have to be extended with an equation for the population of the lower laser level.

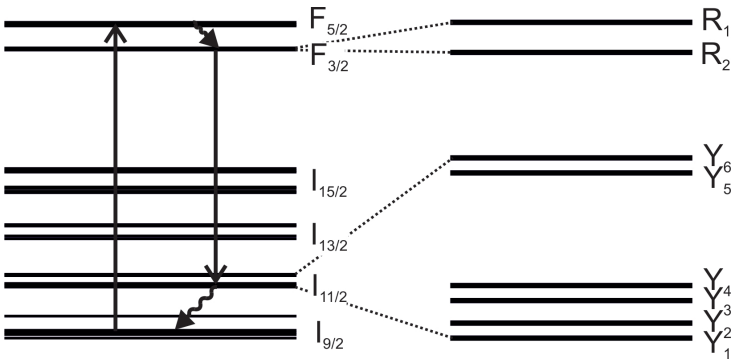

Figure 4.1: *Energy (sub-)levels of Neodymium doped YAG. The laser transition, the pump transition and the phonon transitions are added as arrows. Energy levels are taken from Kaminskii [66].*

The gain medium of the proposed microchip laser is a trivalent Neodymium doped Yttrium-Aluminum-Garnet (Nd^{3+}:YAG or just Nd:YAG), which is a four level gain material with a non-zero lower laser level lifetime τ_l. Figure 4.1 shows the energy levels and the transitions important for the proposed microchip laser. The upper laser level manifold $F_{3/2}$ consists of two sub-levels (R_1, R_2), the lower laser level manifold $I_{11/2}$ consists of six sub-levels ($Y_1, ...Y_6$). The relative population of each sub-level within its manifold is determined by the Boltzmann distribution. Their relative populations f_n are given by

$$f_n(T) = \frac{e^{-\frac{E_n - E_0}{k_B T}}}{\sum_{i=1}^{N} e^{-\frac{E_i - E_0}{k_B T}}} \tag{4.1}$$

with energies E_n of the sub-levels and E_0 representing the lowest sub-level within the manifold (i.e. Y_1 or R_1), Boltzmann constant k_B and temperature T. Degeneracies g_n have been excluded, as they have the same value for each sub-level. Nd:YAG lasers are commonly operated at the wavelength of the highest emission cross section, and so is our proposed microchip design. The point of the

highest emission cross section of Nd:YAG is around 1064 nm, which corresponds to the transition between the R_2 and Y_3 sub-levels. Their relative populations within their manifold are $f_2^{F_{3/2}} = 0.41$ and $f_3^{I_{11/2}} = 0.19$ at room temperature.

According to Einstein and in the case of a two-level system, the probability for emission is the same as for absorption (reciprocity principle). When the emission cross section is defined this way, it is called the spectroscopic emission cross section $\sigma_{em,u\to l}$ for the photon transition between the upper laser level u and the lower laser level l, with the spectroscopic absorption cross section between these two levels being identical $\sigma_{abs,l\to u} = \sigma_{em,u\to l}$. This relation is called the reciprocity of the spectral emission cross sections.

As the upper laser level in Nd:YAG is part of a manifold, the probability for an electron within this manifold being located at the right sub-level has to be taken into account. One way to do this is to define the population density of the upper laser level $n_u(t)$ as a fraction of the total population density in the upper laser manifold $n_{u,i}(t) = f_i n_{u,total}(t)$. The population fraction f_i can also be moved from the population inversion to the emission cross section, resulting in the definition of the effective emission cross section with $\sigma_{eff,u\to l} = f_i \sigma_{em,u\to l}$. In order to be consistent with the conventions used in the rate equations before, the emission cross sections σ_g is defined as the effective emission cross section. The effective absorption cross-section for re-absorption from the lower laser level can thus be determined from the effective emission cross section and the population fractions of the upper and lower laser level by

$$\sigma_{reabs} = \sigma_g \frac{f_3(I_{11/2})}{f_2(F_{3/2})}. \tag{4.2}$$

With the lifetime τ_l of the lower laser level manifold, the new set of rate equations are

$$\begin{aligned}
\frac{d\phi}{dt} &= \frac{\phi}{t_{rt}}(2\sigma_g n_{g,u} l_g - 2\sigma_{reabs} n_{g,l} l_g \\
&\quad -2\sigma_{abs} n_{abs,0} l_{abs} - 2\sigma_{esa} n_{abs,1} l_{abs} - ln(1/R_{oc}) - L) && (4.3)\\
\frac{dn_{g,u}}{dt} &= -\sigma_g c\phi n_{g,u} + \sigma_{reabs} c\phi n_{g,l} && (4.4)\\
\frac{dn_{g,l}}{dt} &= \sigma_g c\phi n_{g,u} - \sigma_{reabs} c\phi n_{g,l} - \frac{n_{g,l}}{\tau_l} && (4.5)\\
\frac{dn_{abs,0}}{dt} &= -\sigma_{abs} c\phi n_{abs,0} && (4.6)\\
n_{abs,0}(0) &= n_{abs,0}(t) + n_{abs,1}(t) && (4.7)
\end{aligned}$$

The lifetime of the lower laser level of the 1064 nm transition of Nd:YAG was measured by Bibeau *et al.*[67] to be 225 ps, which is used within this work. The

new model can be applied to the proposed Microchip design. Figure 4.2 shows the result of two simulations for zero and for non-zero lower level lifetimes. Due to the lowered gain resulting from re-absorption from the lower laser level, less energy gets extracted from the system. The reduction in pulse energy for the proposed microchip laser within the simulation is 22%. This value is in good agreement with the study from Fan [68], who investigated the effect of finite lower level lifetime in Q-switched lasers. The model he derived is very similar to the one presented in this work, but it excludes Excited State Absorption (ESA) from the SA. The model was then used for the two extreme cases, where the lower level lifetime is either zero or infinite. When applied to Nd:YAG lasers, the study showed the worst case reduction of 32% in output energy when the lower level lifetime is set to infinite.

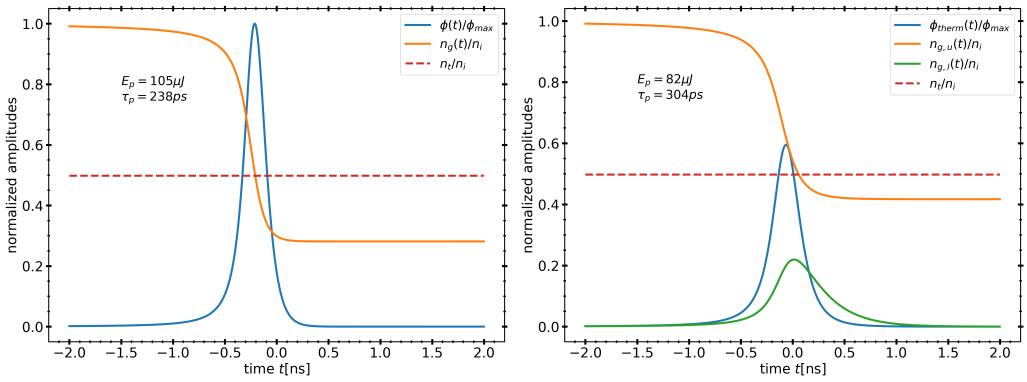

(a) $\tau_l = 0$ **(b)** τ_l =225 *ps*

Figure 4.2: *Solutions of the rate equations for the proposed microchip laser (see table 2.1). Two cases are shown, which are the model with zero lower level lifetime (a) and with non-zero lower level lifetime (b). Plotted are the photon densities* ϕ *and* ϕ_{therm} *normalized to the maximum of* ϕ*, the upper laser level population* n_g *and* $n_{g,u}$*, the lower laser level population* $n_{g,l}$ *and the lasing threshold* n_t *including losses due to ESA in the SA. Given are also resulting pulse energies* E_p *and pulse durations* τ_p*.*

Later, Degnan [65] studied the effects of non-zero lower level lifetime appearing in Q-switched lasers in more detail. His study revealed that when the cavity photon lifetime t_c is small in comparison to the lifetime of the lower laser level, trailing satellite pulses can be generated from the remaining population in the upper laser level. His simulations showed that after the main pulse is generated, the population in the upper laser level can turn into inversion that is above threshold as soon as the lower laser level is depopulated. Depending on the ratio between initial inversion and the lasing threshold at a high Q-factor, trailing satellite pulses can appear for designs where the cavity photon lifetime is smaller than a tenth of the lower level lifetime ($t_c < \frac{1}{10}\tau_l$). The photon lifetime within

the proposed microchip laser is 32.9 ps when losses due to the ESA within the saturable absorber are included. This value is only slightly bigger than a tenth of τ_l. According to Degnan's studies, no satellite pulse should be generated by the proposed microchip laser. As other kind of satellite pulses will be introduced later within this chapter, the satellite pulses due to a non-zero lower level lifetime are called L^3-satellite pulses within this work.

Another hint on if L^3-satellite pulses are generated in the proposed microchip laser can be deduced from the simulation results shown in figure 4.2. The population density of the upper state $n_{g,u}$ drops below the lasing threshold n_t (drawn as a dashed line). Hence, no positive gain is accessible within the cavity. This simulation shows that no L^3-satellite pulses are expected to be generated by the proposed microchip laser.

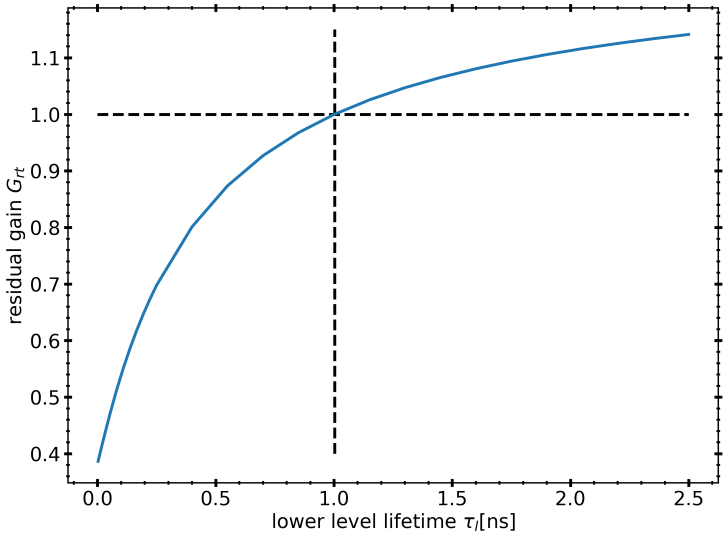

Figure 4.3: *Residual round-trip gain G_{rt} of the proposed microchip laser after the first laser pulse is extracted in dependency on the lower laser level lifetime τ_l. Shown is also the intercept at threshold $G_{rt}(\tau_l) = 1$ with $\tau_l \approx 1ns$.*

To see how far the proposed microchip laser is away from generating L^3-satellite pulses, the simulation was performed in a series with increasing lifetime τ_l. Figure 4.3 shows the residual round-trip gain G_{rt} within the proposed microchip laser after the main pulse is extracted. The residual round-trip gain increases with the lifetime and it reaches the lasing threshold at τ_l =1.0 ns. This value for τ_l is more than four times higher than the actual lifetime for Nd:YAG. According to this simulation, the proposed microchip laser is far away from generating L^3-satellite pulses.

L^3-Satellite pulses can be easily achieved experimentally by switching the gain material from Nd:YAG with its very short lower laser level lifetime of 225 ps to

a gain material with a lower laser level lifetime in the nanosecond range. Ng *et al.*[69] build a Nd:$GdVO_4$ (Neodymium doped Gadolinium Vanadate) based Q-switched laser that was able to generate satellite pulses. The photon lifetime of their cavity was 780 ps, which is more than 25 times lower than the estimated value for the lower level lifetime of Nd:$GdVO_4$ with 20 ns.

4.2 Temperature Dependency

After the first reports on doped crystal based solid-state lasers, studies have revealed that direct one-phonon and two-phonon Raman processes play the dominant role in homogeneous broadening of the spectral lines and their thermal shift. McCumber and Sturge [70] derived a model for the temperature dependent line width and position in ruby, which can also be applied to other solid-state laser crystals. The dominant process determining the line-shapes have been interpreted as direct phonon or two-phonon Raman processes which predict a Lorentzian line-shape with a line-shape factor

$$g_{if}(\nu) = \frac{\Delta\nu_{if}}{2\pi} \frac{1}{(\Delta\nu_{if}/2)^2 + (\nu - \nu_{if})^2} \tag{4.8}$$

for all the transitions from state i to state f, where ν_{if} is the center frequency and $\Delta\nu_{if}$ is the width of the line profile. Later on, Kushida [71] adopted the phonon-electron interaction model for Ruby to Neodymium doped YAG, which can be written as

$$\nu_{if}(T) = \nu_{if}(0) - c_{if}\left(\frac{T}{\Theta_D}\right)^4 \int_0^{\frac{\Theta_D}{T}} \frac{x^3}{e^x - 1} dx \tag{4.9}$$

$$\Delta\nu_{if}(T) = \Delta\nu_{if}(0) + d_{if}\left(\frac{T}{\Theta_D}\right)^7 \int_0^{\frac{\Theta_D}{T}} \frac{x^6 e^x}{(e^x - 1)^2} dx \tag{4.10}$$

The derived model consists of two offsets at zero temperature $\nu_{if}(0)$ and $\Delta\nu_{if}(0)$, two material dependent coupling parameters c_{if} and d_{if} and the crystal specific Debye temperature Θ_D. The Debye temperature can be found in the literature to be $795K$ for YAG [72]. Both the spectral offsets and the material specific coupling parameters have to be determined experimentally by fitting the model to a data set.

The model so far is only for one single transition from i to j. To get the combined temperature dependent emission cross section, all single line-shape factors g_{if} for all possible transitions $i \rightarrow f$ between the upper laser level manifold j and the lower laser level manifold k have to be weighted for their probability and transition rate and then summed. The first weighing factor is a normalized transition probability distribution b_{if}. The factor represents the normalized distribution of the transition probabilities into the sub-levels of the lower manifold k for each upper sub-level i. It can be used to sum up the line-shape functions over the lower manifold according to

$$g_i^k(\nu) = \sum_{f \in k} b_{if} g_{if}(\nu). \tag{4.11}$$

The definition of the weighting factor b_{if} is very close to the one for the branching ratio for transitions from one manifold to all possible lower manifolds. But here we only look at the transition between two manifolds, and b_{if} could be interpreted as an inter-sub-level branching ratio. Starting from a sub-level i, its population probability is given by the fractional population f_i, that was introduced in the previous section. The probability for a transition from a sub-level i to the lower manifold k can be described by the decay rate A_i. The sum over all A_i weighted with the corresponding fractional population is the total decay rate A_{jk} for the $j \to k$ transition.

$$A_{jk} = \sum_{i \in j} f_i A_i = \frac{1}{\tau_{jk}} \tag{4.12}$$

Thus each single transition from an upper sub-level to the lower manifold will have to be weighted by its relative upper sub-level decay rate a_i defined by

$$a_i = \frac{A_i}{\sum_{i \in j} A_i f_i}. \tag{4.13}$$

Now the complete line-shape function for the transition $j \to k$ can be written as the weighted sum over all transitions from i to k by

$$g^{jk}(\nu) = \sum_{i \in j} a_i f_i g_i^k(\nu), \qquad \text{with} \quad \sum_{f \in k} b_{if} = 1. \tag{4.14}$$

With the definition of the emission cross section from equation 2.13 the emission cross section for the $j \to k$ transition becomes

$$\sigma^{jk}(\nu) = \frac{\lambda^2}{16\pi^2 n^2 \tau_{jk}} \sum_{i \in j f \in k} \frac{a_i b_{if} f_i \Delta\nu_{if}}{(\Delta\nu_{if}/2)^2 + (\nu - \nu_{if})^2} \tag{4.15}$$

Sato and Taira [73] made the effort to carefully evaluate a series of fluorescence spectra of the $F_{3/2} \to I_{11/2}$ transition in Nd:YAG to retrieve the temperature dependent coupling parameters c_{if} and d_{if}, the offsets at zero temperature $\nu_{if}(0)$ and $\Delta\nu_{if}(0)$, the relative decay rates a_i and the inter-manifold branching ratio b_{if}. To correlate the parameters to a fluorescence intensity, they used the Füchtbauer Ladenburg equation to deduce the expression

$$I(\nu) \propto \nu^3 \sum_{i,f} \frac{a_i b_{if} f_i \Delta\nu_{if}}{(\Delta\nu_{if}/2)^2 + (\nu - \nu_i f)^2}. \tag{4.16}$$

As the model of Sato and Taira specifically aims for temperature dependent parameters, it includes only changes over temperature but not the actual peak value of the emission cross section. The peak effective emission cross section can be retrieved from Köchner [43] with a value of $2.8 \times 10^{-19} cm^2$ at room temperature.

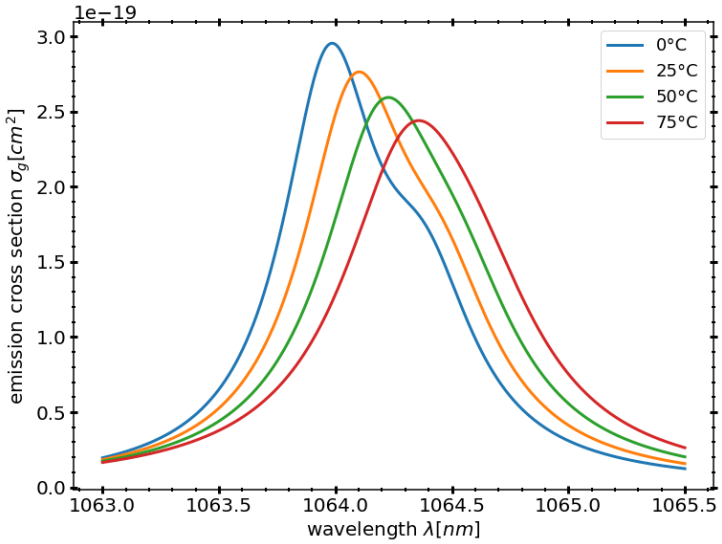

Figure 4.4: *Effective emission cross section of the $F_{3/2} \rightarrow I_{11/2}$ transition in Neodymium doped YAG at different temperatures. Data retrieved from theoretical model from Sato and Taira [73]. Peak emission cross section at $T = 20°C$ retrieved from Köchner [43]. Shown are only the spectral lines of the overlapping $R_2 \rightarrow Y_3$ and $R_1 \rightarrow Y_2$ sub-level transitions.*

Figure 4.4 shows the temperature dependent effective emission cross section spectra of Neodymium doped YAG at different temperatures. Shown are the $R_2 \rightarrow Y_3$ and the partly overlapping $R_1 \rightarrow Y_2$ transitions. The data is the numeric solution from theoretical model from Sato and Taira [73] combined with the peak emission cross section given by Koechner [43]. The peak of the emission cross section spectrum clearly moves to longer wavelengths with increased temperature. With the width of the emission lines increasing with temperature and the lifetime of Nd:YAG being constant over the plotted temperature range [74], the peak emission cross section decreases approximately by $0.21\%/K$.

Applying the Model to the Microchip Laser

From section 2.3 about thermal lensing, we know that the temperature profile within an end-pumped laser crystal varies with a rather steep slope both perpendicular and parallel to the optical axes. Within the volume of the laser mode the laser crystal has a wide range of temperatures $T(r, z)$. In order to simulate the

spectral profile of the emission cross section, a spatially averaged temperature T_{avg} could be used.

$$T_{avg} = \frac{1}{V_g} \int_{V_g} T(r,z) dV \quad \text{with} \quad V_g = 2\pi w_g l_g \tag{4.17}$$

This approximation ignores the shift in wavelength of the single emission cross-section spectra along the temperature gradient within the laser mode volume V_g. With the position of the emission peak varying with temperature and the temperature varying within the gain crystal the total emission profile is smeared out and thus wider than presumed by this approximation.

An approximation that is closer to the actual emission cross-section spectrum can be found by integrating all temperature profiles $\sigma(\lambda, T(r,z))$ within the crystal weighted by their contribution to the initial gain $d\phi/dt \propto \phi\sigma_g n_g$. This method provides the emission cross-sectional profile during the pulse build-up time, where the population $n_g \approx n_i$ is not reduced considerably. For the weighting of the single emission cross-section spectra, we are going to define a normalized gain factor f_{gain} by

$$f_{gain}(r,z) \propto e^{-\alpha z} e^{-2\frac{r^2}{w_p^2}} e^{-2\frac{r^2}{w_g^2}} \quad \text{with} \quad \int_{V_c} f_{gain}(r,z) dV = 1, \tag{4.18}$$

where the integral is done over the whole laser crystal volume V_c and the population n_g was replaced by the local pumping rate from 2.35. An averaged weighted emission cross section within the laser mode volume can be retrieved by

$$\sigma_{g,avg}(\lambda) = \int_{V_c} \sigma_g(\lambda, T(r,z)) \times f_{gain}(r,z) dV. \tag{4.19}$$

The temperature profile within the gain medium and the averaged emission cross sections for the proposed microchip laser are shown in figure 4.5. The temperature profile shows a high peak temperature of over 70 °C due to the used strong pumping power that is necessary for the chosen PRF of 5 kHz. The spatially averaged emission cross section spectra $\sigma_{g,avg}$ and $\sigma_g(T_{avg})$ show clearly the difference between the two possible averaging methods.

The change in the emission cross section spectrum will have several effects on the performance of the proposed microchip laser. For one the emission peak wavelength will change with temperature and thus the wavelength of the emitted pulses will vary with the pumping power. The other is an increase in pulse energy with crystal temperature. When the emission cross section of the gain medium becomes smaller, the initial population inversion has to raise to higher levels before the saturable absorber can bleach out. Hence, more energy gets stored in

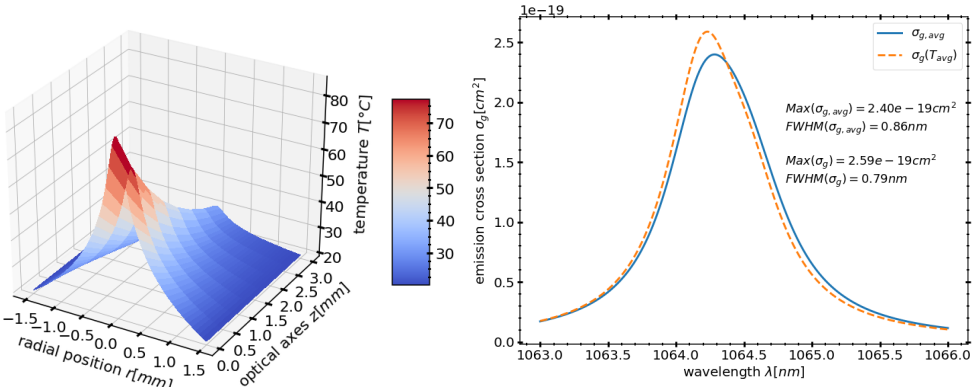

(a) *Temperature profile* **(b)** *Average emission cross sections*

Figure 4.5: *(a) Temperature profile inside the gain medium of the proposed microchip laser (Table 2.1) pumped at 5 kHz repetition rate (PRF). (b) Average weighted emission cross section $\sigma_{g,avg}$ plotted together with emission cross section for averaged temperature $\sigma_g(T_{avg})$. Values for the respective peak emission cross sections and the FWHM of the spectra are given.*

the gain medium before a laser pulse is extracted. This effect is comparable to a decrease in the initial transmission of the saturable absorber, which increases the pulse energy and shortens the pulse duration. This of course presumes that the saturable absorber crystal, which will also heat up during operation, does not change its absorption cross section with temperature. That was shown to be the case for Cr^{4+}:YAG crystals by Okhrimchuk and Shestakov [75].

Figure 4.6 compares the change in pulse energy over increased repetition rate (PRF) of the proposed microchip laser for two cases. One time the simulation was run with a constant emission cross section, the other time a temperature dependent emission cross section was used. At low repetition rates and thus at low pumping power, both models show the same pulse energy. This is expected, as at low repetition rates the gain crystal does not heat up much. With increasing repetition rate the pulse energies for both models start to drop, as the thermal lensing gets stronger and thus the laser mode width shrinks. At the same time the two models start to drift apart from each other, as the effect from the temperature dependent emission cross section kicks in. An interesting aspect of the proposed microchip laser appears in the simulation at very high repetition rates around 4 kHz. The increase in pulse energy due to lowered emission cross section starts to compensate the drop in energy due to thermal lensing. Following these simulations, it is expected that the drop in pulse energy will settle at a constant value at very high repetition rates.

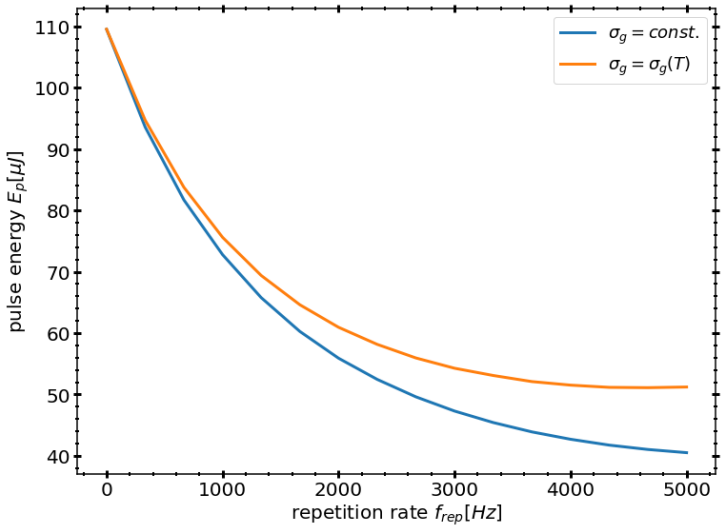

Figure 4.6: *Simulated pulse energy of the proposed microchip laser over repetition rate (PRF). Either a constant emission cross section ($\sigma_g = const.$) or a temperature dependent averaged weighted emission cross section ($\sigma_g = \sigma_g(T)$) is used.*

4.3 Modulated Photon Field

The Q-switched microchip laser has been described with a time varying but spatial homogeneous photon-density $\phi(t)$. But the photon-field within a laser cavity is actually a standing electromagnetic wave that has both amplitude and phase. Hence, the photon-field inside the cavity should also be described with a phase-modulation analogue to the electric field. A possible description would be a sinusoidal modulation along the optical axes z analog to the sinusoidal modulated electric field with

$$\phi_q(t,z) = 2\phi_{q,0}(t)\sin^2(2\pi\frac{z}{\lambda_q}) \tag{4.20}$$

$$\phi_{q,0}(t) = \frac{1}{l_g}\int_{z_{g,0}}^{z_{g,1}} \phi_q(t,z)dz \tag{4.21}$$

where $\phi_{q,0}(t)$ is the space-averaged photon density and λ_q is the wavelength of the q-th longitudinal mode. The integral within the averaged photon density is performed only along the gain medium, so from $z_{g,0}$ to $z_{g,1}$. This description has the advantage that the photon density can be separated into a time dependent amplitude and a time independent spacial component.

For the time derivative of the population inversion $\frac{dn_g(t,z)}{dt}$ on the other hand, the population density has to be split into thin slices Δz, which should be far

smaller than the wavelength ($\Delta z << \lambda_q$). This will result in $N = \frac{l_g}{\Delta z}$ separately numerically solvable differential equations. For each slice $n_q(t)_z$ the equations for the gain medium and the saturable absorber are

$$\frac{dn_g(t)_z}{dt} = -c\sigma_{g,q}\phi_q(t,z)n_g(t)_z \tag{4.22}$$

$$\text{with} \quad z = z_0 + N \times \Delta z \quad \text{and} \quad N = 0 \dots l_g/\Delta z. \tag{4.23}$$

$$\frac{dn_{abs}(t)_z}{dt} = -\sigma_{abs}c\phi_q(t,z)n_{abs,0}(t)_z \tag{4.24}$$

$$\text{with} \quad z = z_0 + N \times \Delta z \quad \text{and} \quad N = 0 \dots l_{abs}/\Delta z. \tag{4.25}$$

Here it was assumed that the emission cross section for the gain medium $\sigma_{g,q}$ can be different for each longitudinal mode q, but the cross sections for the saturable absorber do not differ much between the excited modes.

As the photon density can be separated into a spatial and a temporal part, it does not have to be sliced up. Instead, the spatially averaged inversion densities $n_{g,q,avg}(t)$ and $n_{abs,q,avg}(t)$ are going to be defined, which are weighted by their photon field modulation. The averaged densities will have to be calculated for each time step during the numerical integration along the time domain.

$$n_{g,q,avg}(t) = \frac{1}{l_g}\int_{z_{g,0}}^{z_{g,1}} 2\sin^2(2\pi n\frac{z}{\lambda_q})n_g(t,z)dz \tag{4.26}$$

$$n_{abs,q,avg}(t) = \frac{1}{l_{abs}}\int_{z_{abs,0}}^{z_{abs,1}} 2\sin^2(2\pi n\frac{z}{\lambda_q})n_{abs,0}(t,z)dz \tag{4.27}$$

The averaged population densities can be used to define a time-only dependent differential equation for the photon field's space-averaged amplitude with

$$\frac{d\phi_{q,0}(t)}{dt} = \frac{\phi_{q,0}(t)}{t_{rt}}(2\sigma_{g,q}n_{g,q,avg}(t) - 2\sigma_{abs}n_{abs,q,avg}(t) - [...]) \tag{4.28}$$

This new set of rate equations include the effects of a modulated optical field for a pulse with a single longitudinal mode. In Figure 4.7 the modulated photon density $\phi_q(z)$ is plotted together with the modulated final population inversion $n_{g,final}(z)$ of the gain material and the final population density of the ground state of the saturable absorber $n_{abs,final}(z)$. The parameters from the proposed microchip laser from table 3.2 are used for this calculation. The final populations are strongly modulated for both the gain material as for the saturable absorber. The simulation shows that after a laser pulse is extracted, a rather large population inversion still remains, especially at the points where the modulated photon density

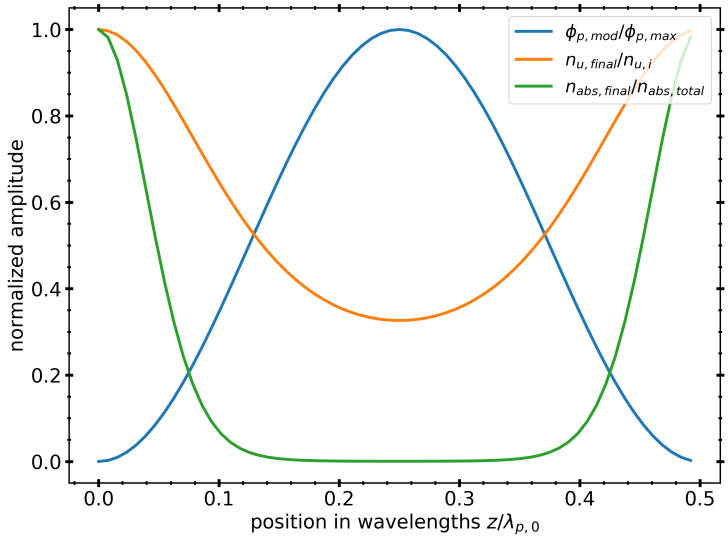

Figure 4.7: *Solution for the rate equations which include a spatially modulated photon density $\phi_p(z)$. Data is plotted for the range of half a wavelength (wavelengths corrected with the refractive index of the material). The microchip geometry from table 3.2 is used. Plotted are also the modulated final population of the upper laser level $n_{u,final}$ and the population of the ground level of the saturable absorber n_{abs}.*

is zero or close to zero. This modulated depletion in population is called spatial hole burning. As a direct result of spatial hole burning, the extracted energy is smaller than in the unmodulated case.

To see how much less energy is extracted from the cavity of the proposed microchip laser, the rate equations are solved and the photon density and the spacial averaged population densities are plotted for both the modulated and the unmodulated case in figure 4.8. In the case of a modulated photon field, the average final population density of the upper laser level settles at around 60% of its initial level, whereas in the unmodulated case the population density drops to roughly 40% of its initial value. The extraction efficiency is thus lower for a modulated photon field and the resulting pulse energy drops from 78 µJ to 53 µJ.

Figure 4.8 also shows the population of the saturable absorber's ground state after the laser pulse has been extracted. A rather big part centered within each period $\lambda_{q,1}/2$ is completely bleached out and only in the areas close to the electric field's zero-points a population is left in the ground state. The saturable absorber is bleached out by roughly 80% on average, whereas only 40% of the inversion in the gain medium are extracted. It is plausible at this point, that a second laser pulse running in a different longitudinal mode might extract parts of the remaining inversion.

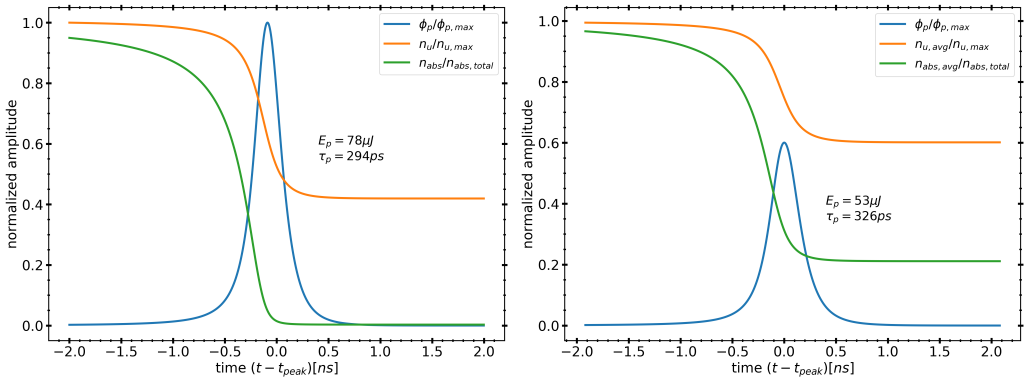

(a) *Solution with constant photon field* **(b)** *Solution with modulated photon field*

Figure 4.8: *Solutions of the rate equations for Q-switched microchip laser from table 3.2, with spatially constant photon field (a) and with spatially modulated photon field (b). Amplitudes are normalized to their maximum value. Plotted are the photon densities ϕ_p normalized to the maximum in case of infinite thermalization rate, spatially averaged population density n_u of the upper laser level and the spatially averaged population density n_{abs} of the saturable absorbers ground state.*

4.4 L-Mode Satellite Pulse

In chapter 2.2, it is shown that two neighboring longitudinal modes overlap constructively at the end mirrors, but they drift apart towards the cavity center. After a single longitudinal mode laser pulse is extracted from the cavity, it leaves a spatially modulated residual inversion in the gain medium. That inversion might be high enough to generate a second trailing pulse running in a different longitudinal mode. Figure 4.9 shows the emission cross section spectrum of Nd:YAG for room temperature together with a few possible longitudinal modes of the proposed microchip laser. The mode with the highest cross section (L-Mode 0) represents the first laser pulse extracted from the microchip. The possible second laser pulse can have any direct or next neighboring longitudinal mode depending on its emission cross section and its spatially averaged population inversion.

From the last simulation in the previous section, which included the spatially modulated rate equations, the final population density $n_{g,final}(z)$ can be used in conjunction with possible laser modes $\phi_q(z, \lambda_q)$ to see if the gain, respectively the time derivative of the photon density, is above zero. The resulting condition

$$\frac{d\phi_{q,0}}{dt} \propto (2\sigma_{g,q} n_{g,q,avg} - 2\sigma_{abs} n_{abs,0,avg} - [...]) > 0 \tag{4.29}$$

contains only the second multiplier of $\frac{d\phi_{q,0}}{dt}$, which is enough to see if there

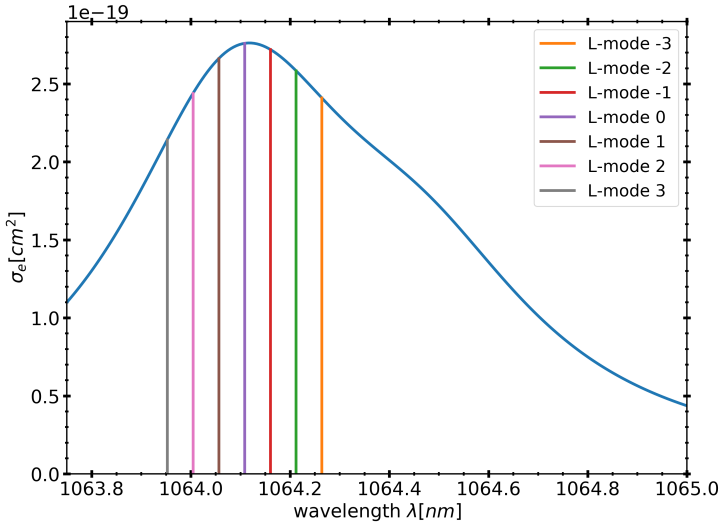

Figure 4.9: *Emission cross section spectrum of Nd:YAG plotted together with longitudinal modes of the proposed microchip laser described in table 2.1. Operation at 1 kHz PRF. L-modes are designated with numbers from -3 to +3. The center L-mode 0 has the actual mode number of* $q = 20493$.

is a positive gain. Table 4.1 shows the values for $\frac{d\phi_{q,0}}{dt}$ (excluding the term $\frac{\phi_{q,0}}{t_{rt}}$) after the first laser pulse is extracted. For the center mode (L-Mode 0) most of the spatially averaged inversion is already extracted by the first laser pulse, and thus the gain here is negative. One neighboring mode (L-Mode -1) on the other hand shows a raise in photon density, which indicates that a trailing pulse is building up after the first pulse is extracted.

L-Mode (q)	-2	-1	0	1	2
$\propto \frac{d\phi_0}{dt}$	-0.28	0.22	-0.34	-0.09	-0.53

Table 4.1: *Values proportional to* $\frac{d\phi}{dt}$ *according to equation 4.29 for different longitudinal modes* q *after the extraction of the first laser pulse.*

To see which characteristics the predicted trailing pulse has, the rate equations can be further extended to include several competing longitudinal modes. Several parameters and properties with their dependency on the laser mode number q have been introduced in the previous section. Both the emission cross section $\sigma_{g,q}$ and the modulated photon field $\phi_q(t, z)$ are wavelength dependent. The averaged populations $n_{g,q,avg}(t)$ and $n_{abs,q,avg}(t)$ that overlap with the photon-field are dependent on the modes wavelength and are thus marked with the mode number q. The new set of rate equations will have to include several possible photon fields

ϕ_q, each of which will diminish the population further. The single photon fields ϕ_q are treated as if they would not interfere with each other. This is a reasonable assumption as a time-independent phase-offset between the single modes like in a mode-locked system is missing. It is reasonable to assume that the single intensity fields with mode numbers q can be summed up without interference terms. The rate equation for the photon density ϕ_q from the model before (equation 4.28) can be reused, but it has to be solved for each mode q separately. The rate equations for the population densities in the case of multi-longitudinal modes are

$$\frac{dn_g(t)_z}{dt} = -cn_g(t)_z \sum_q \sigma_{g,q}\phi_q(t,z) \tag{4.30}$$

$$\text{with} \quad z = z_0 + N \times \Delta z \quad \text{and} \quad N = 0 \ldots l_g/\Delta z. \tag{4.31}$$

$$\frac{dn_{abs}(t)_z}{dt} = -cn_{abs,0}(t)_z\sigma_{abs} \sum_q \phi_q(t,z) \tag{4.32}$$

$$\text{with} \quad z = z_0 + N \times \Delta z \quad \text{and} \quad N = 0 \ldots l_{abs}/\Delta z. \tag{4.33}$$

The new set of rate equations for multi-longitudinal mode lasing are solved and the results are shown in figure 4.10. The first laser pulse with mode $q = 0$ is identical to the pulse from the previous single longitudinal mode simulation. The remaining spatially averaged upper laser level population of roughly 60% of its initial value is high enough to generate a second laser pulse. The second laser pulse with the relative mode number $q = -1$ has a far shorter pulse build-up time t_{peak} than the first. This is due to the saturable absorber being nearly bleached out during the first pulse build-up. The second pulse can thus be seen as a mix between Q-switched and gain-switched pulse. Its pulse duration is accordingly longer than the fully Q-switched pulse. The simulation shows that the second laser pulse extracts another 10% of the stored population.

To keep in line with previous publications and name giving, the trailing pulse running in a different longitudinal mode is called an L-mode satellite pulse within this work. The simulation shows that L-mode satellite laser pulses are expected to appear in the proposed microchip laser. In order to see which time delays between the main pulse and the satellite pulse are expected for the proposed microchip laser at varying temperatures and PRFs, the multi-longitudinal mode simulations where conducted in a series with varying crystal holder temperature and at three different repetition rates (PRFs). The results are shown in figure 4.11. The average delay between the two pulses for all shown repetition rates is 8.4 ns. An interesting feature appears at each repetition rate. There is a maximum delay between the two pulses which appears at a certain temperature. At these points the difference between the emission cross sections of the two pulses is at its maximum. Due

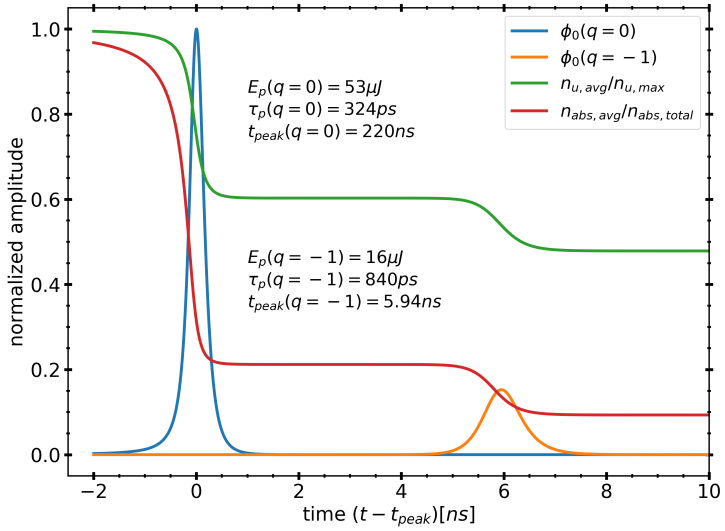

Figure 4.10: *Simulation results for multi-longitudinal mode lasing of the proposed microchip laser. Shown are the spatially averaged amplitudes of the photon densities with L-mode numbers* 0 *and* -1*, both normalized to the peak value of* $\phi_0(q=0)$*. The spatially averaged population densities for the upper laser level* $n_{u,avg}$ *and for the ground state of the saturable absorber* $n_{abs,avg}$ *are both normalized to their respective peak values. Given are also the pulse energies* E_p *and the pulse durations* τ_p *of the generated pulses. The pulse build-up times* t_{peak} *for both pulses are measured from the pulse onset to its peak.*

to the minimized cross section for the satellite pulse, it needs more time to build up. Another interesting property of the L-mode satellite pulses is that at certain temperatures the delay to the main pulse vanishes. At these points the emission cross sections for both modes are very close to each other and both reach their inversion threshold nearly at the same time. The two pulses temporarily overlap with each other. Due to their separation in wavelengths this temporal overlap will result in mode-beating, which is discussed in more detail in the following section.

The L-mode satellite pulses described in this section differ from the previously described L^3-satellite pulses (see section 4.1) considerably, as they run in a different longitudinal modes. The first experimental observations of a L-Mode satellite pulse can be found by Bartschke *et al.*[76]. They used Nd:YAB (Neodymium doped Yttrium Aluminium Borate) as both gain medium and nonlinear crystal for frequency doubling. The measurements of the temporal profiles of the output pulses showed a trailing pulse for each main pulse. A look at the spectrum revealed that the two pulses had different wavelengths and their separation could be explained by being two neighboring longitudinal modes. The given cause for the second L-mode was spatial-hole burning, which coincided with the model in this

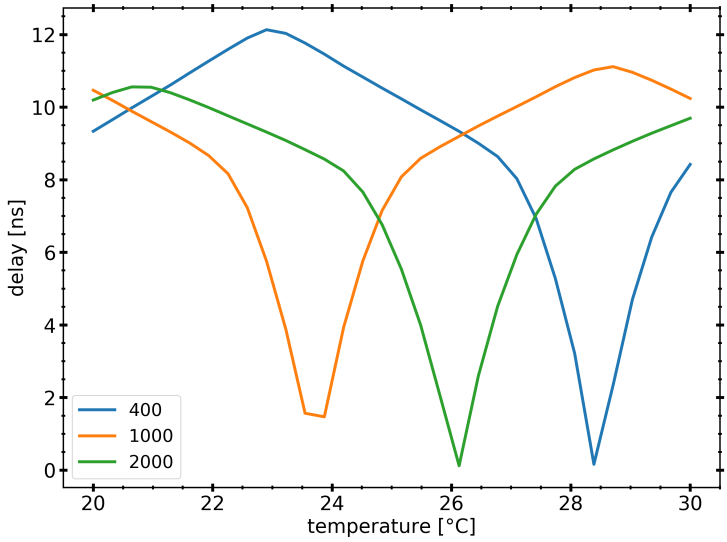

Figure 4.11: *Simulation results for multi-longitudinal mode lasing of the proposed microchip laser. Shown are the time delays between the main pulse and the L-mode satellite pulse. The data is plotted along varying crystal holder temperature and for different pulse repetition frequencies (from 400 to 2000 Hz). A satellite L-mode pulse is observed in every run of the simulation.*

work.

A satellite laser pulse following the main pulse with a different L-mode and with a far lower energy was also reported by Niu *et al.*[77]. An explanation on why or how the second laser pulse was generated is not given by the author, but from his report it is clear that it was an L-mode satellite pulse. Later Liu *et al.*[78] also produced L-mode satellite pulses. By correlating the appearance of the satellite pulses with extra modes seen on a high resolution spectrometer, they showed that these pulses correspond to different longitudinal modes.

4.5 Mode Beating

Due to the modulation of the electric field inside the gain material, several laser modes can be generated independently. This multi-longitudinal mode lasing can result in several effects. The simulations in the previous section shows that a trailing pulse is generated after the main pulse was extracted. As a special case, this second laser pulse or L-mode satellite pulse can be formed at nearly the same time as the main laser pulse. In the simulations from the previous chapter it is shown that this can occur at every set repetition frequency, but only at certain temperatures (see figure 4.11).

Two longitudinal modes might have very similar emission cross sections. As a consequence these two modes reach threshold either at the same time or very close to each other. These two neighboring modes compete for the population inversions in that part of the gain medium, where their photon-field is in phase. To visualize this effect and to investigate it further, the derived simulation model can be used. In figure 4.12 the emission cross sections for several longitudinal modes within the proposed microchip laser (MC01) pumped at 400 Hz are shown along varying crystal holder temperature. For the calculation the model for temperature dependent emission cross section of Nd:YAG is used. As the wavelengths of the single longitudinal modes are fixed, their cross sections shift with changes in temperature. At certain temperature points the cross sections of two neighboring modes are identical. At a crystal holder temperature of $25.75°C$, the two central modes have the same emission cross section, which should result in temporally overlapping laser pulses.

Using the multi-longitudinal mode model on the proposed microchip laser with the crystal holder temperature set to $25.73°C$, in fact two temporally overlapping laser pulses are generated, which can be seen in figure 4.13. The temperature was chosen to be slightly off the previously determined point at $25.75°C$ to get slightly different pulse amplitudes in the two overlapping pulses. The two generated laser pulses with absolute L-mode numbers 20463 and 20464 differ from each other. The mode 20464 features a higher emission cross section, which can also be seen in figure 4.12. As a direct result, this mode starts lasing first. The temporal delay is not a result of the needed extra pumping time but of the bleaching of the saturable absorber by the first laser pulse. The second pulse can thus be seen as a mixed Q-switched gain-switched pulse and its pulse duration is longer than in the pure Q-switched case. The two pulses have differed wavelengths and the output of the laser is a pulse with a modulation frequency $\Delta f_{1,2}$ defined by the difference in wavelengths.

This mode-beating effect can be interpreted as a special case of the L-mode satellite pulse effect. Mode-beating is expected to happen with the proposed mi-

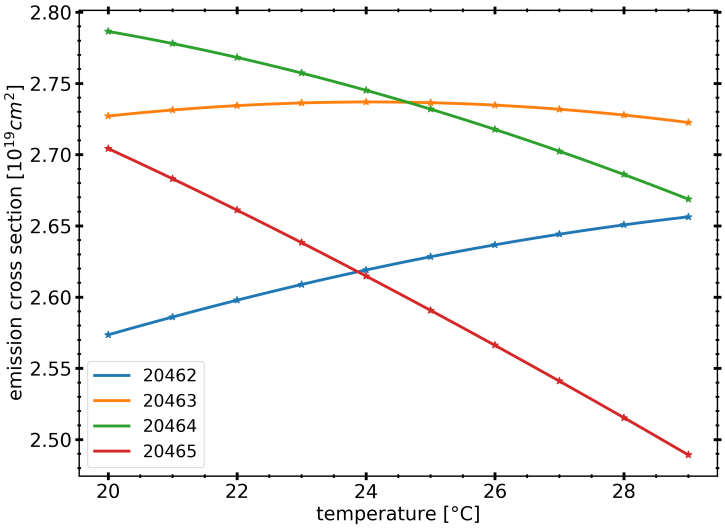

Figure 4.12: *Simulated emission cross sections of the single longitudinal modes of the proposed microchip laser (MC01) pumped at 400 Hz. The given numbers in the legend are the absolute q-numbers. The crystal holder temperature is varied between* $20°C$ *and* $30°C$*. Within this temperature range the L-modes 20463 and 20464 feature the highest emission cross sections. Their emission cross sections overlap at a temperature of* $25.75°C$*.*

crochip laser for every repetition frequency but only at certain temperatures. To avoid the mode-beating effect, the proposed Q-switched microchip laser has to be temperature stabilized.

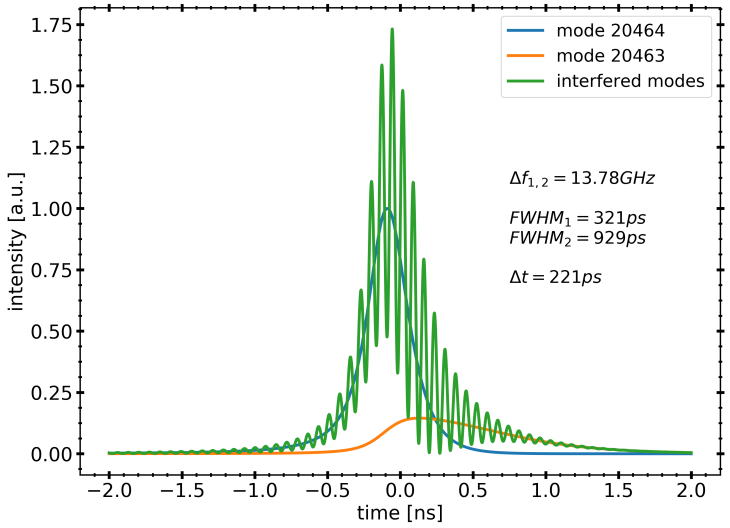

Figure 4.13: *Solution for the model for multi longitudinal modes of the proposed microchip laser (MC01) pumped at 400 Hz solved for a crystal holder temperature of* $25.73°C$*. Two longitudinal modes are overlapping in time. Their interfered signal is modulated with a frequency* $\Delta f_{1,2}$ *due to their slightly different wavelengths. Given is also the FWHM pulse duration and the time delay* Δt *between the peaks of the two interfering pulses.*

4.6 Mode Hopping

Between the generated laser pulses the gain medium is pumped until the needed initial population is reached again. Experimentally it makes sense to pump the microchip laser not continuously but in pulsed mode. This pulsed pumping reduces the losses due to the finite lifetime of the upper laser level. With the repetition frequency of the pulsed pump, the pulse repetition frequency (PRF) of the microchip laser can be set. The duration of a single pump pulse is set as long as needed to reach the initial inversion.

If the time between two consecutive pulses is in the range of the upper laser level lifetime or shorter, part of the not extracted upper level population is preserved and can be used by a pulse from the second pumping cycle. In the case of the proposed microchip laser, the final population inversion is strongly modulated after the main and the trailing L-mode satellite pulses are extracted from the cavity. If the modulated inversion partly remains until the pulse of the following cycle is generated, then the mode of the main pulse might hop to a neighboring mode. To investigate this effect, the final populations of the previous simulations can be used as a starting point. The population of the upper laser level then is reduced by its decay rate over the time period between two consecutive main pulses and a

population according to the pumping rate is added. From there the same model as before is used, but this time with the mixed and thus modulated population density as a new starting point.

The simulation is performed with a fixed repetition frequency of 1 kHz, and the energies and mode-numbers of the generated main and trailing pulses are shown in Table 4.2. It can be seen that indeed the consecutive main pulses exhibit a mode hopping between the $q = 0$ and $q = -1$ mode and that the trailing pulses also hop between these two modes. What can also be seen is that the pulse energies of the trailing pulses fluctuate between pulse-cycles, which can be explained by the difference in emission cross sections for each laser mode.

L-Mode	-2	-1	0	1	2
	0	16.6	53.1	0	0
	0	53.1	16.8	0	0
	0	16.1	53.1	0	0
	0	53.1	16.8	0	0
	0	16.1	53.1	0	0

Table 4.2: *Given values are the pulse energies E_p[μJ] for the repeatedly solved rate equations. First row represents the first pulse (L-mode 0) plus trailing pulse (L-mode -1) after the first pumping cycle. Second row represents the pulses after the second pumping cycle, etc. Final population densities after each cycle are reduced by their lifetime and then added to the inversion of the following pumping cycle. Simulations where done for the proposed microchip design operated at 1 kHz PRF.*

The mode-hopping between the laser pulses in the microchip laser strongly depends on the ratio between PRF and upper laser level lifetime. Further simulations of the proposed microchip laser with different repetition frequencies showed no mode-hopping effects for PRFs below 500 Hz. Starting between 500 and 1000 Hz mode-hopping appears, which depended on the set crystal temperature. Comparing the lifetime of the upper laser level of Nd:YAG, which is about 230 µs, and the time delay between pulses at 1 kHz, which is 1000 µs, it can be seen that only 1.3% of the modulated final population is already enough to get mode-hopping effects. In other words, the proposed microchip laser should be very susceptible to mode-hopping, especially at high PRFs of 1 kHz and above.

The same approach can also be used to look at consecutive pulses for even higher PRFs. If the microchip laser is pumped at a raised PRF, the crystal will heat up more. As the emission cross section spectrum is temperature dependent, it has to be recalculated according to the model given in section 4.2. The weighted emission cross section spectrum is shown in figure 4.14. The profile is considerably wider than in the case of operation at 1 kHz PRF. Its full width at half

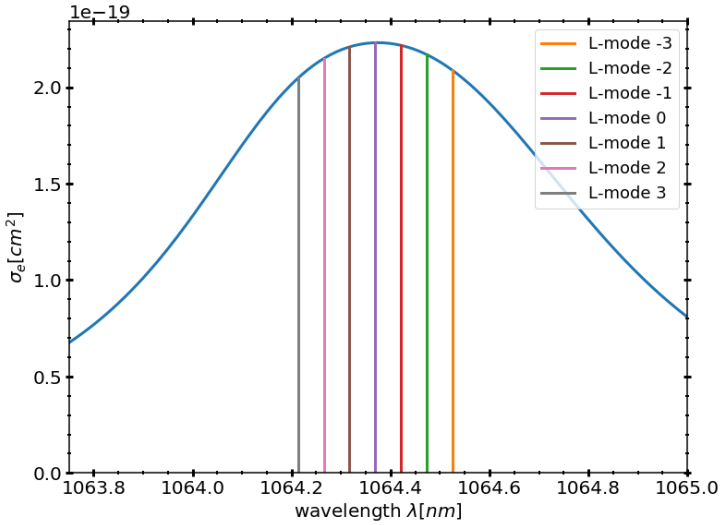

Figure 4.14: *Initial gain weighted emission cross section spectrum of Nd:YAG plotted together with longitudinal modes of the proposed microchip laser described in table 3.2. Laser is operated at 5 kHz repetition frequency with accordingly higher gain medium temperature. The emission spectrum is wider than in the 1 kHz case.*

maximum widened from 0.77 nm at 1 kHz to 0.93 nm at 5 kHz. As a result, the single longitudinal modes experience a more similar emission cross section. The trailing pulse condition 4.29 which checks the gain after the first pulse is extracted is shown in table 4.3. Both next neighboring modes $q = -1$ and $q = 1$ have a positive gain after the main pulse ($q = 0$) is extracted, thus two trailing pulses are expected. The continued simulation in time is shown in Figure 4.15, where two trailing pulses can be observed within the simulation. They overlap in time, but their energies are quite different from each other.

L-Mode (q)	-2	-1	0	1	2
$\propto \frac{d\phi_0}{dt}$	-0.27	0.34	-0.37	0.34	-0.28

Table 4.3: *Values proportional to $\frac{d\phi}{dt}$ according to equation 4.29 for different longitudinal modes q after the extraction of the first main laser pulse. Simulation performed for proposed microchip laser operated at 5 kHz.*

Table 4.4 shows the pulse energies of consecutive pulses for the proposed microchip laser operated at 5 kHz PRF. Due to more inversion preservation between the pulses, the mode-hopping is much more severe than at 1 kHz. Interestingly the main mode changes between pumping cycles between $q = 0$ and $q = 1$. Apparently the emission cross sections for these two modes must be very similar. What

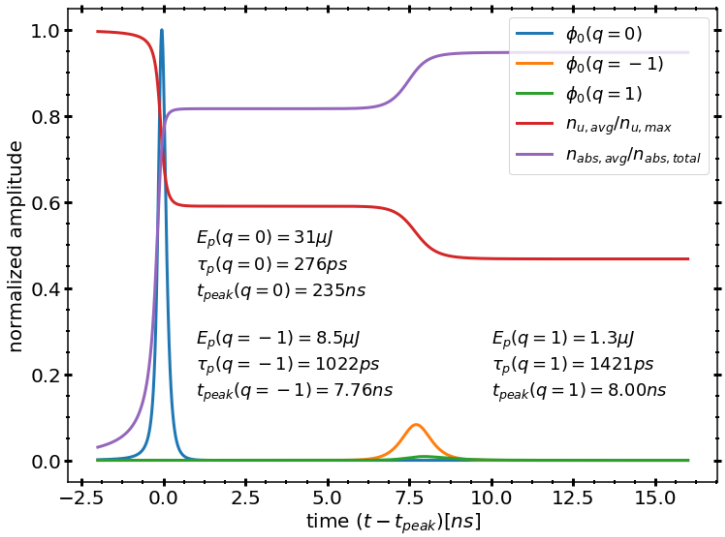

Figure 4.15: *Simulation results for multi-longitudinal mode lasing of the proposed microchip laser operated at 5 kHz. Shown are the spatially averaged amplitudes of the photon densities ϕ_0 of the laser pulses with L-mode 1, 0 and -1 normalized to the peak value of $\phi_0(q=0)$. The spatially averaged population densities for the upper laser level $n_{u,avg}$ and the excited state of the saturable absorber $n_{abs,avg}$ are both normalized to their total peak values. Given are also the pulse energies E_p and the pulse durations τ_p for each mode. The pulse build-up times t_{peak} are measured from the pulse onset to its peak.*

can also be seen from the simulation, is that both the total pulse energies (sum) and the energy of the main pulses fluctuate between cycles.

For the proposed microchip laser, mode hopping is expected to happen at raised PRFs, starting around 1 kHz. The fluctuations in pulse energy seem not to be severe. The fluctuation in total pulse energy is within a 1% window and the fluctuation of the energy of the main pulse is also around this value. In experimental conditions there will be also externally induced fluctuations like in temperature and also fluctuations in pumping power due to imperfect pumping electronics and diodes. This will be looked at in more detail within the experimental chapter.

Mode-hopping is known to happen in Q-switched microchip lasers. Dong *et al.*[79] investigated on two-mode oscillation in a 1 mm short Nd:YAG based Q-switched microchip laser. The laser experienced mode-hopping which was attributed to spatial-hole burning effect. The easiest way to achieve mode hopping is when a gain material with a wide emission cross section spectrum is used and neighboring modes have very similar emission cross sections. Dong *et al.*[80] studied multi-longitudinal mode lasing of a Yb:YAG based Q-switched microchip laser. The laser started mode-hopping at pumping powers as low as 0.33 W. At higher pumping powers up to four longitudinal modes were observed. This be-

L-Mode (q)	-2	-1	0	1	2	sum
	0	8.8	30.4	2.7	0	39.2
	0	0	0.8	30.6	7.7	39.1
	0	9.6	30.2	0	0	39.8
	0	0	0.8	30.7	8.0	39.4
	0	9.6	30.2	0	0	39.8
	0	0	0.8	30.7	8.0	39.5
	0	9.6	30.2	0	0	39.8
	0	0	0.8	30.7	8.0	39.5
	0	9.6	30.2	0	0	39.8

Table 4.4: *Given values are the pulse energies $E_p[\mu J]$ for the repeatedly solved rate equations. The first row represents the first pulse plus the two trailing pulses. The second row represents the pulses after the second pumping cycle, etc. Final population densities after each cycle are reduced by their lifetime and then added to the inversion of the following pumping cycle. Besides the values for pulse energies $E_p[\mu J]$ within each L-mode q, the sum over all modes within one cycle is also given (sum). Simulations were done for 5 kHz PRF.*

havior was attributed to spatial hole burning effects in both the gain medium and the saturable absorber, which coincides with the findings in this work.

4.7 Discussion

In the theory chapter a model for calculating the laser pulse parameters for a given Q-switched microchip laser design has been given (chapter 2). This model was extended within this chapter to include several effects. The first extension of the model includes the lower level lifetime of the gain material (section 4.1). It was shown that this effect raises the pulse duration of the proposed microchip laser (MC01) and lowers its pulse energy. For certain Q-switched laser designs the lower level lifetime can lead to the generation of a satellite pulse. This was observed by Ng *et al.*[69], where a gain medium with a long lower level lifetime in the order of nanoseconds was used (Nd:$GdVO_4$). The simulations showed that this kind of satellite pulses are not expected to be generated by the proposed microchip laser design. The lifetime of the lower laser level of Nd:YAG with a value of 225 ps is short enough to depopulate the lower level within the laser pulse duration of 200 to 400 ps.

A model for the temperature dependence of the emission cross section spectrum of Nd:YAG was introduced (section 4.2). This effect lowers the peak emission cross section of the gain medium with increased heat deposition. It was shown that the lowered emission cross section at increased PRFs leads to an increase in pulse energy. At very high PRFs around 4 kHz, this increase can compensate the loss in pulse energy induced by thermal lensing.

A major extension to the model of Q-switched microchip lasers is the introduction of a modulated photon field inside the cavity (section 4.3). This extension enables the modeling of multi-longitudinal modes within the cavity. Several new effects have been derived from this extension: The generation of L-mode satellite pulses, mode beating and mode hopping (sections 4.4 to 4.6). In case of the proposed microchip design, trailing pulses in the form of L-mode satellite pulses are expected to appear within the experiments. Mode-hoping is expected to occur at PRFs starting between 500 and 1000 Hz together with the effect of mode-beating.

Chapter 5

Q-Switched Microchip Experiments

The proposed microchip design (MC01) as a new oscillator for the NextGenPIRL is set up and characterized. The model for temperature dependent emission cross section is used to compare the measured spectra to the given model from section 4.2. Due to a strong deviation of the measured spectral shift within the gain medium and the calculated temperature distribution within the crystal, a finite volume solver is introduced to get more precise results for the modeled emission spectrum.

The generated pulses are characterized regarding their pulse duration and pulse energy. A rather complex model was developed in the previous chapters to simulate the lasing behavior within the microchip laser. An overview of the used extensions is given, the proposed microchip laser is simulated and the results are compared to the measurements.

In the previous chapter 4 a model has been derived to simulate multi longitudinal mode lasing within the proposed microchip laser. Several effects have been identified and predictions have been made to when multi-mode lasing starts and which effects should occur. Within the section 5.4 these effects are reproduced experimentally and studied in detail.

5.1 Laser Setup

The proposed microchip design (MC01) consists of a 2.5 mm long, 1.1 at.% doped Nd:YAG crystal bonded on a 2.5 mm long Cr^{4+}:YAG crystal with an initial transmission T_0 of 20 %. Both end-faces are capped with a 0.5 mm long undoped YAG crystal to suppress bulging of the end-faces and to enhance the longitudinal heat flow. The input side is HR coated for the lasing wavelength at 1064 nm and AR coated for the pump wavelength of 808 nm. The output side has a partial reflectivity of 30 %. Both end-faces exhibit a slight curvature due to the manufacturing process. When polishing the end-faces of a crystal, a curvature of that surface is happening because of the crystal sinking slightly into the polishing mate. High care has to be taken to keep the resulting curvature of the surface limited to the substrates outer edges, so that the center part stays flat. This is particularly tricky when the substrate has a small surface area, like in the case of the used microchip design. The curvature of the available microchip laser is estimated with a radius of 400 mm. This design is very close to the HPMCL-3 design by Zayhowski, but considerably shorter. The two designs are compared in table 3.2.

The fiber coupled Volume Bragg Grating (VBG) stabilized pump diode with a maximum optical power of 30 W and a fiber core diameter of 200 µm is placed on a temperature controlled copper mount. The pump beam after the fiber is collimated with a 50 mm focal length lens and focused inside the Nd:YAG crystal with a 25 mm lens. The pump beam has a diameter of around 120 µm ($1/e^2$) at the focal spot and the M^2 was measured to be 46. The diode's emission spectrum is due to its VBG stabilization far more narrow than in the case of an un-stabilized diode (see figure 5.1). The spectral narrowing is a direct result of the diode's output coupler being wavelength selective. With a spectral width $\Delta\lambda_{FWHM}$ of only 0.20 nm and a wavelength drift $d\lambda/dT$ of 0.08 nm/ °C the pump diode's output spectrum is already centered close to the highest absorption peak of the $I_{9/2} \rightarrow F_{5/2}$ transition of Nd:YAG and an absorption of up to 98% of the pump light can be achieved in the gain medium of the MC01 laser.

The microchip laser is carefully pressed inside a temperature controlled copper mount using thin Indium foil as a buffer to enhance thermal conductivity between the crystal and the copper heat sink. Special care was taken to press the crystal not too hard within the mount to ensure that no birefringence was induced. In the first experiments the copper mount of the microchip crystal was held at a constant temperature of 20 °C by a thermoelectric cooling device.

Several measurement devices were available during the experiments. The pulse energy was measured with a fast energy meter, that was able to measure pulse energies at PRFs up to 25 kHz. The temporal profile of the generated pulses were measured with a fast 16 GHz photo-diode and a sampling oscilloscope with

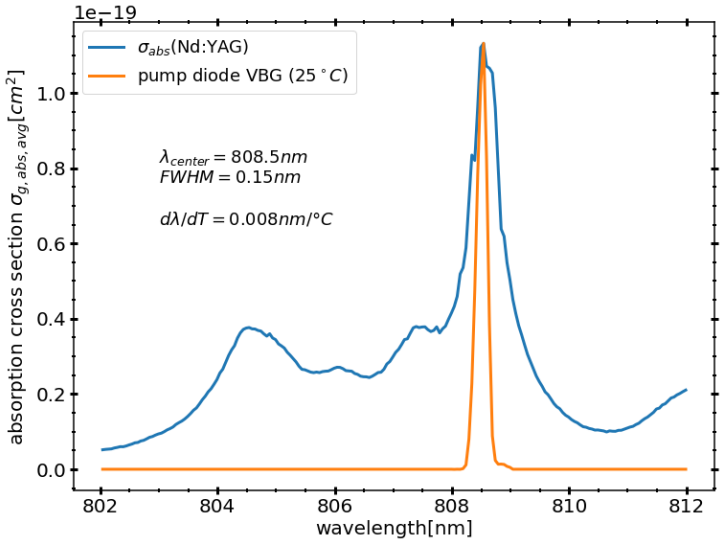

Figure 5.1: *Spectrum of the VBG stabilized fiber-coupled diode laser [a.u.], operated at 40% duty cycle and at 25 °C heat sink temperature. Shown is also the absorption cross section σ_{abs} of 1.0 at.% doped Nd:YAG, taken from Kellner [81].*

a bandwidth of 16 GHz. Spectra where taken with a spectrum analyzer, which had a resolution of down to 0.02 nm. A beam profiler consisting of a high resolution camera and a translation stage was also accessible for M^2 measurements.

5.2 Spectrum and Temperature

Pumping the microchip laser at varying repetition frequency heats up the gain medium to different temperatures. The gain mediums emission spectrum shifts to longer wavelengths with increased temperature. Figure 5.2 shows the laser emission spectrum for different repetition frequencies. The shift towards longer wavelengths with increasing temperature can be seen clearly. Besides the main modes of the laser pulses, weaker side-modes are also excited. This is the result of the multi-longitudinal mode lasing that also appeared in the simulations (see chapter 4.4). For a confirmation for each single effect like mode-hopping and L-mode satellite pulse effect, the temporal profile should also be investigated, which will be done later. What can be retrieved from the spectrum immediately is the length of the microchip laser. The average mode spacing of the spectrum at 2 kHz PRF is 13.77 GHz which translates into a cavity length of 6.00 mm.

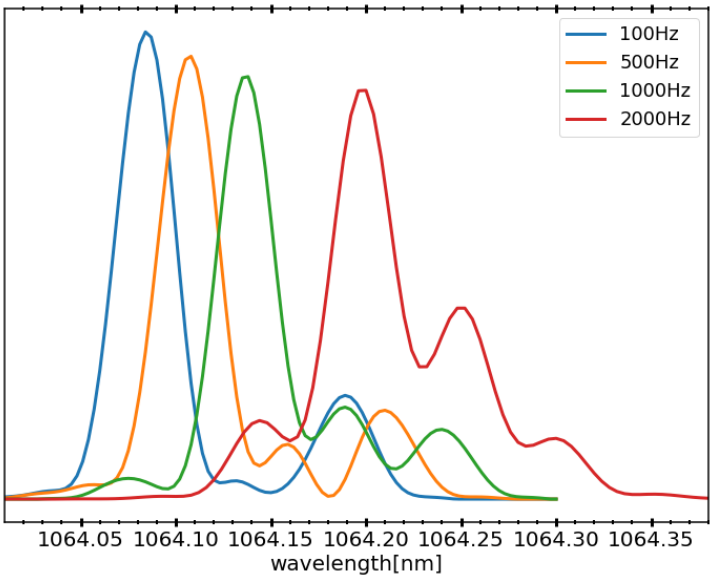

Figure 5.2: *Spectra of the laser pulses from the example microchip laser (MC01) for different repetition frequencies.*

In chapter 4.2 a model was derived to calculate the emission cross section spectrum of Nd:YAG according to its temperature. This model can be used in combination with the pump and absorption parameters to calculate the emission peak for varying PRFs. In figure 5.3 the weighted center wavelength of the measured laser mode spectra is plotted together with the modeled peak of the emission spectrum for varying PRFs. A deviation between the measured and the modeled emission spectra can be seen for increased PRFs. The model used includes the

analytic solution for the temperature profile of a pumped laser crystal given by Innocenzi (chapter 2.3).

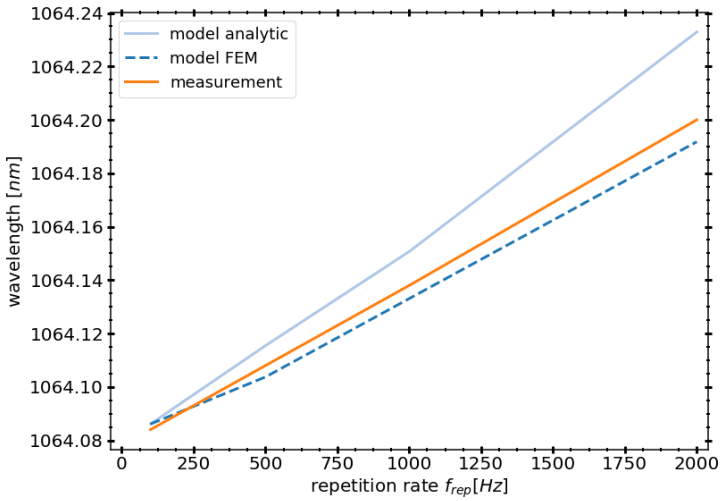

Figure 5.3: *Wavelength of peak emission cross section for different repetition frequencies. Shown are the results of an analytic model given by Innocenzi [45] and of a FEM based model in comparison with the measured spectra shown in figure 5.2.*

The microchip laser used (MC01) has an undoped end-cap bonded onto the gain medium. This end-cap enables a heat flow from the hot center of the crystal along the optical axis. To model the heat flow along the optical axis, the used model from Innocenzi can be replaced by a numerical approach, a finite element method (FEM) that includes both radial and axial heat flow. For this purpose the FEM Python package FiPy [82] was used.

In figure 5.4 the modeled temperature profiles of both the analytic and the numeric analysis are shown. Due to the extra heat flow along the optical axes, the maximum heat temperature at the center of the front-end of the gain medium ($(r, z) = (0, 0)$) is considerably reduced from 81 °C down to 52 °C. The weighted averaged temperatures within the laser modes are shown in table 5.1. It can be seen that the end-cap on the gain medium reduces the temperature considerably. The resulting focal lengths on the other hand do not change from radial to 3D heat flow. A possible explanation is that the heat can only be conducted out of the crystal by the side surfaces. The heat flow along the optical axes does not change the total radial heat flow thus the total OPD does not change. With the analytic radial-only model delivering the same focal lengths as the numeric 3D model, the calculated focal lengths within the previous chapters are still valid.

With the FEM method, the central peak emission cross sections of the proposed microchip laser at varying PRFs can be re-calculated. The FEM model

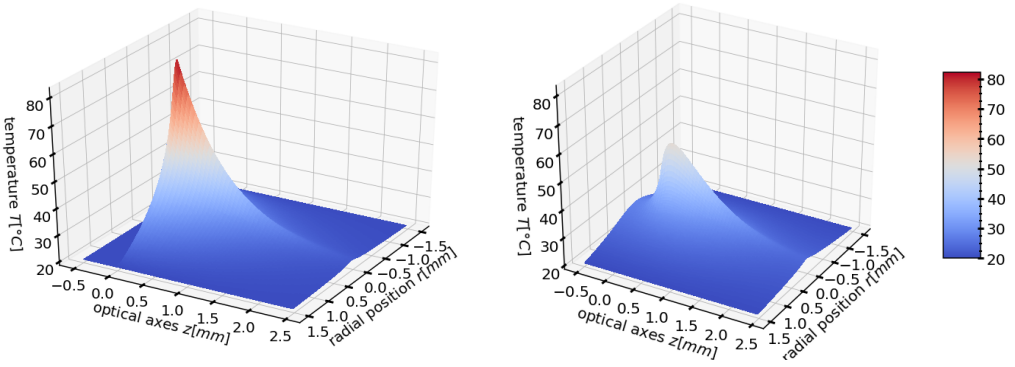

(a) *radial only heat flow* **(b)** *heat flow in all directions*

Figure 5.4: *Temperature profiles within the gain medium of the microchip laser MC01 modeled numerically with (a) radial only heat flow and with (b) a heat flow in all directions. Pump parameter were used for 2 kHz repetition frequency.*

	repetition frequency			
method	100Hz	500Hz	1000Hz	2000Hz
analytic	21.6 (2371)	27.8 (456)	35.7 (219)	51.6 (105)
FEM radial	21.5 (2378)	27.7 (452)	35.4 (217)	51.1 (103)
FEM 3D	21.1 (2378)	25.6 (452)	31.2 (217)	42.7 (103)

Table 5.1: *Averaged weighted temperature $T_{avg}[\,°C]$ (and focal lengths $f_{gain}[mm]$ in brackets) of the example microchip laser MC01 in case of three different models. Analytic solutions according to Innocenzi (analytic), temperature profiles calculated numerically including radial heat flow (FEM radial), temperature profiles calculated numerically including 3D heat flow and end-cap (FEM 3D). Focal lengths are corrected according to Strehl-ratio.*

seen in figure 5.3 shows considerable less deviation from the measurement then the analytic radial-only model. With the new model the shift in emission wavelength can be calculated accurately.

5.3 Pulse Energies and Lengths

The theory of Q-switched microchip lasers predicts varying pulse energies for varying PRFs. With the peak emission cross section becoming lower with increased temperature and PRF, the stored energy before the lasing threshold is reached is higher. Hence, the pulse energy should increase with increased PRF. On the other hand, the thermal lensing increases with PRF, which narrows the transversal mode size and lowers the pulse energy. Ultimately the increase in thermal lensing is the predominant effect, which was shown in the chapter 2.4.3. Many more effects have been combined within this work into a complex model for Q-switched microchip lasers. The variety of effects can be split into two main sub-models, that have to be used in combination to model the pulse energy and the pulse duration. For one there are rate equations to be solved to get the time dependent photon density within and outside the cavity (1). And with a second sub-model (2), the beam width inside the cavity is determined.

(1) The first sub-model consists of a set of differential equations for Q-switched lasers. The rate equations from chapter 2.4.2 including the excited state absorption of the saturable absorber are used as a starting point. They are further extended by:

- lifetime of the lower laser level of the gain material (section 4.1)
- temperature dependent emission cross section spectrum of the gain media (section 4.2) including FEM modeling of the temperature distribution inside the gain medium
- modulated photon field with spatially resolved population densities (section 4.3)
- several modulated photon fields for each possible longitudinal mode in order to include satellite pulses (section 4.4) and mode-beating (section 4.6)
- continued solving for several pumping cycles to include mode-hopping effects (section 4.5)

(2) With the second sub-model the calculation of the beam width within the cavity is possible. The included steps are:

- calculation of the thermal lens inside the gain medium, taking into account the pump beam profile and the Strehl-ratio (section 2.3)
- calculation of the second thermal lens inside the saturable absorber, taking into account the excited state absorption (section 2.4.3)

- calculation of the fundamental transversal mode within a stable cavity, taking into account the beam width widening by increased M^2 due to wavefront distortions

The beam quality factor M^2 can be determined experimentally with a beam profiler, which was done for the example microchip laser (MC01) at varying PRFs (see figure 5.5) The M^2 factor starts close to the ideal value of one, which shows that it operates at the fundamental transversal mode. With increased PRF the wavefront distortion and thus the beam quality factor M^2 of the laser beam increase. This is due to the thermal lens being non-parabolic, which was shown in chapter 2.3. Ultimately, an increase in wavefront distortion leads to an increase in the beam width in the focus and thus inside the cavity.

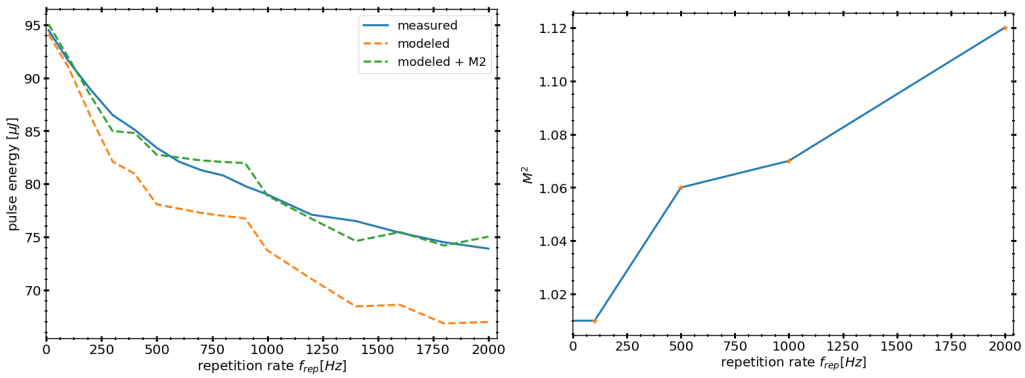

(a) *(a) pulse energies*

(b) *(b) beam quality factor*

Figure 5.5: *Measured and modeled pulse energy for the proposed microchip laser (MC01). The beam quality factor M^2 was retrieved experimentally and included into the model.*

Figure 5.5 shows both the measured and the modeled pulse energies for the example microchip laser (MC01) over varying PRFs. The used pulse energy meter is fast enough to handle pulse repetition rates of up to 25 kHz, but it is not fast enough do differentiate between main and satellite pulses. Hence, the shown simulated pulse energies contain both the main and the satellite pulses. At the lowest measured PRF of 10 Hz the induced thermal lens is very small which would normally result in an increase in mode diameter. But due to the curved end-faces of the microchip laser the pulse energy is limited to 95 µJ.

The modeled pulse energies overlap well with the measured pulse energies. An interesting feature of the change in energy over the PRF can be seen best at the simulations. The energy exhibits several plateaus after which a steep drop in energy occurs until the next plateau is reached. With the emission cross section of

the gain material being temperature dependent but the wavelengths of the longitudinal modes being fixed, the experienced cross sections shrinks under the shifted emission spectra. The plateau can thus be explained by the drop in cross section compensating the thermal lensing effect. When the temperature shift becomes big enough, the lasing longitudinal mode hops to a neighboring mode which then experiences a raising emission cross section. This effect can also be seen in the measured pulse energies where it is less pronounced than in the simulations.

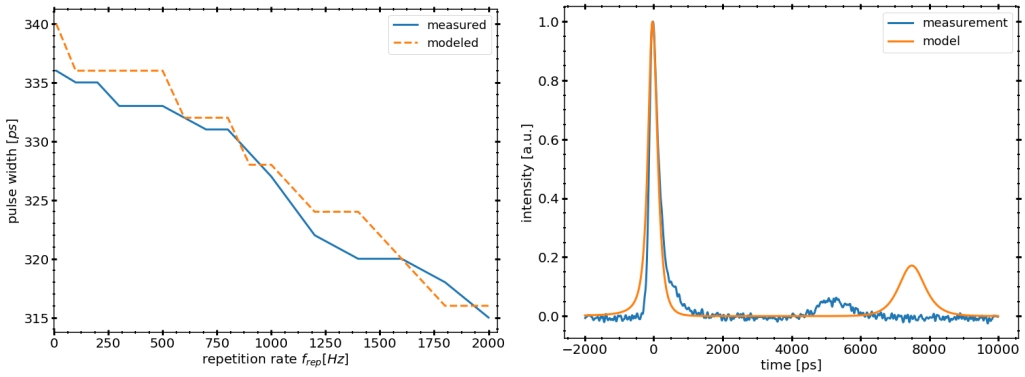

(a) *(a) pulse duration* **(b)** *(b) temporal pulse shape*

Figure 5.6: *Comparison of modeled and measured pulse durations of the example microchip laser (MC01). Also shown is a temporal profile of one pulse plus L-mode satellite pulse measured and modeled at 100 Hz PRF.*

The pulse durations of the main pulses are also modeled and measured for varying PRFs. Figure 5.6 shows that they overlap very well. The mentioned plateau-effect can also be found here in the measured pulse durations. The big steps in the simulated data on the other hand are mostly due to the low temporal resolution of 4 ps in the used time-grid. Figure 5.6 also shows the temporal profile of the main pulse plus L-mode satellite pulse at 100 Hz PRF. The modeled and the measured profiles are in good agreement. The pulse form of the main pulse deviates slightly between the measurement and the simulation, which is most likely an effect of the used measurement device (photo-diode, SMA-cable, oscilloscope). The L-mode satellite pulse was predicted in the simulations to be between 8 and 0 ns depending on the temperature settings of the microchip crystal holder. The measured pulse delay of 5.2 ns is within this range.

That the measured trailing pulse from figure 5.6 is indeed an L-mode satellite pulse and not a pulse due to the non-zero lower level lifetime of Nd:YAG can be confirmed by looking at the pulse spectrum (see figure 5.2 in the previous section). The spectrum at 100 Hz PRF shows two distinct L-modes separated by two times the microchips L-mode spacing.

5.4 Pulse Instabilities

In the simulation chapter 4 several predictions have been made on when multi L-mode lasing occurs and how it effects the output of the proposed microchip laser. Each measured spectra shown in figure 5.2 shows at least one side mode. This indicates the presence of L-mode satellite pulses, which can be found in the taken time-resolved measurements starting from the lowest measured PRF of 10 Hz up to the highest at 2 kHz.

Figure 5.7 shows the spectra of the output pulses in more detail. In case of the spectra at 100 Hz operation, one main mode (①) exists plus two smaller side modes (② and ③). The side modes correspond to the L-mode satellite pulses generated due to the spatially modulated electric field of the laser modes. Interestingly there are more than one possible side modes, which was not predicted by the simulations. The reason for this is that in the simulations an evenly distributed inversion was assumed whereas in the experiment the main inversion is generated in the beginning of the gain medium due to the high absorption of the pump beam. In chapter 2.2, it was explained that direct neighboring longitudinal modes are out of phase in the cavity center, where in this case less inversion is available then at a third cavity length, where the next neighboring modes are out of phase. Hence, the next neighboring side mode ③ is favored and has a higher amplitude in the recorded spectrum.

In the case of the increased PRF of 400 Hz, the mode spectrum shifts towards longer wavelengths due to the extra heat deposited in the crystal (see figure 5.7). The intensity distribution between the single modes 1 to 3 also change with the second mode being more pronounced. The extra energy in the second mode is a hint on mode hopping between consecutive pulses, where occasionally mode 2 would act as the main mode. This is expected to happen according to the simulations.

A fast energy meter was used to measure the pulse energies. Each of the measured pulse energies included both the main pulse and the L-mode satellite pulse (if there was any) summed together. The energy distribution is shown in figure 5.8. In case of the low PRF of 100 Hz, the pulse energies are Gaussian-like distributed. When the PRF is raised to 400 Hz, three distinct energy levels each with a Gaussian-like distribution can be fitted into the data. The parameter for the fitted Gaussian functions are shown in table 5.2. The spectra indicate mode hopping. The mode-hopping effect can explain two of the three energy levels. The remaining one can be explained by mode-beating, which should also occur according to the simulations. In order to differentiate which energy level belongs to mode beating and which to mode hopping, the temporal profiles of the output pulses are studied statistically.

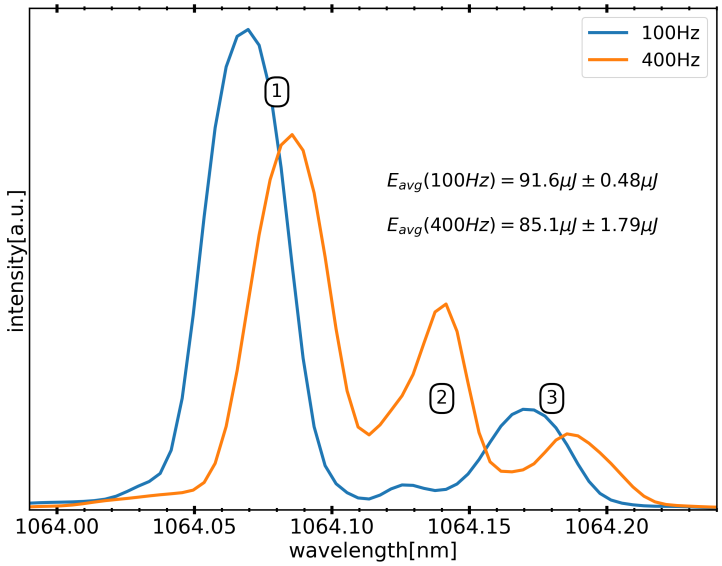

Figure 5.7: *Spectra for the output pulses of the example microchip laser (MC01) operated at 100 Hz and at 400 Hz. At both repetition frequencies the spectra feature three distinct modes marked with numbers 1 to 3. Average pulse energies E_{avg} and their standard deviation are given also.*

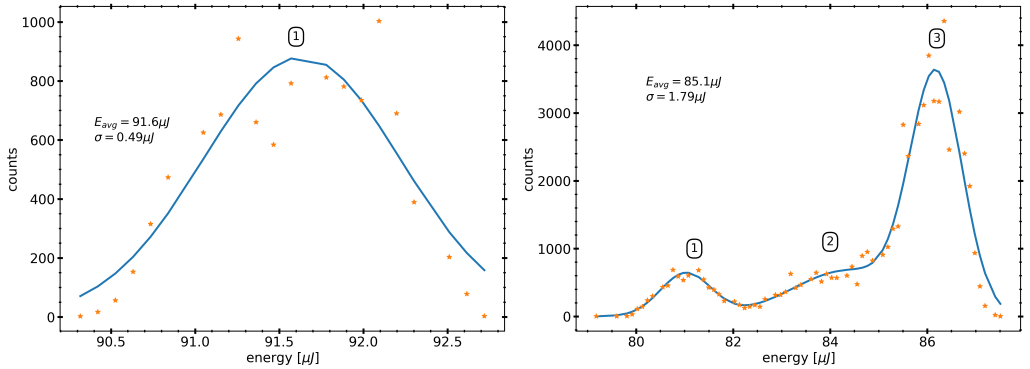

(a) *Pulse energy distribution at* $100Hz$ *PRF.*

(b) *Pulse energy distribution at* $400Hz$ *PRF.*

Figure 5.8: *Pulse energy distribution for both stable operation at 100 Hz (10,000 pulses total) and fluctuating laser output at 400 Hz (60,000 pulses total). Averaged pulse energy E_{avg} and standard deviation σ are given. Gaussian functions fit to data and plotted as continuous lines. Fit parameter for the single Gaussian function for low repetition frequency operation (marked with number 1) and the three overlapped Gaussian functions for high repetition frequency operation (marked with numbers 1 to 3) are given in table 5.2.*

rep. rate	level	E[µJ]	σ[µJ]	rel. counts
100Hz	①	91.6	0.59	1.00
400Hz	①	81.0	0.53	0.12
	②	84.4	1.15	0.26
	③	86.2	0.54	0.62

Table 5.2: *Parameter for Gaussian functions fitted to measured pulse energies at low and high PRFs. The distribution of the measured pulse energies can be found in figure 5.8.*

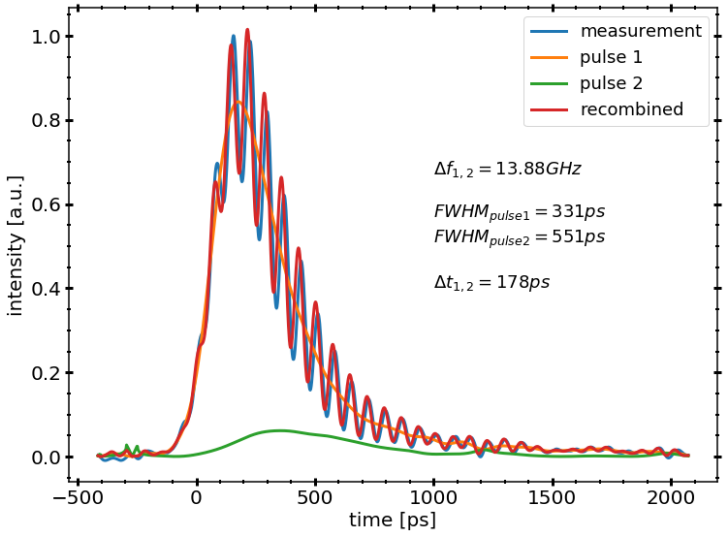

Figure 5.9: *One temporal pulse shape of the example microchip laser operated at 400 Hz PRF. A numeric Fourier-filter was applied to separate the measured pulse profile (measurement) into two distinct pulses (pulse 1 and 2). The modulation frequency $\Delta f_{1,2}$ of the measured pulse suggests an interference between direct neighboring laser modes. Shown is also the recombined pulse shape consisting of both reconstructed pulses interfering with the modulation frequency $\Delta f_{1,2}$. The recombined pulse overlaps well with the original measurement, which suggests that the separation filter delivers accurate information. Also given is the temporal distance between the two reconstructed pulse-peaks $\Delta t_{1,2}$.*

The temporal profile of 1800 laser pulses at a PRF of 400 Hz where recorded with a fast photo-diode attached to a sampling oscilloscope with a combined resolution of 15 GHz (3 dB dampening). The time window for each profile was big enough to capture both main and trailing pulses within each measurement. Most of the recorded temporal pulse profiles consisted of a main pulse with an L-mode satellite pulse, and modulated pulses where also recorded. Figure 5.9 shows one of the modulated pulse shapes with a modulation frequency $\Delta f_{1,2}$ of 13.88 GHz.

The modulation frequency coincides with the longitudinal mode spacing retrieved from the spectra (see section 5.2), which suggests that mode-beating of two direct neighboring modes is present. Two single longitudinal mode pulses can be reconstructed from the modulated pulse (pulse 1 and 2 in figure 5.9). The first pulse has the expected pulse duration of 331 ps, whereas the second temporally overlapping pulse with a longer pulse duration of 551 ps seems to be a mixed Q-switched gain-switched pulse. The recording window of the shown modulated pulse was extended to 10's of nanoseconds and no trailing pulse could be seen. The measurements of the temporal pulse profiles confirmed the occurrence of mode-beating, which could explain a third energy level within the energy distribution.

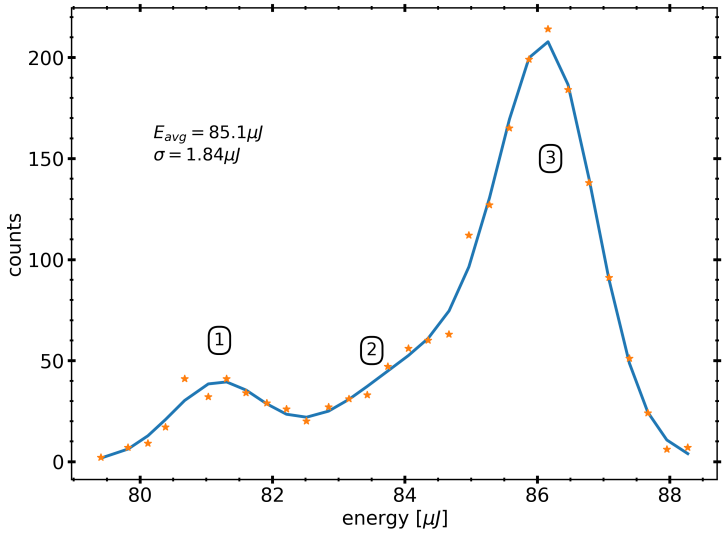

Figure 5.10: *Distribution of the total pulse energies retrieved by temporal pulse profiles at 400 Hz PRF. Pulse profiles were taken with fast diode and sampling oscilloscope. Single temporal profiles are integrated over time to include both main and satellite pulse. Integration values are scaled to match the average pulse energy of 85.1 µJ.*

To see if the three-fold energy distribution can be reproduced by the recorded temporal pulse profiles, the amplitudes of each profile were summed up to a total detector count value per measurement and then combined to a detector count distribution over the recorded 1800 pulses. The total count values where multiplied by a constant factor to match the average pulse energy of 85.1 µJ. In figure 5.10 the energy distribution of the temporal pulse profiles are plotted. The distribution is very similar to the one retrieved with the energy meter. Three Gaussian like distributed pulse energy levels can be identified again. Their positions are very close to the ones retrieved by the energy meter (see table 5.3). The main differences between the two measurements are the widths of the three energy levels. They are higher in the case of the fast photo-diode, which can be explained by the rather

high noise level of the oscilloscope plus photo detector.

level	E[µJ]	σ[µJ]	rel. counts
①	81.2	0.71	0.12
②	84.7	1.36	0.33
③	86.2	0.71	0.55

Table 5.3: *Parameter of Gauss functions fitted to energy distribution from figure 5.10.*

Knowing that the energy distribution can be reproduced by the temporal measurements, the occurrence of mode beating can now be correlated with the single pulse energies. A fitting routine in Fourier space was applied to the temporal pulse profiles to identify mode beating. That method gives a modulation amplitude for each measured profile. The correlation between these amplitudes along the corresponding pulse energies are shown in figure 5.11. Mode beating shows up predominately at the middle energy level ②, whereas the other two levels ① and ③ have low to no mode-beating. From the simulations and the measured spectrum it was deduced before that the proposed microchip laser is supposed to mode-hop and that the pulse energies should be distributed around two distinct energy levels, one for each longitudinal mode. The measured energy spectrum shows a third energy level ② which can now interpreted as pulses with mode-beating.

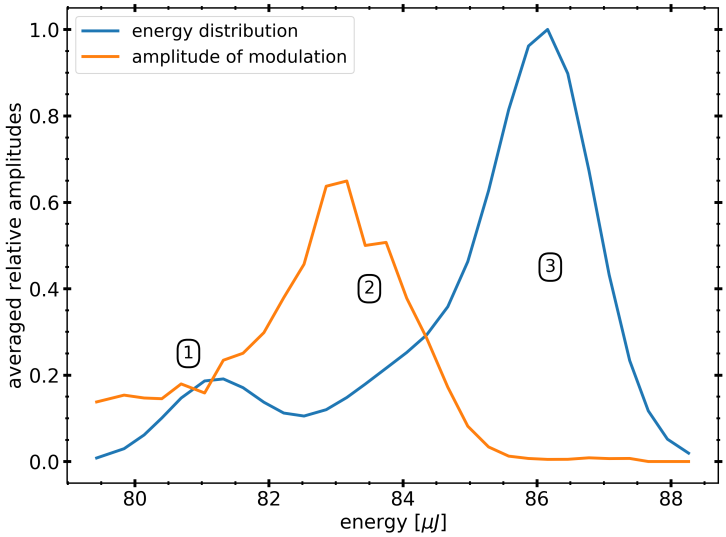

Figure 5.11: *Distribution of the retrieved pulse energies from temporal pulse profiles at 400 Hz PRF (energy distribution). Single energy values have been scaled by a constant factor to match the distribution to an average pulse energy of 85.1 µJ. Amplitudes of the pulse-modulations where taken from Fourier-space and binned together along the energy distribution (amplitude of modulation). The three numbers (1 to 3) mark the three different pulse types: (1) low pulse energy with low modulation depth, (2) medium pulse energy with high modulation depth, (3) high pulse energy with no modulation.*

5.5 Discussion

A passively Q-switched microchip laser (MC01) is implemented (section 5.1) according to the proposed design (table 3.2) to act as an oscillator for the NextGen-PIRL. The basis for the implemented microchip laser is a design published by Zayhowski (HPMCL-3 found in [63]). Starting from the HPMCL-3, the design is optimized towards short pulse durations around 300 ps and high pulse energies around 100 µJ without reaching the damage threshold of the used materials. The pulse energies and pulse durations were measured over a wide range of PRFs from 10 Hz to 2 kHz (section 5.3) and compared to the predictions from the simulations shown in the previous chapter 4. The measured pulse characteristics are in good agreement with the simulations.

The simulations shown in the previous chapter 4 predict a multi-longitudinal mode behavior. This was confirmed experimentally by several measurements. The measured spectrum of the output pulses show two or more mode operation starting at around 400 Hz (section 5.2) which is in good agreement with the simulations. Confirmed by measured spectra and the temporal pulse shapes are the L-mode satellite pulses. The spatially modulated extraction of the inversion in the gain

medium by the first single-mode laser pulse and the less modulated bleaching in the saturable absorber lead to the generation of a second partially gain-switched laser pulse running in a different longitudinal mode. The experiments showed that the L-mode satellite pulse effect is indeed independent of the PRF and it cannot be suppressed by lowering the PRF.

In section 5.4, it was shown that different multi-mode effects, like mode-hopping between single pulses and mode-beating within a single output pulse, can be differentiated by their different pulse-energy spectra. Two-mode-hopping results in a two folded pulse energy distribution, whereas with the occurrence of mode-beating a three folded distribution emerges. This insight will be of advantage for microchip designs where the mode-beating occurs in a frequency range above the measurable bandwidth of fast oscilloscopes.

Pulse instabilities are a substantial concern for Q-switched microchip lasers. Pulse energy bifurcation was already reported by Zayhowski [83] in case of the HPMCL-03 laser, but it was not investigated further. Indeed, the reported pulse lengths and pulse energies of that microchip designs (shown in table 3.1) were taken at a PRF of only 500 Hz. Zayhowski only stated that at raised PRFs, pulse energy fluctuations appeared, but no further details or explanations were given.

Pulse instabilities are an issue when it comes to the NextGenPIRL. The pulses have to be further amplified before they can be used as pump pulses for the OPA. Both the amplifier and the OPA are typically operated close to the damage threshold of their coatings. Mode-beating drastically increases the maximum field strength which would result in certain optical damage. The next aspect is that the nonlinear amplification process within the OPA increases instabilities even more, which is not advantageous for any experiment attached to the laser system. For a several stage system like the NextGenPIRL a seed laser as stable as possible is needed. The proposed microchip laser (MC01) shows most convincingly how important stability optimized designs are, when in comes to Q-switched microchip lasers.

Chapter 6

Stability Enhanced Microchip Designs

The characterization of the output pulses of the MC01 laser showed strong pulse instabilities due to mode-hopping and mode-beating starting at a PRF of only 400 Hz. For the NextGenPIRL a stable operation up to several kHz PRF is needed, if a high average output power should be reached. There are several ways to suppress multi longitudinal mode lasing and to enhance the stability in Q-switched microchip lasers.

(1) First, a shortening of the cavity results in a larger spectral mode spacing. As can be seen in a figure 4.14 in section 4.6, only a certain amount of longitudinal modes fit under the roof of the emission cross section spectrum of Nd:YAG. The spacing between the single modes is defined by the length of the cavity. When it is shortened, the spectral distance between the single modes increases and thus the difference in cross sections between neighboring modes increases as well. Ideally the neighboring modes to the main mode feature a low enough emission cross section, so that they never reach threshold.

(2) Another method to suppress multi-L-mode lasing is by temperature tuning. The main mode can be placed most precisely at the point of maximum emission cross section, so that for the neighboring modes the difference in emission cross section is maximized. This method is essential for any microchip design, as at certain temperature points the two center modes do have the same emission cross sections. This can result in mode-beating, which is shown in section 4.5.

(3) Cooling the gain medium narrows the emission spectrum and thus increases the drop in cross section from the center mode to its neighbors (section 4.2).

(4) The modulation of the photon field for next neighboring modes gets out of phase when approaching the cavity center. Designing the lengths of the individual components (gain medium, absorber, end-caps) in a way that half of the cavity length or even two third are within the volume of the saturable absorber suppresses the onset of neighboring modes. This effect also plays a role within the proposed microchip laser (MC01), where L-mode satellite pulses run in next-neighboring modes (see figure 5.2).

6.1 Shortened Cavity

With these possibilities in mind, a new microchip design MC02 is implemented (table 6.1). Starting from the proposed microchip design (MC01) the length is gradually reduced by shortening or even removing single individual crystals. As most of the heat is generated within the gain medium and not within the absorber, the end-cap of the absorber is left out. The end-cap of the gain medium on the other side stays the same (0.5 mm). The length of the gain medium is reduced down to 1.5 mm, which is possible due to the high absorption of the pump beam from the VBG stabilized pump diode. By raising the initial transmission of the saturable absorber from 20 to 30%, it is possible to reduce its length to 1.9 mm.

	end-cap $l[mm]$	gain $l[mm]$	SA $l[mm]$	end-cap of SA $l[mm]$	optical length $l[mm]$	initial trans. $T_0[\%]$	output coupler $R_{oc}[\%]$
MC01	0.5	2.5	2.5	0.5	10.9	20	30
MC02	0.5	1.5	1.9	0.0	7.1	30	30
MC03	0.2	0.8	1.6	0.0	4.7	30	50

Table 6.1: *Design parameters for Q-switched Microchip lasers used within this work (MC01 to MC03).*

The resulting design has several advantages regarding its stability. The reduced length results in a wider mode spacing (point 1). Increase of the initial transmission lowers the needed pump pulse energy to reach the initial population inversion, thus the gain medium is heated up less (point 3). The crystal is temperature controlled (point 2). Furthermore, the crystal is housed inside a dry nitrogen purged box with a pump entrance window and a laser pulse exit window. With the dry air and a strong Peltier element, it is possible to cool the crystal down to -30 °C during operation (point 3).

As a first test, the new microchip laser is operated at room temperature (20 °C). The spectrum at 1 kHz PRF shows a single main mode plus one satellite L-mode (figure 6.1). The laser stays in single plus satellite mode operation till 3 kHz and then switches to three mode lasing. The maximum achievable PRF is 3.5 kHz after which no lasing is possible due to excessive heating of the gain medium. The mode-spacing retrieved from the spectrum at 3.5 kHz is 21.17 GHz, which translates into a cavity length of 3.9 mm physical or 7.1 mm optical.

Like in case of the proposed microchip laser (MC01), the multi-L-mode operation can produce both mode-hopping and mode-beating. For the new microchip laser (MC02) the mode spacing is above the resolution of the available oscillo-

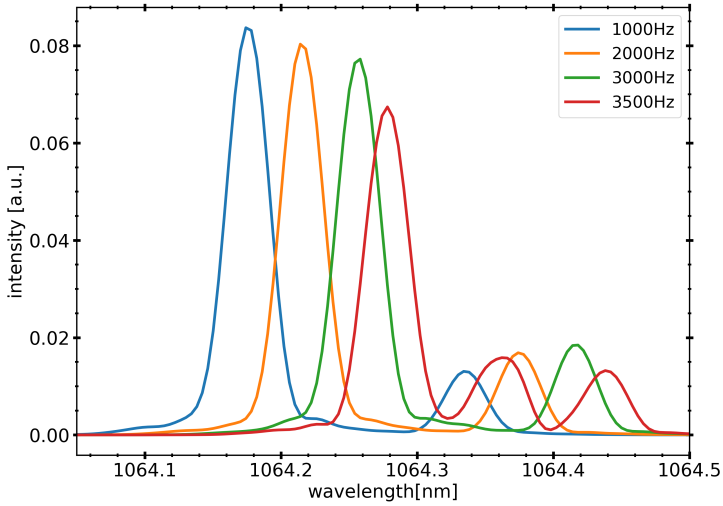

Figure 6.1: *Spectra of the laser pulses from the microchip laser MC02 at different repetition frequencies.*

scope, thus another method to check for mode-beating has to be used. In the section before it was shown that both mode-beating and mode-hopping changes the energy distribution of the output pulses. The measured pulse energies for the MC02 laser operated at 3 kHz shows a single Gaussian distribution (figure 6.2), which is expected as only one main mode plus one satellite mode is present. At a raised PRF of 3.5 kHz the pulse energy distribution (figure 6.2) looks very similar to the one of the MC01 laser at 400 Hz (figure 5.8). The new distribution can also be fitted by three separated Gaussian distributions (table 6.2). It can be deduced that mode-beating and mode-hopping occur for the MC02 laser at running at 3.5 kHz.

rep. rate	level	E[µJ]	σ[µJ]	rel. counts
3000Hz	①	35.1	0.19	1.00
3500Hz	①	33.5	0.23	0.13
	②	34.5	0.41	0.13
	③	35.1	0.26	0.73

Table 6.2: *Parameters for Gaussian functions fitted to measured pulse energies at two PRFs. The distribution of the measured pulse energies can be found in figure 6.2.*

The raise in PRF for stable operation from some 100 Hz with the microchip laser MC01 to 3 kHz with the MC02 laser is quite an improvement. In order to push the border of stable operation further, the active cooling with the Peltier

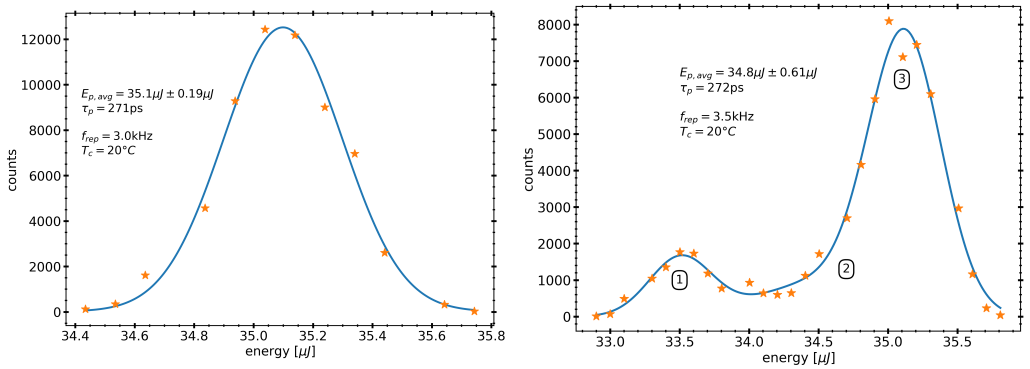

(a) $f_{pulse} = 3000Hz$ **(b)** $f_{pulse} = 3500Hz$

Figure 6.2: *Pulse energy distribution of the microchip laser MC02 for two PRFs. Averaged pulse energies E_{avg} are given width their corresponding standard deviation. Gaussian functions fit to data and plotted as continuous lines. Fit parameter for the single Gaussian function for 3 kHz operation and the three overlapped Gaussian functions for 3.5 kHz operation (marked with numbers 1 to 3) are given in table 6.2.*

element is used to cool the crystal holder down to -19 °C. At this temperature stable single mode (plus satellite mode) operation was achieved with a PRF of 5 kHz (figure 6.3). The energy distribution is a single Gaussian with a standard deviation of below 1%.

The cooling of the crystal not just narrows the emission cross section spectrum of the gain medium, but it also raises its peak value. And the raised PRF increases the thermal lensing. As a direct result, the pulse energy drops from 35.1 µJ at 3 kHz uncooled operation down to 21.9 µJ at 5 kHz cooled operation. Further increase in PRF led to multi-L-mode lasing.

Even though there is a big improvement in stability when switching from the proposed design to the new one, there is still room for improvement. The quasi single L-mode operation at 5 kHz still produces L-mode satellite pulses. When this laser would be used as a seed laser for an amplifier, these satellite pulses would be amplified too.

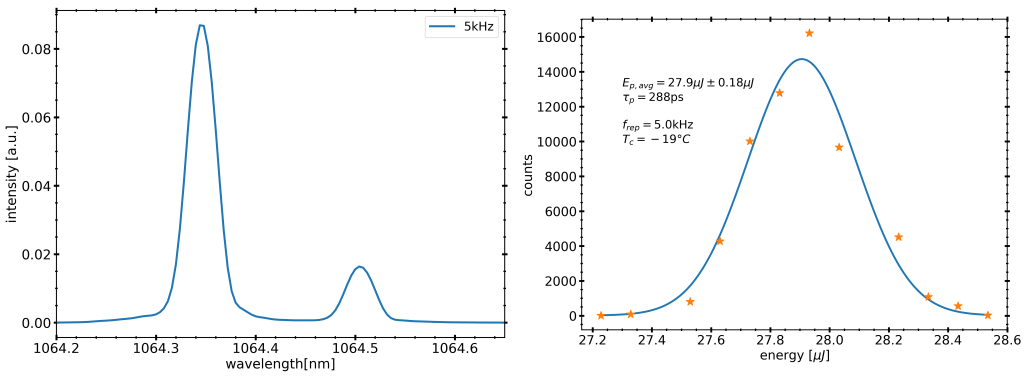

(a) *spectrum* **(b)** *energy distribution*

Figure 6.3: *Measured spectrum and pulse energy distribution of the microchip laser MC02 operated at 5 kHz PRF and -19 °C crystal holder temperature. Given are the average pulse energy $E_{p,avg}$ with its standard deviation and the pulse duration τ_p.*

6.2 Asymmetric Cavity

In order to get rid of the satellite pulses for good, the MC02 laser is further improved. So far, only the first three mentioned methods (point 1 to 3) for enhancing the stability have been taken advantage of. A third design MC03 (table 6.1) is implemented, which is an even shorter version of the MC02 laser (point 1) and it uses an asymmetric cavity design to further suppresses multi-L-mode lasing (point 4). The length of the gain medium plus end-cap is reduced from 2 mm to only 1 mm whereas the length of the saturable absorber is only reduced by a little from 1.9 mm down to 1.6 mm. In order to counteract the loss in absorption of the pump beam by the shortened gain medium, the doping level of Neodymium is increased from 1.1% to 1.6%.

The spectra of the MC03 laser operated at room temperature (20 °C) show true single L-mode operation at up to 2 kHz. At 3 kHz a small satellite mode starts to appear and its intensity is raised with further increase of the PRF. The very short cavity of 2.6 mm successfully suppresses next-neighboring modes, and the asymmetric crystal lengths lead to the suppression of direct-neighboring modes for PRFs of up to 2 kHz. At an operation above 4 kHz no lasing was possible due to overheating of the gain medium. A close look to the spectrum at 4 kHz reveals that two satellite L-modes exist (① and ③ in figure 6.5). The energy distribution on the other hand does not show any signs of mode-hopping or mode-beating. Hence, the satellite pulses seem to hop between the two neighboring modes. The L-mode spacing is retrieved from the spectrum to be 31.77 GHz, which translates into a cavity length of 2.6 mm physical or 4.7 mm optical.

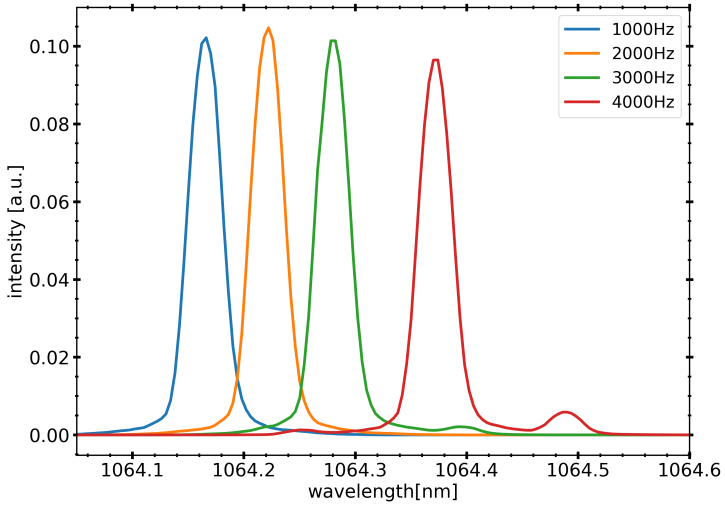

Figure 6.4: *Spectra of the laser pulses from the microchip laser MC03 for different PRFs operated at room temperature (20 °C).*

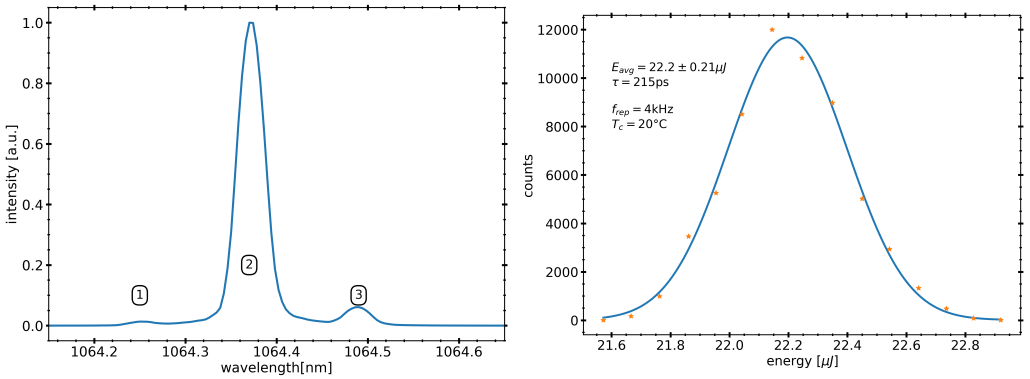

(a) *spectrum* **(b)** *energy distribution*

Figure 6.5: *Measured spectrum and pulse energy distribution of the microchip laser MC03 operated at 4 kHz repetition frequency and 20 °C crystal holder temperature. Given are the average pulse energy $E_{p,avg}$ with its standard deviation and the average pulse duration τ_p.*

The laser is pushed to its limit of stable operation by increasing the PRF while cooling the crystal. The highest pulse rate with true single mode operation was achieved at 5 kHz with the crystal holder cooled down to -15 °C. The spectra consist of a single mode with no satellites (figure 6.6). The stability of the pulse energy is remarkable with a deviation of only 0.74% from the average pulse energy. The laser was not as sensitive to temperature fluctuations as the previous one (MC02). Stable operation in true single mode was possible even when the

temperature of the crystal holder drifted by ±1 °C.

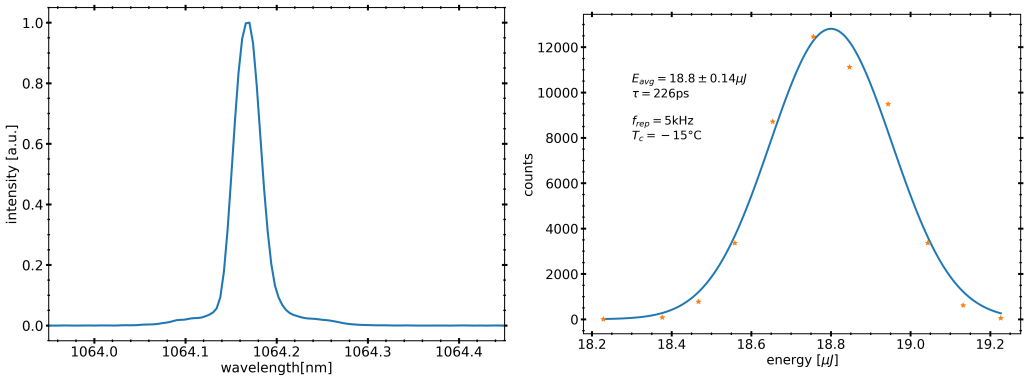

(a) *spectrum* **(b)** *energy distribution*

Figure 6.6: *Measured spectrum and pulse energy distribution of the microchip laser MC03 operated at 5 kHz PRF and at -15 °C crystal holder temperature. Given are the average pulse energy $E_{p,avg}$ with its standard deviation and the average pulse duration τ_p. The wings of the longitudinal mode are most probably artifacts from the cladding mode of the used multi-mode fiber to couple the light into the spectrometer.*

At uncooled conditions the laser was able to operate till 4 kHz at a wavelength of 1064.37 nm (main L-mode). At 5 kHz cooled operation the pulse wavelength is centered at 1064.17 nm. It can be deduced that higher pumping rates should still be possible before the gain medium overheats. The highest achievable point of operation is reached at 10 kHz PRF. The crystal has to be cooled down to -28 °C, which is close to the achievable -30 °C of the available setup. The laser pulses are single mode with one L-mode satellite pulse (figure 6.7). The energy distribution shows no signs of mode-hopping or mode-beating and the deviation from the average pulse energy is only 0.8%. The temperature of the crystal holder can vary by up to ±1 °C with the laser continuing to produce quasi single mode pulses.

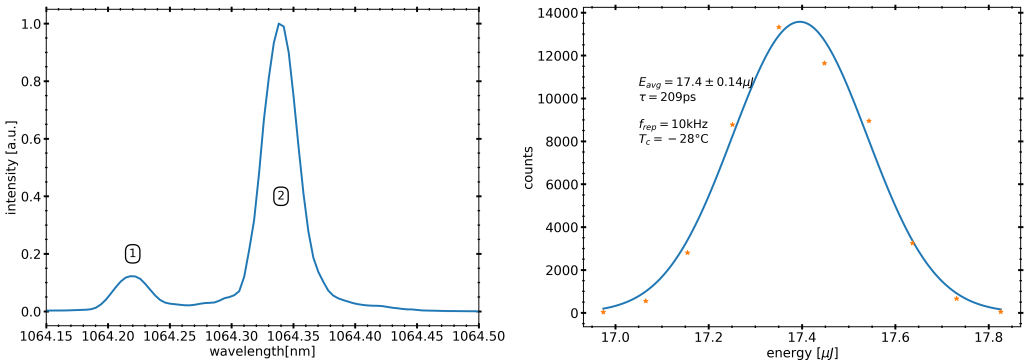

(a) *(a) spectrum* **(b)** *(b) energy distribution*

Figure 6.7: *Measured spectrum and pulse energy distribution of the microchip laser MC03 operated at 10 kHz repetition frequency and -28 °C crystal holder temperature. Given are the average pulse energy $E_{p,avg}$ with its standard deviation and the pulse duration τ_p.*

6.3 Discussion

The proposed microchip laser (MC01) produced short sub-400ps pulses with a high pulse energy of 85 µJ, but it lacks in stability. Multi-L-mode effects lead to mode-hopping and mode-beating. The design was improved for better stability by forcing the cavity to stay in single-longitudinal mode operation. Several methods to do this where identified and implemented in two additional designs (MC02 and MC03).

The length of the cavity was reduced to increase spectral mode spacing (1). The temperature was tuned in the way that one L-mode is placed at the peak of the emission cross section spectrum (2). The temperature was lowered even further to reduce the spectral width of the emission cross section (3) until the next stability point (2) is reached. The cavity design was chosen to be asymmetrical regarding the lengths of the gain and absorber medium to suppress L-mode satellite pulses (4).

With all these optimizations, the laser MC03 was able to produce single mode pulses with one L-mode satellite pulse per cycle at PRFs of up to 10 kHz. True single mode operation without any satellite modes was achieved at up to 5 kHz. The setup was not sensitive to temperature fluctuations of up to ±1 °C. The drastically reduced cavity length led to a short pulse duration of only 226 ps at 5 kHz PRF.

The stability reached with the MC03 sets a new mark for short-pulse microchip laser. Most short pulse microchip laser suffer from multi-L-mode effects ([79], [80]) or even multi transversal mode effects ([84]). Close to the stability of the

MC03 laser comes the microchip laser reported by Niu *et al.*[77]. A PRF at single mode operation without L-mode satellite pulses of up to 4.4 kHz was reached with pulse energies of 32.5 µJ. The cavity with a length of only 2 mm was even shorter than the MC03 laser, but the resulting output pulse duration was 715 ps which is above of what is needed for the NextGenPIRL. Agnesi *et al.*[85] reached short pulses with a duration of 486 ps, but the laser started mode-hopping at PRFs between 2 and 3 kHz.

Worth mentioning is the report from Dong *et al.*[86], where Yb:YAG was used as the gain medium. A big advantage of Yb:YAG is its low emission cross section in combination with high doping levels, which lead to a high energy load capacity. The generated pulses had an energy of 172 µJ with a duration of only 237 ps at 3.5 kHz PRF. The presented data from Dong *et al.*shows the onset of multi-L-mode lasing at roughly 1 kHz. At 3.5 kHz PRF the published spectrum shows 3 main L-modes, which suggests that mode hopping occurred. The lasers energy fluctuations are reported to be 6%, which is several times higher than for any of the presented microchip lasers in this work (2.1% for the MC01 laser at 400 Hz and 0.8% for the MC03 laser at 10 kHz). Even though the usage of Yb:YAG with its high pulse energy scaling capabilities seems very promising, the broad emission cross section spectrum makes it impossible to achieve stable operations within a Q-switched microchip laser in the kHz PRF range.

The remarkable stability of the MC03 laser comes with a cost. The pulse energies drop drastically from 85.1 µJ with the first design (MC01) down to 17.4 µJ with the stability optimized design (MC03). Several reasons lead to that drop in energy. The initial transmission of the saturable absorber is increased from 20 to 30% in order to shorten the cavity length, which also results in less energy being stored in the gain medium. The gain mediums length is also shortened, and a shortening of a cavity leads to a narrowed transversal mode diameter. The PRF and thus the average pumping power was increased drastically from 400 Hz up to 10 kHz, which leads to a far stronger thermal lensing and again to a smaller transversal mode diameter. The excessive heating within the gain medium and the drop in emission cross section would usually lead to an increase in pulse energy. But the excessive heating had to be compensated by cooling the crystal down to -28 °C in order to narrow the emission spectrum.

Chapter 7

Power Amplifier

The OPA stage of the PIRL has typical conversion efficiency of 10% into the Mid-IR [16, 38]. In order to reach the necessary energy in the idler of at least 100 µJ, it has to be pumped with pulses in the mJ-level. The pulse energies of the stable microchip laser MC03 are around 17 µJ, thus the gain G of the amplifier has to be 60 or more to bring the pulses to at least 1 mJ.

An interesting approach for a very simple amplifier stage is presented by Martial *et al.*[87]. A very thin, long and low doped Nd:YAG crystal was used as the gain medium. The crystal is end-pumped and the thin rod geometry provides beam guiding for the pump beam through the crystal. This long and thin crystal design enables a very low doping level of 0.2% while a pump absorption of typically 98% is reached [88]. The heat is generated within a large volume with a outer surface that is very close to the heated region. Hence, the heat can be transported out of the crystal most efficiently and pumping with up to 110 W is possible with this design [88].

One example setup from the report of Martial [87] is very close to the intended NextGenPIRL parameters. A pulsed seed with 80 mW of power at 1 kHz PRF was amplified to 2.7 W with a 60 W pump laser running in pulsed mode at 31% duty cycle. The microchip laser MC03 on the other hand produces around 80 mW at a PRF of 5 kHz. The reduced time interval between consecutive pulses to below the lifetime of the upper laser level enables continuous pumping. With a pumping power of 60 W at 100% duty cycle, three times the reported output power or a total power of 8 W or a pulse energy of 1.6 mJ can be expected from this amplifier in conjunction with the MC03 laser.

In this chapter the limitations of the crystal-fiber based amplifier are discussed, the amplifier is tested together with the MC03 laser and the output pulses are characterized. It is investigated if the amplifier can deliver the necessary output power for the NextGenPIRL. Last, a concept to scale the output power further is presented.

7.1 Damage Threshold and B-Integral

Two limitations concerning the pulse energies do exist with the proposed fiber amplifier. With the beam diameter being limited to 400 µm due to the small rod aperture of only 1 mm in diameter, the damage threshold of the coatings on the crystals end-faces are of concern. The damage threshold is specified by the manufacturer (Fibercryst, France) with 3 J/cm^2 for 1 ns pulses. Using the root-law for scaling the threshold down to 200 ps [89], the amplified pulses are limited to a peak fluence of 1.34 J/cm^2 or a pulse energy of 3.4 mJ.

The small beam diameter together with the long length of the crystal can result in nonlinear effects. A common criterion for the appearance of nonlinear effects is the B-integral [42], defined by

$$B = \frac{2\pi}{\lambda} \int n_2 I(z) dz \tag{7.1}$$

where n_2 is the second-order nonlinear refractive index and $I(z)$ is the peak intensity along the nonlinear medium. The nonlinear index of refraction for YAG is given by Köchner [43] with 6.9×10^{-16}cm^2/W. To get an estimate for the beam intensity along the amplifiers optical axis, the amplifier model by Frantz and Nodvik [90] can be used. Assuming a spatially homogeneous population inversion inside the amplifier with a small signal gain coefficient g_0 and a rectangular pulse shape, the output fluence F_{out} is given by

$$F_{\text{out}} = F_{\text{sat}} \ln\left(1 + (e^{\frac{F_{\text{in}}}{F_{\text{sat}}}} - 1) e^{g_0 l_{\text{gain}}}\right) \tag{7.2}$$

with the input fluence F_{in}, the saturation fluence F_{sat} and the length of the amplifier l_{gain}. The Frantz-Nodvik equation can also be applied on a two-pass amplifier, when the small signal gain coefficient is reduced between the passes according to the extraction efficiency η_e from the first pass.

$$g_0' = g_0(1 - \eta_e) \qquad \text{with} \qquad \eta_e = \frac{F_{\text{out}} - F_{\text{in}}}{g_0 l_{\text{gain}} F_{\text{sat}}} \tag{7.3}$$

The position dependent fluence $F(z)$ within the gain medium is needed to calculate the B-integral, and it is given by the differential equation from Avizonis and Grotbeck [91]

$$\frac{dF(z)}{dz} = F_{\text{sat}}\, g_0\, (1 - e^{-\frac{F(z)}{F_{\text{sat}}}}), \tag{7.4}$$

assuming a lossless material and square shaped pulses, like in the Franz-Nodvik equation. For $I(z)$ the peak intensity level for a Gaussian pulse is used with

$$I(z) = 4 \sqrt{\frac{\ln(2)}{\pi}}\, \frac{F(z)}{\tau_p} \tag{7.5}$$

These equations can now be used to calculate the B-integral for varying output fluencies or energies. One assumption has to be made for the correction parameter γ within the saturation fluence with $F_{sat} = \frac{h\nu}{\gamma\sigma}$, which is also called the inversion reduction factor [43]. The exact value for γ is retrieved within the section 7.4. For the present calculation it can be approximated to a value of two.

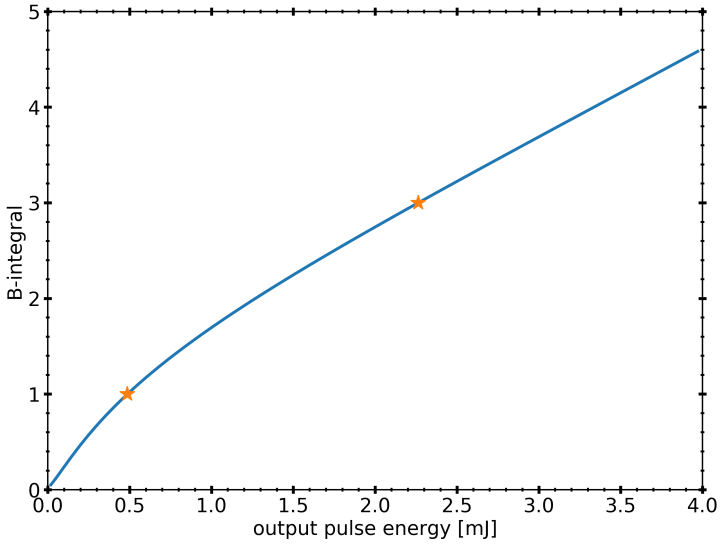

Figure 7.1: *Approximated B-integral for the amplifier system and different output pulse energies. Marked are the two points where the B-integral is one or three. Calculations are done for an input pulse energy of 17 µJ, a beam diameter of 400 µm, a pulse duration of 220 ps and a length of the amplifier of 50 mm. For $I(z)$ the peak intensity level has been used instead of a spatially or temporally averaged intensity.*

The B-integral over output pulse energies for the two-pass amplifier seeded with pulses from the MC03 laser is shown in figure 7.1. A B-integral with a value of one or less would be the safest choice where no self-phase modulation occurs. But with this kind of amplifier this value will be reached at a pulse energy of 0.49 mJ, which is too low for the NextGenPIRL. The next threshold for the B-integral is somewhere between of 3 and 5, where self-phase modulations might start to occur [42]. This limit will be reached at an output pulse energy between 2.3 mJ and 4.4 mJ.

Both the damage threshold and the B-integral do limit the achievable output pulse energy. But the limits are well above 1 mJ, and the amplifier is suited for the NextGenPIRL design.

7.2 Amplifier Setup

A two pass amplifier is set up to boost the seed pulses from the stability optimized microchip laser MC03 to the mJ-level. The amplifiers gain medium is a low doped (0.2 at.%) Nd:YAG rod with a diameter of 1 mm and a length of 50 mm (figure 7.2). It can be pumped from one or both sides by fiber coupled diode lasers (P1 and P2), each with up to 40 W of power. The beam from pump P1 is coupled into the setup by a fiber with a 200 µm core diameter. It is collimated by a 50 mm lens and focused slightly inside the gain crystal with a 100 mm lens. The fiber coupling from pump P2 has a core diameter of 400 µm, it is collimated by a 50 mm lens and focused with a 75 mm. The seed pulses from the microchip laser are collimated and focused inside the amplifier crystal. The focal spot diameter inside the crystal is measured to be 400 µm ($1/e^2$) and 420 µm at the crystals end-faces. After the first pass, the diverging beam is refocused inside the crystal rod with a spherical mirror (SM). The signal after the second pass is separated from the seed with the use of a quarter waveplate (WP) and a thin-film polarizer (TFP). An optical isolator is used to prevent feedback from the amplified pulses back to the microchip laser. The temperatures of the pump diodes and of the amplifier crystal are tunable by Peltier elements.

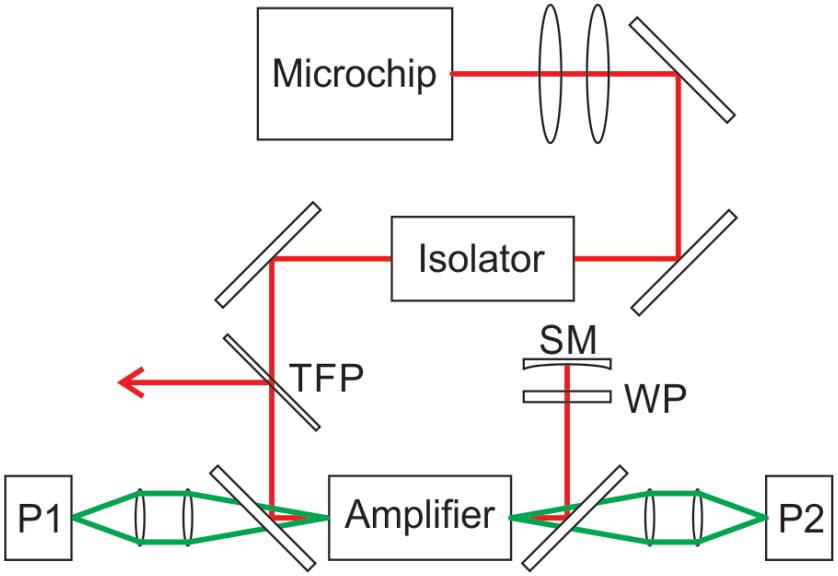

Figure 7.2: *Setup of the two-pass power amplifier. Seed pulses from the microchip laser are collimated and focused into the amplifier, then reflected back by a spherical mirror (SM). Separation of seed and signal are done with a quarter waveplate (WP) and a thin-film polarizer (TFP). An optical isolator prevents feedback. The amplifier can be pumped with up to two pumping modules (P1 and P2).*

7.3 Amplifier Experiments

As a first experiment, the amplifier is operated at single pass with the maximum seed pulse energy of 13.9 µJ. The pulse energy after the amplifier is measured to be 13.6 µJ, which gives a transmission of 98% through the crystal. The two percent losses are due to reflections on the entrance and exit surfaces of the gain medium and due to absorption within. The output pulse energy over raised pumping power is shown in figure 7.3, one time with only one pump diode active (P1) and the other time with both diodes active (P1 and P2). The two diodes seem to have different resulting gain values at the same pumping power. The reason is that both diodes have slightly different wavelengths, but they are both temperature controlled by only one cooling plate. That wavelength mismatch leads to different pumping rates and gain values. The gain of the module does not show any signs of roll-over at high pumping rates. Previous reports show that with this kind of amplifier a roll-over can be expected earliest for pumping powers between 80 W and 100 W [88].

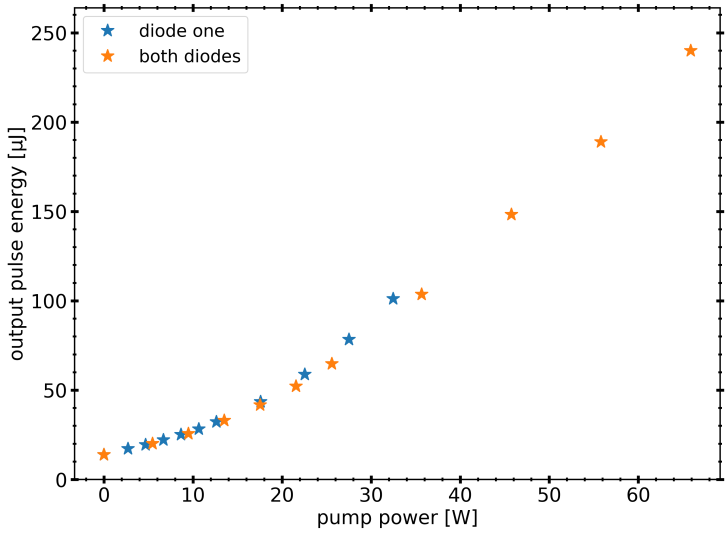

Figure 7.3: *Single pass amplification seeded by the MC03 laser. Output pulse energy is plotted over pumping power, one time with only one pump diode active (diode P1) and the other time with both diodes (P1 and P2).*

A roll-over of an amplifier can have several reasons. In general, the output fluence of an amplifier should first raise exponentially with the pumping power as long as the resulting output fluence is well below the saturation fluence. Then if the two fluences get close to one another, the exponential raise gradually changes to a linear slope. The change between exponential to linear raise in output fluence

is due to a saturation effect, that is described by the Franz-Nodvik model. Basically, the first half of the laser pulse diminishes the population density n within the amplifier, so that the second half of the pulse experiences a lower gain coefficient $g = n\sigma$. A roll-over is, when other effects lead to a further diminish in gain. These effects can be:

- With increased pumping power, the gain medium heats up and the emission cross section becomes smaller. In the case of the presented amplifier, this was taken care of in the sense that the amplifier was mounted on a temperature controlled heat sink, and the temperature was always optimized for maximum gain.
- With increased pumping power, the population inversion can raise to levels, where multi-ion processes like up-conversion start to happen. This leads to a reduction in inversion and thus gain. The presented amplifier is specifically designed with a very low doping level of only 0.2 at.%, so that this effect is strongly suppressed.
- With increased pumping power, the thermal lens becomes stronger and the laser beam converges within the gain crystal. The reduced beam diameter further increases the fluence of the laser pulse towards the exit of the amplifier and the saturation effect is pronounced. The increase in thermal lensing with pumping power cannot be avoided for end-pumped amplifiers.
- With increased pumping power, the amplified spontaneous emission (ASE) increases. Spontaneously emitted photons get amplified and diminish the population inversion. In case of the presented amplifier, throughout all experiments, no ASE is visible as long as the amplifier is seeded. A small amount of ASE is observed starting at pumping powers of 70 W with a very sensitive detector card only (VRC2 - Thorlabs Inc.).

In two-pass configuration the amplifier is operated with both pumps active. The output pulse energy of the amplified pulses is recorded for varying input pulse energies and for a total of four pumping power levels (figure 7.4). For every change in pumping power, the spherical back reflector (SM) had to be repositioned to match the change in thermal lensing. Furthermore, the temperature of the gain crystal was adjusted to match the gain spectrum to the wavelength of the seed pulses. The maximal achieved output power was 7.49 W with the amplifier pumped at 86 W, which is slightly above the pump diodes specifications. The extraction efficiency η_e, when calculated conservatively with the stored energy $E_{\text{stored}} = P_p/f_{\text{rep}}$ defined by the total pump power P_p and the PRF f_{rep}, is 11.4%. The pulse energy of 1.5 mJ is already high enough to be used for the NextGen-PIRL, whose minimal pulse energy was derived to be 1.34 mJ (see introduction).

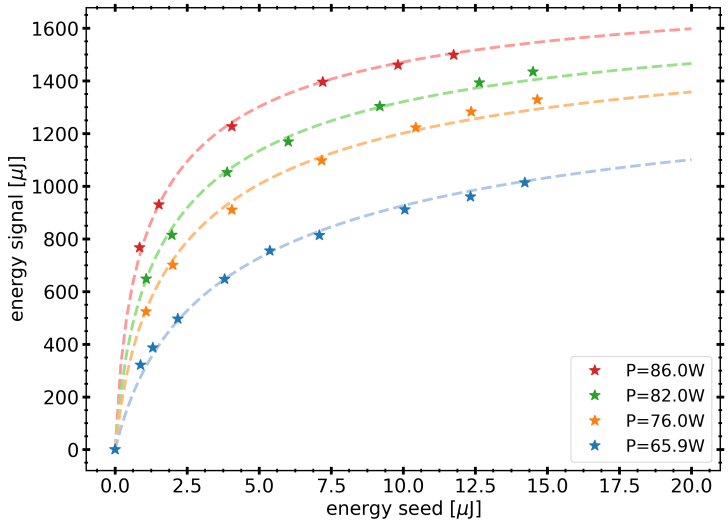

Figure 7.4: *Double pass amplification seeded by the MC03 laser. Output pulse energy is plotted over seeded energy for different pumping powers. Shown as solid lines are the fitted curves, retrieved from the Franz-Nodvik model, which is explained in section 7.4.*

The beam quality of the pulses after the amplifier is extraordinarily good. The beam profile at an output power of 7 W is Gaussian (figure 7.5), with a diameter ($1/e^2$) of 3.57×3.54 mm measured 1 m after the last mirror (TFP). No beam deformations are visible. A closer look at the beam quality reveals a M^2 factor of 1.24 (figure 7.6). That the amplifier does not add extra beam deterioration onto the seed was also reported by Martial *et al.*[87] for pump powers of up to at least 40 W. In the presented system, the total pump power of 80 W is split up into two pump-beams. Hence, the total heat is distributed within the crystal much more evenly then in the case of one pump only. This could explain the good beam quality at such a high pumping level.

In the beginning of the chapter the setup was compared to one used by Martial *et al.*[87], which resulted in an extraction efficiency of 33.9%. The definition for that extraction efficiency includes the loss of inversion during the pumping time due to finite lifetime of the upper laser level. With that definition, the extraction efficiency for the presented system is 24.3%. That remaining difference between these two values has several reasons. For one the pulse length of the MC03 laser is less than half of the system used by Martial, which leads to a stronger re-absorption from the lower laser level. Another reason is the stronger thermal lensing in the presented amplifier, due to several times higher pump powers. Hence, the presented setup has a smaller beam diameter within the amplifier and a worse pump to laser-mode overlap.

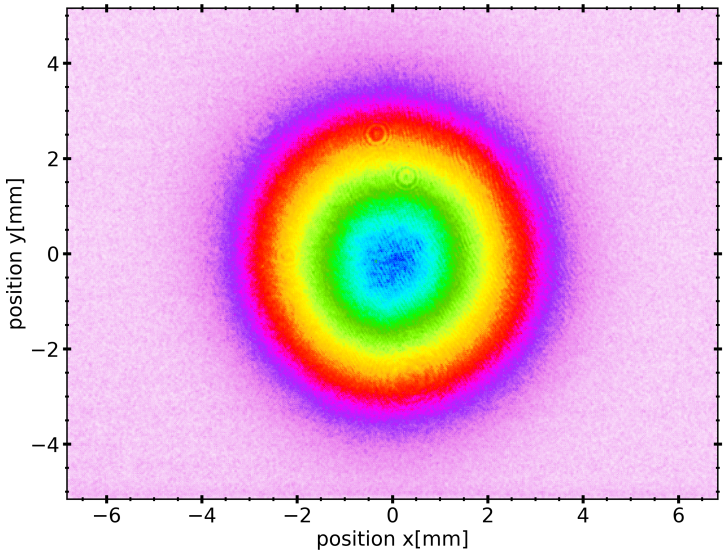

Figure 7.5: *Beam profile measured 1 m after the last mirror (TFP) of the amplifier running at an output power of 7 W. Measured beam diameters* $(1/e^2)$ *are 3.57×3.54 mm.*

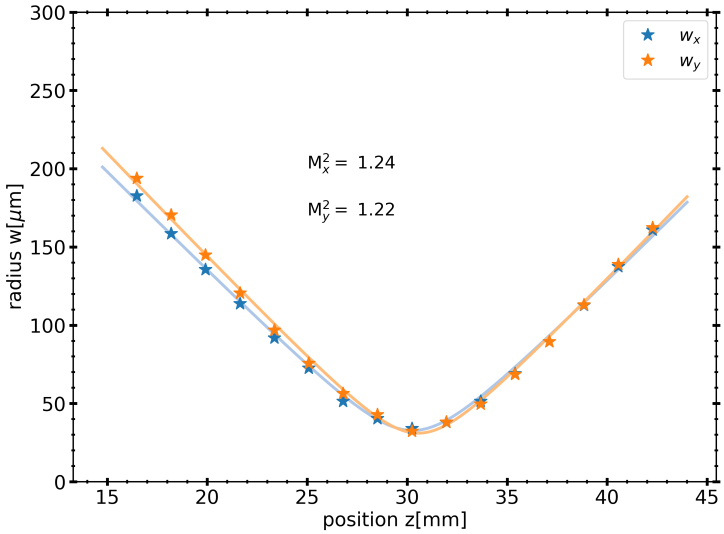

Figure 7.6: *Beam radii of the amplifies output beam measured around the focus of a* $f = 100$ *mm lens placed 1 m after the amplifier. The amplifier is operating at 7 W of output power. The resulting* M^2 *values are given.*

.

7.4 Franz-Nodvik Model

The Franz-Nodvik model can be applied to the gain curves from figure 7.4 to find the pumping power dependent small signal gain coefficient $g_0(P_p)$. The model was fit to the data to find the values g_0 and also the unknown gain reduction factor γ. There are several factors that lead to an increase in γ which ultimately results in a reduction of the saturation fluence $F_{sat} \propto \frac{1}{\gamma}$. Commonly γ can have values between one and two, one for an ideal four level system and two for the worst case of a three level laser. The used gain material Nd:YAG has a non-zero lower level lifetime, thus the γ factor has to be raised to a value that depends on the fractional populations f_u and f_l of the used Stark-levels within the upper and lower laser manifold and also on the relation between the pulse duration τ_p and the lower level lifetime $\tau_{11/2}$. For the extreme case of $\tau_p << \tau_{11/2}$ the value for the population reduction factor can be as high as $\gamma = 1 + \frac{f_l}{f_u} = 1.48$.

The next effect that raises γ is the thermal lensing within the amplifier. The amplifier is aligned while the pump modules are turned off, with the beam size being maximal at the entrance and exit surfaces of the crystal and the focus of the seed beam is in the crystal's center. When the pump modules are turned on, a thermal lens forms and the collimated beam becomes a converging beam within the crystal. A smaller beam diameter results in an increase in fluence, and as the fluence is always looked at in relation to the saturation fluence within the Franz-Nodvik model, it seems reasonable, that this effect can be added to the model by increasing the value for γ. Another effect that decreases the saturation fluence or increases the value for γ is the spatial hole burning. The seed laser emits a single frequency wave that is strongly modulated. Like in case of the microchip laser, this modulation leads to less available inversion to be extracted, and thus to a lower saturation fluence.

pump power [W]	g_0[1/cm]	$g_0\, l_{\text{gain}}$	γ
65.9	0.611	3.055	1.89
76.0	0.692	3.460	1.86
82.0	0.728	3.642	1.87
86.0	0.779	3.897	1.89

Table 7.1: *Franz-Nodvik model with parameters g_0 and γ fitted to the measured gain curves from figure 7.4.*

The resulting parameters g_0 and γ are shown in table 7.1. The values for γ are constant over the used pumping powers. The small signal gain coefficient on the other hand raises with increased pump power. With g_0 being proportional to the

population inversion, which itself is proportional to the pumping rate, g_0 should raise linearly with the pumping power. Figure 7.7 shows that this is the case for the amplifier system within the used pump power range. That the small signal gain does not roll-over is not surprising, as previous reports on that kind of amplifier system did show a linear raise in small signal gain depending on the seed power until at least 80 or even 110 W of pumping power [87, 88].

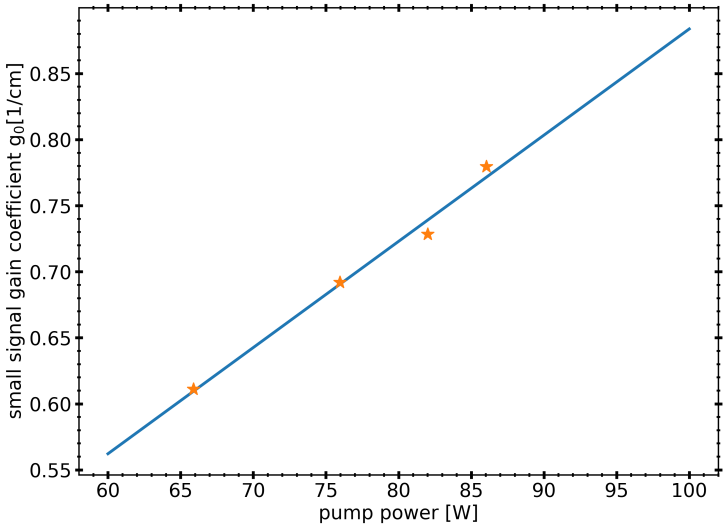

Figure 7.7: *Values for the small signal gain coefficient g_0 obtained by fitting the Frantz-Nodvik model to the retrieved data from figure 7.1. Data values plotted together with a linear regression line.*

In the characterization of the MC03 laser it was mentioned, that the pulse energy dropped drastically from 85 µJ with the MC01 laser down to 17 µJ with the stability optimized design. With the Franz-Nodvik model a definition for the extraction efficiency can be used which includes the fitted coefficients g_0 and γ with

$$\eta_e = \frac{F_{\text{out}} - F_{\text{in}}}{g_0 \, l_{\text{gain}} \, F_{\text{sat}}} \tag{7.6}$$

The coefficient g_0 can be seen as a measured value for the gain within the laser mode. The losses due to the laser mode being smaller than the pump mode are then ignored and the saturation fluence F_{sat} is already reduced by the measured γ. The extraction efficiency defined this way will be far bigger than in case of the previous definition that relates the output fluence to the total pump power. But with η_e given by Franz-Nodvik the change in extraction efficiency with varying input pulse energy can be studied. Figure 7.8 shows the extraction efficiencies for the different pumping rates. At the highest pumping power of 86 W and an

input pulse energy of 17 µJ an extraction efficiency as high as 90% is reached. Increasing the input pulse energy to 85 µJ by using the MC01 laser again, the extraction of the stored energy within the amplifier would only increase by another 8%. Hence, the drastic loss in pulse energy due to the stability optimizations does not compromise the output pulse energy of the amplifier system.

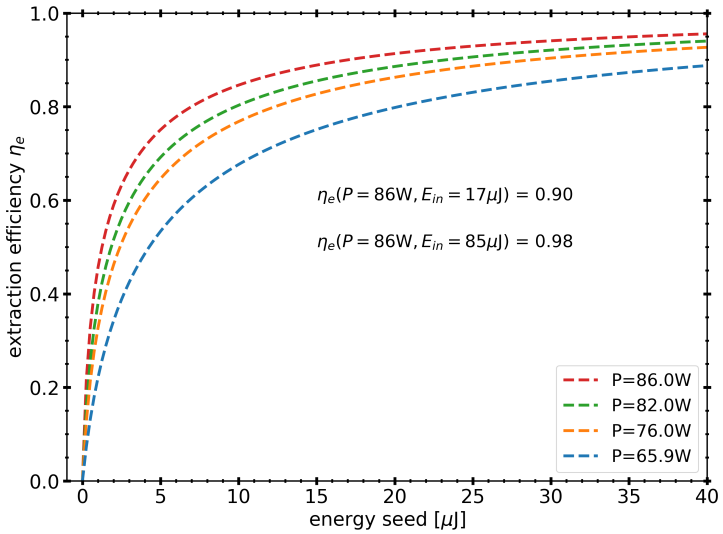

Figure 7.8: *Extraction efficiencies of the amplifier system according to values for g_0 and γ obtained by the Frantz-Nodvik model applied to the measured data from figure 7.1. Input pulse energies only shown till 40 µJ for better visibility.*

7.5 Scaling Capabilities

The experiments showed a linear raise in the small signal gain coefficient with pumping power. From previous reports it is known that this will not be the case when a certain pumping power is reached. Several effects contribute to that roll-over. For one the temperature gradient steepens within the gain crystal and thus the distribution of the spectra of the temperature dependent emission cross sections widens, which will ultimately result in a lowered average gain, even if the gain crystals outer surface is cooled to lower temperatures. A raise in the temperature gradient also leads to increased stress and thus to birefringence. Depolarization losses have been reported to start to happen at low pumping powers of 10 W and they reach values of 4% at 80 W [88]. The next contributing factor to loss in gain is pump bleaching. Calculating back from the retrieved values for the small signal gain coefficient, about 10% of the Nd ions are already excited at a pumping power of 80 W and with further increase of the pump power the pumping efficiency will drop. Another effect contributing to the extraction efficiency is the thermal lensing. As already mentioned, the beam diameter within the crystal shrinks with increased pumping power and with it the usable volume of inverted gain medium. For scaling the output power to higher levels, a method is needed to reduce the amount of heat deposited inside the gain crystal.

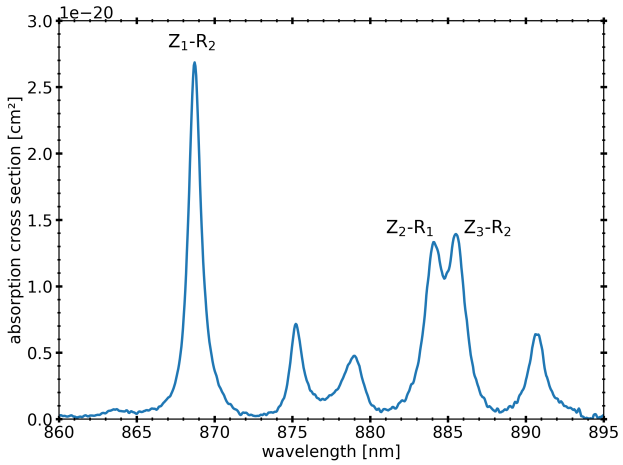

Figure 7.9: *Absorption cross sections of Nd:YAG for pumping into the $F_{3/2}$ upper laser level, taken from Kellner [81].*

The used pump modules populate the $F_{5/2}$ level of the Neodymium ions, from which the electrons relax into the $F_{3/2}$ upper laser level. The resulting quantum defect and thus the fraction of generated heat per pump power in the used system is 24%, including the phonon transition from the lower laser level to the ground level

of course. When pumping the Neodymium ions directly into the upper laser level, one phonon transition is left out and the fraction of heat is reduced down to 17%, depending on which Stark-levels from the ground and upper state manifold are addressed. The absorption cross section spectrum of Nd:YAG shows two possible pumping wavelengths (figure 7.9). The Z_1-R_2 transition at a wavelength around 869 nm has a relatively high peak absorption cross section and the overlapping Z_2-R_1 Z_3-R_2 transitions at around 885 nm feature a relatively wide spectral width. Pumping with a VBG stabilized diode at 869 nm would enable a reduction of the heat fraction down to 19% while still providing a pump absorption of 97% within the 50 mm long unbleached gain crystal. This absorption is basically the same as the 99% achieved by pumping into the $F_{5/2}$ band with an unstabilized diode. Pumping at 885 nm would enable a reduction of the heat fraction down to 17% while still providing a pump absorption of 86% within the gain crystal. The transmitted 14% could be reflected back into the amplifier with a spherical mirror, which would lead to a total absorption of up to 98%. Pumping the amplifier crystal with a VBG stabilized diode at 885 nm is a viable option. Scaling the used pumping power of 86 W with a heat fraction of 24% to pumping at 885 nm with a heat load of 17% gives a possible pump power of up to 120 W without increasing the heat load.

The Franz-Nodvik model is used in conjunction with the fitted regression of the small signal gain coefficient (figure 7.7) to calculate output pulse energies for increased pumping power P_p. At a $P_p = 120$W and a seed energy of 15 µJ, an output pulse energy of 2.27 mJ is reached. As shown before, the extraction efficiency is very close to optimal at such high pumping powers and with the given input pulse energy. At this energy level the set limit for the B-integral being below three is reached. Further increase in pulse energy would not be recommendable with this kind of amplifier system.

In the reports by Martial *et al.*[87], the available pumping power was 60 W and there was no sign of a roll-over. In the report by Rodin *et al.*[88] the crystal was pumped with up to 110 W and a roll-over in output power can only be seen merely for pump power levels over 80 W with low seed powers. When the seed power is high enough, a linear raise with no roll-over is seen for pump powers up to 110 W. This data suggests that the amplifier can be pumped with more than the 80 W available within the frame of this work.

The seed laser beam, the spherical back-reflector (SM) and the temperatures of all components where optimized at a pump power level of 86 W, then the pump power was varied and the output power measured without re-aligning or optimizing any components. The pump diodes where driven above their specified maximal output power of 80 W only for a short period, so the pump diodes did not get damaged, but long enough to measure the output power with a thermophile sensor. An output power of 8.2 W is reached with no sign of roll-over. Ultimately,

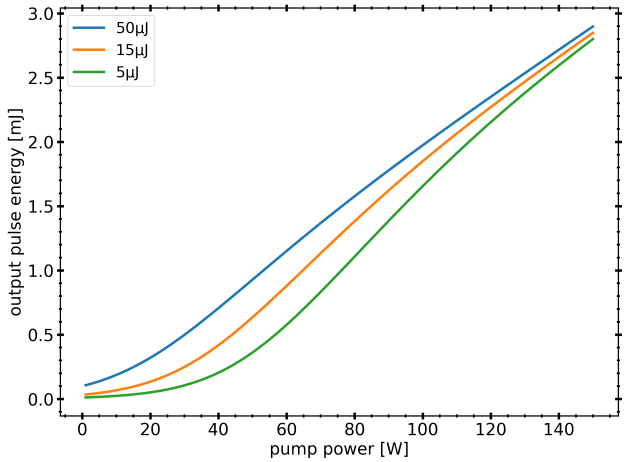

Figure 7.10: *Modeled (Franz-Nodvik) output pulse energies for direct upper laser level pumping. Output for three different input pulse energies are given (5, 15 and 50 µJ). The regression value of the small signal gain coefficient (figure 7.7) and an average γ of 1.88 are used as model parameters.*

the calculated maximum output power for the case of direct upper level pumping is likely not the upper limit that can be reached with this kind of amplifier in conjunction with the MC03 laser.

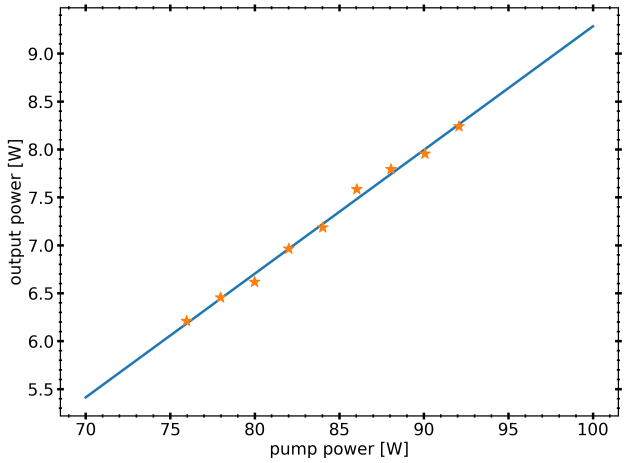

Figure 7.11: *Amplifier output power over pump power. The seed laser beam, the spherical back-reflector (SM) and the temperatures of the amplifier crystal and the pump diodes where optimized at a pump power level of 86 W, then the pump power was increased for a short period, enough to measure the output power. Data-points for pumping below 86 W where taken from a previous measurement series (see figure 7.4).*

7.6 Discussion

A fiber-crystal based two-pass amplifier was set up and characterized. The amplifier was able to produce an output power of up to 8.2 W when seeded with the stability optimized microchip laser MC03. The Franz-Nodvik model was used to investigate its scalability. The small signal gain coefficient showed a linear raise over the tested pumping powers. No roll-over was visible. This showed that the amplifier is so far only limited by the available pump power. Several factors contribute to the good scalability of the design:

- Care was taken to maximize the emission cross section by temperature controlling the crystal. The geometry in form of a fiber makes it possible to cool the whole crystal volume most efficiently. The lowest temperature for the heat sink used was 15 °C at a pumping power of 86 W.
- A very low doping level of only 0.2 at.% suppresses losses due to up-conversion or other two-ion processes. During all experiments no fluorescence light inside the amplifier was observable. This was the case for the microchip laser, which shows a bright glow where the pump-mode overlaps with the Nd:YAG crystal, even at low pumping powers.
- The low doping rate is also beneficial for the thermal conductivity of the crystal. The Neodymium ions do not fit perfectly into the Yttrium sites leading to a decrease in thermal conductivity for increased doping levels.
- The amplifier operated below the point of strong losses due to ASE. A certain onset of ASE could only be observed at pumping power of at least 70 W.

A possible different pumping regime was considered. Pumping directly into the upper laser level would reduce the heat load. Pumping with 885 nm and with up to 120 W should be possible without increasing the deposited heat in comparison to the experiments. An output power of over 11 W is predicted.

The presented crystal-fiber amplifier is a good match for the MC03 laser. The presented data shows that the low pulse energies of the microchip laser are high enough to drive the amplifier to saturation fluence levels. Simulations showed that a further increase in seed pulse energy would not result in a much higher output power. The high output power together with the good beam quality showed that this design is a viable amplifier for the NextGenPIRL design.

Chapter 8

Summary and Conclusion

Q-Switched Microchip

The aim of this thesis was to follow a Master Oscillator Power Amplifier (MOPA) design and identify limitations and scaling capabilities for a new laser system named the NextGenPIRL. As a master oscillator, a microchip design given by Zayhowski [83] was chosen to be the object of investigation. The microchip design was reported to run stable regarding its pulse energy at PRF of up to several kilohertz.

Within this work a numerical model to simulate the Q-switched microchip laser was developed. The model is based on the broadly used standard description developed by Degnan [55] using the time dependent average photon and population densities $\phi(t)$ and $n(t)$. These densities were extended by spacial components to $n(z,t)$ and $\phi(z,t)$, which enabled simulations of longitudinal mode based effects. The simulations showed that the microchip design suffers from severe pulse instabilities due to multi-longitudinal mode lasing. Spatial-hole burning causes the generation of L-mode satellite pulses which can even lead to mode-beating. Furthermore, mode-hopping between consecutive pulses where the main pulse hops between two or more longitudinal modes also lead to pulse energy instabilities.

These findings have all been reproduced experimentally within a first Q-switched microchip laser design (MC01). L-mode satellite pulses were seen both in the temporal pulse profile and in the recorded spectra. Starting at a PRF of 400 Hz, mode-hopping and pulse bifurcation could be identified spectrally and by recording a pulse energy distribution. The pulse energy distribution showed three distinct energy sections. Through analysis of the recorded temporal pulse profiles, the middle energy section can be related to pulses with strong mode-beating behavior and the outer energy sections can be related to hopping of the main pulse between two longitudinal modes. This three-fold energy distribution was reproduced in a second microchip design (MC02).

Several methods to enhance the stability of the Q-switched microchip laser by suppressing multi-longitudinal mode lasing have been introduced. (1) One way is

to increase the difference in emission cross section between the main mode and its neighbors by shortening the cavity length, which increases the mode spacing. (2) Cooling the crystal by several tens of Kelvin narrows the emission spectrum. (3) With fine-tuning the temperature, the main mode can be placed exactly at the emission peak wavelength. All these methods have been implemented in a new design (MC02). The optimizations led to a considerable improvement of the pulse energy stability. Mode hopping and mode beating was eliminated for PRF of up to 5 kHz. The laser ran stable in one longitudinal mode with a standard deviation in pulse-to-pulse energy of below 1 %. What could not be eliminated in this design was the generation of trailing L-mode satellite pulses. The drop in emission cross sections was increased through the optimizations, but it was not high enough to suppress the onset of L-mode satellite pulses completely.

Another method was introduced, which specifically suppresses direct neighboring modes. When the cavity is chosen to be asymmetrical in the lengths of the gain medium and of the absorber, the spatial-hole burning effect leads to a suppression of the direct neighboring modes. By shifting the gain medium towards the cavity end-mirror where direct neighbors overlap constructively with the main mode and by shifting the absorber over the cavity center where direct neighboring modes are out of phase with the main mode, the satellite mode overlaps mostly with regions of low gain and high absorption.

This method of multi-longitudinal mode suppression by choosing asymmetric lengths was implemented in a third design (MC03). Spectral and temporal analysis confirmed that the laser was emitting pulses in single longitudinal mode without satellite pulses up to a PRF of 5 kHz. The stability of the pulse energy was remarkable with a standard deviation of only 0.74%, and the pulse duration was determined to be as short as 226 ps. The laser was not sensitive to temperature fluctuations and stable operation in true single mode was possible even when the temperature of the crystal holder was varied by ± 1 °C. With further increased PRF of up to 10 kHz, the laser emitted single L-mode pulses with one trailing satellite pulse each. The deviation in total pulse energy stayed below 1 % and the pulse duration was 209 ps. The pulse energy dropped significantly between the designs. The first microchip laser (MC01) emitted pulses with an energy of up to 85 µJ and the last design (MC03) had a pulse energy of 17.4 µJ. The drop in energy is due to the shortening of the cavity and the strong cooling of the crystal down to -15 °C. Furthermore, the initial transmission of the saturable absorber was raised in between designs, to shorten the cavity, which also leads to a drop in pulse energy.

All in all, an effort was made to derive a numerical model for Q-switched lasers that is able to reproduce all longitudinal mode effects that appeared during the experimental investigations. Several authors have reported on single L-mode effects before [92, 79, 80, 86, 84, 77, 76, 78], but this work is the first

that includes and differentiates between all known and observed L-mode effects in Q-switched microchip lasers in both simulation and experiment. The effect of mode-beating for Q-switched microchip lasers is reported on for the first time including a method for identification without the usage of a fast oscilloscope. The suppression of multi-L-mode onset by strong cooling of the microchip and fine-tuning the emission cross sections by small temperature variations is elaborated here for the first time. This approach is shown to be simple and effective.

Compared to offerings on the market, the stability optimized microchip laser (MC03) sets a new standard. The company ALPHALAS GmbH (Göttingen, Germany) is offering sub-nanosecond Q-switched microchip lasers. Their model PULSELAS-P-1064-300-FC delivers 800 ps pulses at a PRF of 5 kHz with a pulse energy of 15 µJ. These parameters are very close to the MC03 laser, except for the pulse duration which is four times of the MC03 laser's and it is above the DIVE criteria with $\tau_p < 500$ ps. Furthermore, the company reports that their laser suffers from 10 to 20% fluctuations in pulse energy due to intrinsic laser dynamics starting at 3 kHz PRF. This is clearly a sign for multi-longitudinal mode lasing and ALPHALAS does not offer stable single-longitudinal mode systems. Since the year 2017, the company Teem Photonics (Meylan, France) is offering single longitudinal mode Q-switched microchip lasers, which suggests that all their other microchip lasers are unstable multi-mode designs. Their single-mode system is specified to deliver 500 ps long pulses and very low pulse energies in the 1 µJ to 2 µJ range. The company BATOP GmbH (Jena, Germany) is specialized in SESAM based microchip lasers delivering pulses with durations as short as 100 ps to 200 ps, but with even lower pulse energies in the sub-100 nJ range. From these companies and their product lines it can be deduced that single longitudinal mode operation in Q-switched microchip lasers is still hard to accomplish, especially when a high pulse energy in the 10 to 20 µJ-range is required. This work can help the industry to overcome that obstacle in the near future.

There is one effect that appeared during the experiments and the simulations that did not get mentioned in this work so far due to its complexity and it might be worth to be investigated further as it influences both the efficiency and the stability of the microchip laser. The pulse characteristics of a microchip laser are determined by the output coupling, the cavity length and the saturable absorber. The later is described by two parameters, which are the ground state and the excited state absorption cross sections. These parameters are strongly dependent on the doping level of the tetravalent Chromium ions in YAG, the manufacturer of the crystal and mostly on the investigator. The measured values vary by an order of magnitude between published reports [93, 94, 95, 96, 97, 98]. An overview of measured cross sections found in literature and more details can be found in the Appendix C. A reasonable explanation for the huge variation in measured cross sections is the existence of extra losses within the crystal, which are not directly

described by the two parameters. The incorporation of the Chromium ions into the Yttrium sites of the YAG crystal is suppressed by a difference in charge and size between these two ions. This can be addressed by co-doping the crystal with charge compensating ions, but ultimately it leads to residual ions in the crystal that are not embedded into its structure. The resulting extra losses are not addressed by the given models found in literature. A thorough investigation of this issue would be beneficial as it would enable a further optimization of the microchip laser towards even shorter pulse durations and higher pulse energies.

Fiber Amplifier

A crystal-fiber amplifier was setup to amplify the pulses to the mJ-regime. The fiber design has several benefits. For one internal reflections ensure a good overlap between the pump and the laser mode over a long distance. This enables the usage of a low doped crystal, which suppresses multi-ion processes and enhances thermal conductivity. Additionally, the small diameter enables very efficient cooling. With a pumping power of up to 86 W an output power of 7.49 W was achieved, which gives an extraction efficiency of 11.4%. The pulses had an energy of 1.5 mJ at a PRF of 5 kHz. The beam quality was exceptionally good with a M^2-factor of 1.24, a Gaussian shape and no ellipticity. The power of the pump diodes was increased for a short period above the manufacturers specifications, which resulted in an output power of 8.2 W.

An analysis of the measured output pulse energies over varying input pulse energies and pumping powers was performed, by fitting the Franz-Nodvik model to the data. It turned out that the amplifier is perfectly suited for the MC03 laser. Even though the seeded pulse energy is very low, the amplifier achieved several times the saturation fluence due to the high gain and the double-pass geometry. The extraction efficiency with the low seeding pulse energy of 15 µJ was already at 90% of what is achievable according to the Franz-Nodvik model. The analysis also revealed an inversion or saturation fluence reduction factor γ of 1.9, which can be explained by (1) re-absorption due to the non-zero lower level lifetime, (2) the narrowed mode diameter due to thermal lensing and (3) spatial-hole burning effect due to the single mode character of the seed laser. Furthermore, the analysis showed a linear raise in the small signal gain coefficient over the used pumping power range. Hence, the amplifier's output power was only limited by the available pump power.

The ultimate scalability of the amplifier could not be achieved experimentally within this work as a pump diode with sufficient output power was not at our disposal. Several companies like Dilas Diodenlaser GmbH (Mainz, Germany) and nLight Inc. (Vancouver, USA) offer frequency stabilized fiber coupled pump modules for direct upper level pumping of Nd:YAG with output powers of up to

200 W and a fiber core diameter of 200 µm. Upgrading the amplifier with such a high power diode would enable an investigation on ultimate output powers.

NextGenPIRL

The MOPA laser system as implemented and presented has shown to be a viable design for the NextGenPIRL. The condition for the minimum pulse energy was determined to be 1.37 mJ in order to reach the necessary fluence level for a typical DIVE setup (see introduction). The current system delivers an output pulse energy of 1.5 mJ and with an upgraded pump diode, laser pulse energies of above 2 mJ can be reached. The pulse duration of the presented MOPA is 2.4 times shorter than the needed 500 ps to ensure stress confinement. The average output power is four times of what was achieved with the previous regenerative amplifier design [16]. Hence, four times higher cutting speeds can be expected. The system is also compact, simple and robust. It offers low-maintenance operation and the possibility to be transported between the laser lab and a medical clinic.

A crucial part to generate the Mid-IR pulses is the OPA. The first DIVE experiments from Franjic *et al.*[16] were performed with a PIRL system with attached KTA based OPA with collinear type-II phase matching. The OPA was seeded by a fiber coupled distributed feedback (DFB) diode laser and the resulting idler pulses had a wavelength of 2.96 µm. For applications of DIVE in surgery and biodiagnostics in Hamburg [21, 22, 28, 29] a commercial PIRL system with attached OPA was used. That OPA was similar in construction to the first one from Franjic *et al.*[16]. The amplification was performed in a single stage pumped by 400 ps to 500 ps pulses with 7 mJ of energy, resulting in 700 µJ pulses in the Mid-IR. The power of the cw-seed can be estimated with 10 mW, which gives a total gain G of 2.5×10^{8}. Due to the gain-guiding effect, the seed and idler beams shrink in diameter within the OPA. This effect has been described by Arisholm *et al.*[99] in detail. Starting with an initial beam diameter of the seed and pump beams of typically 1 mm, the gain guiding effect can shrink the diameter of both signal and idler down to 100 µm or even less, which is far smaller than the diameter of the pump beam. The resulting output is a mixture of seeded OPA idler at the center overlapped with unseeded amplified fluorescence light. Beam quality factors of up to ten have been measured with this kind of OPA [21]. A promising route towards a better output beam quality of the Mid-IR idler is to investigate the beam-guiding effect in the OPA in more detail. Switching from a one-stage OPA to a two or more stage system will reduce the gain per stage and suppresses the gain-guiding effect. This upgrade would lead to a better beam quality and a better focusability of the laser.

Alternative ways to generate picosecond Mid-IR pulses do exist, which could also be the basis for a NextGenPIRL. For example, Erbium ions emit light in the

2.7 to 2.94 µm wavelength range, depending on the host material. Erbium lasers generating pulses with durations around 100 ns and with output powers in the Watt range have been reported on [100, 101]. To generate few-100 ps pulses the cavity has to be very short with a few millimeters in length. Hence, an inversion density has to be reached that is far higher than in the mentioned systems that used few centimeter long Erbium crystals. The first step in designing an Erbium Mid-IR PIRL would be to investigate if high levels of inversion can be reached, even though Erbium suffers from strong up-conversion processes from the upper laser level [102].

Appendix A

List of Publications

Hannes Petersen, Fatemeh Tavakoli, Sebastian Kruber, Adrian Münscher, Alexandra Gliese, Nils-Owe Hansen, Stephanie Uschold, Dennis Eggert, Wesley D. Robertson, Tobias Gosau, Susanne Sehner, Marcel Kwiatkowski, Hartmut Schlüter, Udo Schumacher, Rainald Knecht, and R.J. Dwayne Miller. "Comparative study of wound healing in rat skin following incision with a novel picosecond infrared laser (PIRL) and different surgical modalities." In: *Lasers in Surgery and Medicine* 48.4 (2016), pp. 385–391. ISSN: 01968092. DOI: 10.1002/lsm.22498.

Markus Hess, Michael Dominik Hildebrandt, Frank Müller, Sebastian Kruber, Peter Kroetz, Udo Schumacher, Rudolph Reimer, Michael Kammal, Klaus Püschel, Wolfgang Wöllmer, and Dwayne Miller. "Picosecond infrared laser (PIRL): an ideal phonomicrosurgical laser?" In: *European Archives of Oto-Rhino-Laryngology* 270.11 (2013), pp. 2927–2937. ISSN: 0937-4477. DOI: 10.1007/s00405-013-2561-6.

Marcel Kwiatkowski, Marcus Wurlitzer, Maryam Omidi, Ling Ren, Sebastian Kruber, Refat Nimer, Wesley D. Robertson, Andrea Horst, R. J. Dwayne Miller, and Hartmut Schlüter. "Ultrafast Extraction of Proteins from Tissues Using Desorption by Impulsive Vibrational Excitation." In: *Angewandte Chemie International Edition* 54.1 (2015), pp. 285–288. ISSN: 14337851. DOI: 10.1002/anie.201407669.

M. Kwiatkowski, M. Wurlitzer, A. Krutilin, P. Kiani, R. Nimer, M. Omidi, A. Mannaa, T. Bussmann, K. Bartkowiak, S. Kruber, S. Uschold, P. Steffen, J. Lübberstedt, N. Küpker, H. Petersen, R. Knecht, N.O. Hansen, A. Zarrine-Afsar, W.D. Robertson, R.J.D. Miller, and H. Schlüter. "Homogenization of tissues via picosecond-infrared laser (PIRL) ablation: Giving a closer view on the in-vivo composition of protein species as compared to mechanical homogenization." In: *Journal of Proteomics* 134 (2016), pp. 193–202. ISSN: 18743919. DOI: 10.1016/j.jprot.2015.12.029.

Hannes Petersen, Alexandra Gliese, Yannick Stober, Stephanie Maier, Nils-Owe Hansen, Sebastian Kruber, Dennis Eggert, Miklós Tóth, Tobias Gosau, Hartmut Schlüter, Klaus Püschel, Udo Schumacher, Robert John Dwayne Miller, Adrian Münscher, and Carsten Dalchow. "Picosecond Infrared Laser (PIRL) Application in Stapes Surgery - First Experience in Human Temporal Bones." In: *Otology & Neurotology* 39.4 (2018), e224–e230. ISSN: 1531-7129. DOI: 10.1097/MAO.0000000000001753.

S. Maier, N.-O. Hansen, S. Kruber, T. Gosau, D. Eggert, A. Gliese, H. Petersen, H. Schlüter, and R. J. D. Miller. "Wound Healing Study and Ablation Rate Measurements with the Novel Picosecond Infrared Laser (PIRL)." In: *Conference on Lasers and Electro-Optics*. Optical Society of America, 2017, ATu3A.5. DOI: 10.1364/CLEO_AT.2017.ATu3A.5.

Submitted

M. Wurlitzer, E. Hessling, K. Rinas, M. Fuh, Dr. H. Petersen, Dr. F. Ricklefs, Dr. K. Lamszus, Dr. J. Regelsberger, S. Maier, S. Kruber, Dr. N. Hansen, Dr. RJ D. Miller, and Dr. H. Schlüter. "Mass Spectrometric Lipid Profiles of Picosecond Infrared Laser Generated Tissue Aerosols Discriminate Different Brain Areas." In: *Journal of Lipid Research* (submitted 2018).

Frederik Busse, Sebastian Kruber, Wesley D Robertson, and R J Dwayne Miller. "Digital Interference Microscopy and Density Reconstruction of Picosecond Infrared Laser Desorption at the Water-Air Interface." In: *Journal of Applied Physics* (submitted 2018).

Patent

R.J. Dwayne Miller, Stephanie Maier, Sebastian Kruber, and Nils-Owe Hansen. *Laser Surgery Apparatus For Contact Laser Surgery*. 2017, EP3067005B1.

Previous Project

J. A. Fülöp, Zs Major, A. Henig, S. Kruber, R. Weingartner, T. Clausnitzer, E-B Kley, A. Tünnermann, V. Pervak, A. Apolonski, J. Osterhoff, R. Hörlein, F. Krausz, and S. Karsch. "Short-pulse optical parametric chirped-pulse amplification for the generation of high-power few-cycle pulses." In: *New Journal of Physics* 9.12 (2007), pp. 438–438. DOI: 10.1088/1367-2630/9/12/438.

Appendix B

Crystal Constants and Coefficients

The following crystal constants and thermo-optic coefficients have been used for the calculations and simulations within this work.

Crystal Constants

acronym	YAG	YSGG	Lutetia	YLF
formula	$Y_3Al_5O_{12}$	$Y_3Sc_2Ga_3O_{12}$	Lu_2O_3	$LiYF_4$
symmetry	cubic	cubic	cubic	tetragonal
lattice constant $[\mathring{A}]$	12.00	12.43	10.39	5.18(10.74)
cation density $[10^{20}\text{cm}^3]$	139 Y^{3+}	125 Y^{3+}	285 Lu^{3+}	139 Y^{3+}
melting point [°C]	1930	1780	2450	850
hardness [Mohs]	8.5	7.5	6.5	4.5
density [g/cm^3]	4.56	4.55	9.42	3.99
Poisson ratio	0.24	0.30 [2]	0.29	0.33
max. phonon energy [cm^{-1}]	672	500	618	442

Table B.1: *Material properties of undoped crystals.*

[2] estimated value

	YAG	YSGG	Lutetia	YLF
symmetry	[66]	[108]	[109]	[110]
lattice constant	[66]	[111]	[112]	[110]
cation density	[110]	[113]	[112]	[110]
melting point	[113]	[113]	[114]	[113]
hardness	[114]	[113]	[114]	[113]
density	[108]	[108]	[112]	[108]
Poisson ratio	[108]	n.a.	[115]	[43]
max. phonon energy	[116]	[113]	[114]	[113]

Table B.2: *References to material properties from table B.1.*

material	C_{11}	C_{12}	C_{44}	reference
YAG	3.49	1.21	1.14	[108]
YSGG	2.75	1.00	0.85	[108]

Table B.3: *Elastic constants for cubic crystals in 10^{11} N/m^2 at room temperature.*

material	C_{11}	C_{12}	C_{13}	C_{16}	C_{33}	C_{44}	C_{66}	reference
YLF	1.21	0.609	0.526	-0.077	1.56	0.409	0.177	[108]

Table B.4: *Elastic constants for tetragonal crystals in 10^{11} N/m^2.*

Thermo-optic Properties

material	Sellmeier equation	ref.
YAG	$n^2-1=\frac{2.28200\lambda^2}{\lambda^2-0.01185}+\frac{3.27644\lambda^2}{\lambda^2-282.734}$	[117]
YSGG	$n^2-1=\frac{2.628\lambda^2}{\lambda^2-0.127^2}$	[118]
YLF	$n^2-1=0.38757+\frac{0.70757\lambda^2}{\lambda^2-0.00931}+\frac{0.18849\lambda^2}{\lambda^2-50.99741}$	[119]
Lutetia	$n^2-1=0.83439+\frac{1.7837\lambda^2}{\lambda^2-0.15242^2}+\frac{8.07129\lambda^2}{\lambda^2-30.76181^2}$	[120]

Table B.5: *Sellmeier equations for several undoped host crystals.*

	temperature [K]		
	300	250	200
β[cm^2/s]	0.041	0.056	0.091
	(0.032)	(0.043)	(0.068)
C_p[J/gK]	0.60	0.52	0.42
	(0.58)	(0.51)	(0.41)
κ[W/mK]	11.2	13.4	17.6
	(8.6)	(10.2)	(13.0)

Table B.6: *Thermal coefficients for undoped and doped YAG over temperatures. The doped YAG crystal contained 2 at.% Ytterbium and the corresponding values are written in brackets. Data is taken from Aggarwal et al.[121].*

	temperature [K]					
	300	280	260	240	220	200
$\alpha[10^{-6}/K]$	6.14	5.92	5.66	5.36	5.01	4.61
$\frac{dn}{dT}[10^{-6}/K]$	7.8	7.3	6.7	6.1	5.5	4.8

Table B.7: *Coefficient for thermal expansion and refractive index change over temperature for undoped YAG taken from Aggarwal et al.[121].*

Appendix C

Cross Sections for Cr^{4+}:YAG

When doping YAG crystals with tetravalent Chromium ions, a charge compensation in form of a divalent ion is needed. Kalisky *et al.*[93] retrieved the absorption cross sections of the ground and excited state of Cr^{4+}:YAG co-doped with Ca^{2+} ions. Later Lipavsky *et al.*[95] retrieved the absorption cross sections of Cr^{4+}:YAG co-doped with Mg^{2+} ions. The two measurements show a dependency of the excited state absorption on the co-dopant ion. Several other groups re-measured the cross sections [94, 97, 98]. Xiao *et al.*[96] determined the cross sections for several Cr^{4+}:YAG crystals grown by different manufacturers.

	σ_{abs} $[10^{-18}cm^2]$	σ_{esa} $[10^{-18}cm^2]$	$\sigma_{abs}/\sigma_{esa}$	comment
Kalisky [93]	3.2	0.45	7.1	Ca^{2+} co-doped
Lipavsky [95]	3.25	0.625	5.2	Mg^{2+} co-doped
Burshtein [94]	7.0	2.0	3.5	
Xiao [96]	1.9	0.5	3.8	man. #1, low-dop.
	1.6	0.5	3.2	man. #1, high-dop.
	1.8	0.4	4.5	man. #2, low-dop.
	1.7	0.5	3.4	man. #2, high-dop.

Table C.1: *Retrieved values for ground state σ_{abs} and excited state σ_{esa} absorption cross sections of Cr^{4+}:YAG. Xiao et al.[96] compared crystals from different manufacturers (man.) and with different doping levels (low and high dop.).*

The retrieved values from Xiao *et al.*[96] where used for the calculations and simulations within this work (see table C.1, crystal from manufacturer #1 with high doping level).

Bibliography

[1] W.E. Gerabek and W. Gerabek. *Enzyklopädie Medizingeschichte*. Walter de Gruyter, 2005. ISBN: 9783110157147.

[2] Venera A. Shaimova, Ernest V. Boyko, and Olga G. Pozdeeva. "Retinal Laser Photocoagulation in Peripheral Retinal Degenerations." In: *Peripheral Retinal Degenerations: Optical Coherence Tomography and Retinal Laser Coagulation*. Ed. by Venera A. Shaimova. Cham: Springer International Publishing, 2017, pp. 209–227. ISBN: 978-3-319-48995-7. DOI: 10.1007/978-3-319-48995-7_7.

[3] G. Friedrich, F. G. Dikkers, C. Arens, M. Remacle, M. Hess, A. Giovanni, S. Duflo, A. Hantzakos, V. Bachy, and M. Gugatschka. "Vocal fold scars: current concepts and future directions. Consensus report of the phonosurgery committee of the European laryngological society." In: *European Archives of Oto-Rhino-Laryngology* 270.9 (2013), pp. 2491–2507. ISSN: 1434-4726. DOI: 10.1007/s00405-013-2498-9.

[4] Kavitha Reddy, Lori Brightman, and Roy Geronemus. "Laser treatment of port-wine stains." In: *Clinical, Cosmetic and Investigational Dermatology* 8 (2015), p. 27. ISSN: 1178-7015. DOI: 10.2147/CCID.S53118.

[5] R. Anderson and J. Parrish. "Selective photothermolysis: precise microsurgery by selective absorption of pulsed radiation." In: *Science* 220.4596 (1983), pp. 524–527. ISSN: 0036-8075. DOI: 10.1126/science.6836297.

[6] Willem G. Zijlstra. *Visible and Near Infrared Absorption Spectra of Human and Animal Haemoglobin determination and application*. CRC Press, 2000. ISBN: 9067643173.

[7] Alfred Vogel and Vasan Venugopalan. "Mechanisms of Pulsed Laser Ablation of Biological Tissues." In: *Chemical Reviews* 103.2 (2003), pp. 577–644. ISSN: 0009-2665. DOI: 10.1021/cr010379n.

[8] John E. Bertie and Zhida Lan. "Infrared Intensities of Liquids XX: The Intensity of the OH Stretching Band of Liquid Water Revisited, and the Best Current Values of the Optical Constants of H2O(l) at 25°C between 15,000 and 1 cm-1." In: *Appl. Spectrosc.* 50.8 (1996), pp. 1047–1057.

[9] Alfred Vogel, Ingo Apitz, and Vasan Venugopalan. “Phase transitions , material ejection , and plume dynamics in pulsed laser ablation of soft biological tissues.” In: (2007), pp. 217–258.

[10] I. Apitz and A. Vogel. “Material ejection in nanosecond Er:YAG laser ablation of water, liver, and skin.” In: *Applied Physics A* 81.2 (2005), pp. 329–338. ISSN: 0947-8396. DOI: 10.1007/s00339-005-3213-5.

[11] R O Esenaliev, a a Oraevsky, V S Letokhov, a a Karabutov, and T V Malinsky. “Studies of acoustical and shock waves in the pulsed laser ablation of biotissue.” In: *Lasers in surgery and medicine* 13 (1993), pp. 470–484. ISSN: 0196-8092. DOI: 10.1002/lsm.1900130412.

[12] KL Vodopyanov, LA Kulevsky, VG Mikhalevich, and AM Rodin. “Laser-induced generation of subnanosecond sound pulses in liquids.” In: *Sov. Phys. JETP* 64.1 (1986), pp. 67–70.

[13] Ronald S Dingus and Richard J Scammon. “Gruenneisen-stress-induced ablation of biological tissue.” In: ed. by Steven L. Jacques. Vol. 1427. June 1991. 1991, pp. 45–54. DOI: 10.1117/12.44088.

[14] Alexander A. Oraevsky, Steven L. Jacques, Rinat O. Esenaliev, and Frank K. Tittel. “Pulsed laser ablation of soft tissues, gels, and aqueous solutions at temperatures below 100°C.” In: *Lasers in Surgery and Medicine* 18.3 (), pp. 231–240. DOI: 10.1002/(SICI)1096-9101(1996)18:3<231::AID-LSM3>3.0.CO;2-T. eprint: https://onlinelibrary.wiley.com/doi/pdf/10.1002/%28SICI%291096-9101%281996%2918%3A3%3C231%3A%3AAID-LSM3%3E3.0.CO%3B2-T.

[15] Günther Paltauf and Peter E. Dyer. “Photomechanical Processes and Effects in Ablation.” In: *Chemical Reviews* 103.2 (2003). PMID: 12580640, pp. 487–518. DOI: 10.1021/cr010436c. eprint: https://doi.org/10.1021/cr010436c.

[16] Kresimir Franjic, Michael L. Cowan, Darren Kraemer, and R. J. Dwayne Miller. “Laser selective cutting of biological tissues by impulsive heat deposition through ultrafast vibrational excitations.” In: *Opt. Express* 17.25 (2009), pp. 22937–22959. DOI: 10.1364/OE.17.022937.

[17] Zhao-Zhang Li, James E. Code, and Willem P. Van de Merwe. “Er:YAG laser ablation of enamel and dentin of human teeth: Determination of ablation rates at various fluences and pulse repetition rates.” In: *Lasers in Surgery and Medicine* 12.6 (Jan. 1992), pp. 625–630. ISSN: 1096-9101. DOI: 10.1002/lsm.1900120610.

[18] C. Apel, J. Meister, R.S. Ioana, R. Franzen, P. Hering, and N. Gutknecht. "The Ablation Threshold of Er:YAG and Er:YSGG Laser Radiation in Dental Enamel." In: *Lasers in Medical Science* 17.4 (2002), pp. 246–252. ISSN: 1435-604X. DOI: 10.1007/s101030200036.

[19] Daniel Fried, Nahal Ashouri, Thomas Breunig, and Ramesh Shori. "Mechanism of water augmentation during IR laser ablation of dental enamel." In: *Lasers in Surgery and Medicine* 31.3 (Sept. 2002), pp. 186–193. ISSN: 1096-9101. DOI: 10.1002/lsm.10085.

[20] Saeid Amini-Nik, Darren Kraemer, Michael L Cowan, Keith Gunaratne, Puviindran Nadesan, Benjamin A Alman, and R J Dwayne Miller. "Ultrafast Mid-IR Laser Scalpel: Protein Signals of the Fundamental Limits to Minimally Invasive Surgery." In: *PLoS ONE* 5.9 (2010). Ed. by Michael Polymenis, e13053. ISSN: 1932-6203. DOI: 10.1371/journal.pone.0013053.

[21] Hannes Petersen, Fatemeh Tavakoli, Sebastian Kruber, Adrian Münscher, Alexandra Gliese, Nils-Owe Hansen, Stephanie Uschold, Dennis Eggert, Wesley D. Robertson, Tobias Gosau, Susanne Sehner, Marcel Kwiatkowski, Hartmut Schlüter, Udo Schumacher, Rainald Knecht, and R.J. Dwayne Miller. "Comparative study of wound healing in rat skin following incision with a novel picosecond infrared laser (PIRL) and different surgical modalities." In: *Lasers in Surgery and Medicine* 48.4 (2016), pp. 385–391. ISSN: 01968092. DOI: 10.1002/lsm.22498.

[22] Markus Hess, Michael Dominik Hildebrandt, Frank Müller, Sebastian Kruber, Peter Kroetz, Udo Schumacher, Rudolph Reimer, Michael Kammal, Klaus Püschel, Wolfgang Wöllmer, and Dwayne Miller. "Picosecond infrared laser (PIRL): an ideal phonomicrosurgical laser?" In: *European Archives of Oto-Rhino-Laryngology* 270.11 (2013), pp. 2927–2937. ISSN: 0937-4477. DOI: 10.1007/s00405-013-2561-6.

[23] Arne Böttcher, Till S Clauditz, Rainald Knecht, Stanislav Kucher, Wolfgang Wöllmer, Waldemar Wilczak, Peter Krötz, Nathan Jowett, Carsten V Dalchow, Adrian Münscher, and R J Dwayne Miller. "A novel tool in laryngeal surgery: Preliminary results of the picosecond infrared laser." In: *The Laryngoscope* 123.11 (2013), pp. 2770–2775. ISSN: 0023852X. DOI: 10.1002/lary.24124.

[24] Arne Böttcher, Till S Clauditz, Rainald Knecht, Stanislav Kucher, Wolfgang Wöllmer, Waldemar Wilczak, Peter Krötz, Nathan Jowett, Carsten V Dalchow, Adrian Münscher, and R J Dwayne Miller. "A novel tool in laryngeal surgery: Preliminary results of the picosecond infrared laser." In:

The Laryngoscope 123.11 (2013), pp. 2770–2775. ISSN: 0023852X. DOI: 10.1002/lary.24124.

[25] Nathan Jowett, Wolfgang Wöllmer, Alex M. Mlynarek, Paul Wiseman, Bernard Segal, Kresimir Franjic, Peter Krötz, Arne Böttcher, Rainald Knecht, and R J Dwayne Miller. "Heat Generation During Ablation of Porcine Skin With Erbium:YAG Laser vs a Novel Picosecond Infrared Laser." In: *JAMA Otolaryngology–Head & Neck Surgery* 139.8 (2013), p. 828. ISSN: 2168-6181. DOI: 10.1001/jamaoto.2013.3974.

[26] Nathan Jowett, Wolfgang Wöllmer, Rudolph Reimer, Jozef Zustin, Udo Schumacher, Paul W Wiseman, Alex M. Mlynarek, Arne Böttcher, Carsten V Dalchow, Balazs B. Lörincz, Rainald Knecht, and R J Dwayne Miller. "Bone Ablation without Thermal or Acoustic Mechanical Injury via a Novel Picosecond Infrared Laser (PIRL)." In: *Otolaryngology-Head and Neck Surgery* 150.3 (2014), pp. 385–393. ISSN: 0194-5998. DOI: 10.1177/0194599813517213.

[27] S.J. Linke, L. Ren, A. Frings, J. Steinberg, W. Wöllmer, T. Katz, R. Reimer, N.O. Hansen, N. Jowett, G. Richard, and R.J. Dwayne Miller. "Perspektiven der laserassistierten Keratoplastik." In: *Der Ophthalmologe* 111.6 (2014), pp. 523–530. ISSN: 0941-293X. DOI: 10.1007/s00347-013-2995-7.

[28] Marcel Kwiatkowski, Marcus Wurlitzer, Maryam Omidi, Ling Ren, Sebastian Kruber, Refat Nimer, Wesley D. Robertson, Andrea Horst, R. J. Dwayne Miller, and Hartmut Schlüter. "Ultrafast Extraction of Proteins from Tissues Using Desorption by Impulsive Vibrational Excitation." In: *Angewandte Chemie International Edition* 54.1 (2015), pp. 285–288. ISSN: 14337851. DOI: 10.1002/anie.201407669.

[29] M. Kwiatkowski, M. Wurlitzer, A. Krutilin, P. Kiani, R. Nimer, M. Omidi, A. Mannaa, T. Bussmann, K. Bartkowiak, S. Kruber, S. Uschold, P. Steffen, J. Lübberstedt, N. Küpker, H. Petersen, R. Knecht, N.O. Hansen, A. Zarrine-Afsar, W.D. Robertson, R.J.D. Miller, and H. Schlüter. "Homogenization of tissues via picosecond-infrared laser (PIRL) ablation: Giving a closer view on the in-vivo composition of protein species as compared to mechanical homogenization." In: *Journal of Proteomics* 134 (2016), pp. 193–202. ISSN: 18743919. DOI: 10.1016/j.jprot.2015.12.029.

[30] Hannes Petersen, Alexandra Gliese, Yannick Stober, Stephanie Maier, Nils-Owe Hansen, Sebastian Kruber, Dennis Eggert, Miklós Tóth, Tobias Gosau, Hartmut Schlüter, Klaus Püschel, Udo Schumacher, Robert John

Dwayne Miller, Adrian Münscher, and Carsten Dalchow. "Picosecond Infrared Laser (PIRL) Application in Stapes Surgery - First Experience in Human Temporal Bones." In: *Otology & Neurotology* 39.4 (2018), e224–e230. ISSN: 1531-7129. DOI: 10.1097/MAO.0000000000001753.

[31] L Ren, W D Robertson, R Reimer, C Heinze, C Schneider, D Eggert, P Truschow, N-O Hansen, P Kroetz, J Zou, and R J D Miller. "Towards instantaneous cellular level bio diagnosis: laser extraction and imaging of biological entities with conserved integrity and activity." In: *Nanotechnology* 26.28 (2015), p. 284001. ISSN: 0957-4484. DOI: 10.1088/0957-4484/26/28/284001.

[32] Eike C. Schulz, Johannes Kaub, Frederik Busse, Pedram Mehrabi, Henrike M. Müller-Werkmeister, Emil F. Pai, Wesley D. Robertson, and R. J. Dwayne Miller. "Protein crystals IR laser ablated from aqueous solution at high speed retain their diffractive properties: applications in high-speed serial crystallography." In: *Journal of Applied Crystallography* 50.6 (2017), pp. 1773–1781. DOI: 10.1107/S1600576717014479.

[33] J. Zou, C. Wu, W. D. Robertson, L. V. Zhigilei, and R. J. D. Miller. "Molecular dynamics investigation of desorption and ion separation following picosecond infrared laser (PIRL) ablation of an ionic aqueous protein solution." In: *The Journal of Chemical Physics* 145.20 (2016), p. 204202. DOI: 10.1063/1.4967164. eprint: https://doi.org/10.1063/1.4967164.

[34] Michael Woolman, Isabelle Ferry, Claudia[space]M. Kuzan-Fischer, Megan Wu, Jing Zou, Taira Kiyota, Semra Isik, Delaram Dara, Ahmed Aman, Sunit Das, Michael D. Taylor, James T. Rutka, Howard J. Ginsberg, and Arash Zarrine-Afsar. "Rapid determination of medulloblastoma subgroup affiliation with mass spectrometry using a handheld picosecond infrared laser desorption probe." In: *Chem. Sci.* 8 (9 2017), pp. 6508–6519. DOI: 10.1039/C7SC01974B.

[35] Michael Woolman, Alessandra Tata, Delaram Dara, Jalna Meens, Elisa D'Arcangelo, Consuelo J. Perez, Shamina Saiyara Prova, Emma Bluemke, Howard J. Ginsberg, Demian Ifa, Alison McGuigan, Laurie Ailles, and Arash Zarrine-Afsar. "Rapid determination of the tumour stroma ratio in squamous cell carcinomas with desorption electrospray ionization mass spectrometry (DESI-MS): a proof-of-concept demonstration." In: *Analyst* 142 (17 2017), pp. 3250–3260. DOI: 10.1039/C7AN00830A.

[36] Jing Zou, Francis Talbot, Alessandra Tata, Leonardo Ermini, Kresimir Franjic, Manuela Ventura, Jinzi Zheng, Howard Ginsberg, Martin Post,

Demian R. Ifa, David Jaffray, R. J. Dwayne Miller, and Arash Zarrine-Afsar. "Ambient Mass Spectrometry Imaging with Picosecond Infrared Laser Ablation Electrospray Ionization (PIR-LAESI)." In: *Analytical Chemistry* 87.24 (2015). PMID: 26561279, pp. 12071–12079. DOI: 10.1021/acs.analchem.5b02756. eprint: https://doi.org/10.1021/acs.analchem.5b02756.

[37] John Cameron. "Physical Properties of Tissue. A Comprehensive Reference Book, edited by Francis A. Duck." In: *Medical Physics* 18.4 (1991), pp. 834–834. DOI: 10.1118/1.596734. eprint: https://aapm.onlinelibrary.wiley.com/doi/pdf/10.1118/1.596734.

[38] Kresimir Franjic and R J Dwayne Miller. "Vibrationally excited ultrafast thermodynamic phase transitions at the water/air interface." In: *Physical Chemistry Chemical Physics* 12.20 (2010), p. 5225. ISSN: 1463-9076. DOI: 10.1039/c000359j.

[39] Albert Einstein. "Zur Quantentheorie der Strahlung." In: *Physikalische Zeitschrift* 18 (1917), pp. 121–128.

[40] Max Planck. "Zur Theorie des Gesetzes der Energieverteilung im Normalspektrum." In: *Verhandlungen der Deutschen Physikalischen Gesselschaft* 2 (1900), p. 237.

[41] H. Kogelnik and T Li. "Laser Beams and Resonators." In: *Applied Optics* 5.10 (1966), p. 1550. ISSN: 0003-6935. DOI: 10.1364/AO.5.001550.

[42] Anthony Siegman. *LASERS*. University Science Books, 1986, p. 1304. ISBN: 0-935702-11-5.

[43] Walter Koechner. *Solid-state laser engineering*. 6th ed. Springer Berlin Heidelberg, 2006. ISBN: 0-387-29094-X.

[44] W Koechner. "Thermal Lensing in a Nd:YAG Laser Rod." In: *Applied optics* 9.11 (1970), pp. 2548–2553. ISSN: 0003-6935. DOI: 10.1364/AO.9.002548.

[45] M. E. Innocenzi, H. T. Yura, C. L. Fincher, and R. a. Fields. "Thermal modeling of continuous-wave end-pumped solid-state lasers." In: *Applied Physics Letters* 56.1990 (1990), pp. 1831–1833. ISSN: 00036951. DOI: 10.1063/1.103083.

[46] T.Y. Fan. "Heat generation in Nd:YAG and Yb:YAG." In: *IEEE Journal of Quantum Electronics* 29.6 (1993), pp. 1457–1459. ISSN: 0018-9197. DOI: 10.1109/3.234394.

[47] M Born and E Wolf. *Principles of Optics*. 7th ed. Cambridge University Press, 1999.

[48] Y F Chen, Associate Member, T M Huang, C F Kao, C L Wang, and S C Wang. "Optimization in Scaling Fiber-Coupled Laser-Diode End-Pumped Lasers to Higher Power : Influence of Thermal Effect." In: 33.8 (1997), pp. 1424–1429.

[49] Shuzhen Fan, Xingyu Zhang, Qingpu Wang, Shutao Li, Shuanghong Ding, and Fufang Su. "More precise determination of thermal lens focal length for end-pumped solid-state lasers." In: *Optics Communications* 266 (2006), pp. 620–626. ISSN: 00304018. DOI: 10.1016/j.optcom.2006.05.023.

[50] RW Hellwarth. "Control of fluorescent pulsations." In: *Advances in Quantum Electronics*. 1961, p. 334.

[51] F J McClung and R W Hellwarth. "Giant Optical Pulsations from Ruby." In: *Applied Optics* 1.S1 (1962), p. 103. ISSN: 0003-6935. DOI: 10.1364/AO.1.S1.000103.

[52] F.J. McClung and R.W. Hellwarth. "Characteristics of giant optical pulsations from ruby." In: *Proceedings of the IEEE* 51.1 (1963), pp. 46–53. ISSN: 0018-9219. DOI: 10.1109/PROC.1963.1657.

[53] William G. Wagner and Bela A. Lengyel. "Evolution of the Giant Pulse in a Laser." In: *Journal of Applied Physics* 34.7 (1963), pp. 2040–2046. ISSN: 0021-8979. DOI: 10.1063/1.1729732. arXiv: 1011.1669v3.

[54] J. J. Zayhowski and P. L. Kelley. "Optimization of Q-Switched Lasers." In: *IEEE Journal of Quantum Electronics* 27.9 (1991), pp. 2220–2225. ISSN: 15581713. DOI: 10.1109/3.135181.

[55] J.J. Degnan. "Theory of the optimally coupled Q-switched laser." In: *IEEE Journal of Quantum Electronics* 25.2 (1989), pp. 214–220. ISSN: 00189197. DOI: 10.1109/3.16265.

[56] B Braun, F X Kärtner, G Zhang, M Moser, and U Keller. "56-ps passively Q-switched diode-pumped microchip laser." In: *Optics letters* 22.6 (1997), pp. 381–383. ISSN: 0146-9592. DOI: 10.1364/OL.22.000381.

[57] G. J. Spühler, R. Paschotta, R. Fluck, B. Braun, M. Moser, G. Zhang, E. Gini, and U. Keller. "Experimentally confirmed design guidelines for passively Q-switched microchip lasers using semiconductor saturable absorbers." In: *Journal of the Optical Society of America B* 16.3 (1999), p. 376. ISSN: 0740-3224. DOI: 10.1364/JOSAB.16.000376.

[58] Alex C. Butler, David J. Spence, and David W. Coutts. "Scaling Q-switched microchip lasers for shortest pulses." In: *Applied Physics B* 109.1 (2012), pp. 81–88. ISSN: 0946-2171. DOI: 10.1007/s00340-012-5223-2.

[59] G J Spühler, R Paschotta, M P Kullberg, M Graf, M Moser, E Mix, G Huber, C Harder, and U Keller. "A passively Q-switched Yb: YAG microchip laser." In: *Applied Physics B* 72.3 (2001), pp. 285–287.

[60] Shouhuan Zhou, Shiqun Li, K. K. Lee, and Y. C. Chen. "Monolithic self-Q-switched Cr,Nd:YAG laser." In: *Optics Letters* 18.7 (1993), p. 511. ISSN: 0146-9592. DOI: 10.1364/OL.18.000511.

[61] P Wang, Shou-huan Zhou, K.K Lee, and Y.C Chen. "Picosecond laser pulse generation in a monolithic self-Q-switched solid-state laser." In: *Optics Communications* 114.5-6 (1995), pp. 439–441. ISSN: 00304018. DOI: 10.1016/0030-4018(94)00647-D.

[62] J J Zayhowski and C Dill Iii. "Diode-pumped passively Q-switched picosecond microchip lasers." In: *Optics letters* 19.18 (1994), pp. 1427–1429. ISSN: 0146-9592. DOI: 10.1364/OL.19.001427.

[63] John J Zayhowski. "Passively Q-Switched Microchip Lasers and Applications." In: *The Review of Laser Engineering* 26.12 (1998), pp. 841–846. ISSN: 0387-0200. DOI: 10.2184/lsj.26.841.

[64] B. C. Stuart, M. D. Feit, A. M. Rubenchik, B. W. Shore, and M. D. Perry. "Laser-Induced Damage in Dielectrics with Nanosecond to Subpicosecond Pulses." In: *Physical Review Letters* 74.12 (1995), pp. 2248–2251. ISSN: 0031-9007. DOI: 10.1103/PhysRevLett.74.2248.

[65] John J. Degnan, D. Barry Coyle, and Richard B. Kay. "Effects of thermalization on Q-switched laser properties." In: *IEEE Journal of Quantum Electronics* 34.5 (1998), pp. 887–899. ISSN: 00189197. DOI: 10.1109/3.668777.

[66] Alexander A. Kaminskii. *Laser Crystals*. Vol. 14. 1990, p. 457. ISBN: 978-3-540-52026-9. DOI: 10.1007/978-3-540-70749-3.

[67] Camille Bibeau, Stephen a. Payne, and Howard T. Powell. "Direct measurements of the terminal laser level lifetime in neodymium-doped crystals and glasses." In: *Journal of the Optical Society of America B* 12.10 (1995), p. 1981. ISSN: 0740-3224. DOI: 10.1364/JOSAB.12.001981.

[68] Fan Tso Yee. "Effect of finite lower level lifetime on Q-switched lasers." In: *IEEE Journal of Quantum Electronics* 24.12 (1988), pp. 2345–2349. ISSN: 00189197. DOI: 10.1109/3.14358.

[69] SP Ng, DY Tang, LJ Qian, and LJ Qin. "Satellite Pulse Generation in Diode-Pumped Passively Q-Switched Nd:$GdVO_4$ Lasers." In: *IEEE Journal of Quantum Electronics* 42.7 (2006), pp. 625–632. ISSN: 0018-9197. DOI: 10.1109/JQE.2006.875866.

[70] D. E. McCumber and M. D. Sturge. “Linewidth and Temperature Shift of the R Lines in Ruby.” In: *Journal of Applied Physics* 34.6 (1963), pp. 1682–1684. ISSN: 0021-8979. DOI: 10.1063/1.1702657.

[71] Takashi Kushida. “Linewidths and Thermal Shifts of Spectral Lines in Neodymium-Doped Yttrium Aluminum Garnet and Calcium Fluorophosphate.” In: *Physical Review* 185.2 (1969), pp. 500–508. ISSN: 0031-899X. DOI: 10.1103/PhysRev.185.500.

[72] Yoichi Sato, Hideki Ishizuki, and Takunori Taira. “Novel Model of Thermal Conductivity for Optical Materials.” In: *The Review of Laser Engineering* 36.APLS (2008), pp. 1081–1084. ISSN: 0387-0200. DOI: 10.2184/lsj.36.1081.

[73] Yoichi Sato and Takunori Taira. “Temperature dependencies of stimulated emission cross section for Nd-doped solid-state laser materials.” In: *Optical Materials Express* 2.8 (2012), p. 1076. ISSN: 2159-3930. DOI: 10.1364/OME.2.001076.

[74] Y. Mao, P. Deng, and F. Gan. “Concentration and temperature dependence of spectroscopic properties of highly-doped Nd:YAG crystal grown by temperature gradient technique (TGT).” In: *Physica Status Solidi (A) Applied Research* 193.2 (2002), pp. 329–337. ISSN: 00318965. DOI: 10.1002/1521-396X(200209)193:2<329::AID-PSSA329>3.0.CO;2-8.

[75] AG Okhrimchuk and AV Shestakov. “Performance of YAG: Cr4+ laser crystal.” In: *Optical Materials* 3.1 (1994), pp. 1–13. ISSN: 09253467. DOI: 10.1016/0925-3467(94)90023-X.

[76] J Bartschke, K.-J. Boller, R Wallenstein, I. V. Klimov, V. B. Tsvetkov, and I. A. Shcherbakov. “Diode-pumped passively Q-switched self-frequency-doubling Nd:YAB laser.” In: *Journal of the Optical Society of America B* 14.12 (1997), p. 3452. ISSN: 0740-3224. DOI: 10.1364/JOSAB.14.003452.

[77] Linquan Niu, Cunxiao Gao, Shaolan Zhu, Chuandong Sun, and Haodong He. “Single-and dual-pulse oscillation in a passively Q-switched Nd: YAG microchip laser.” In: *Optics express* 19.21 (2011), pp. 20628–20633.

[78] Ping Li, Teng Song, Jinxi Bai, Yangyang Dun, and Xiaohan Chen. “Research of multi-pulses emission in passively Q-switched Nd 3+ :YAG microchip laser.” In: *Optik - International Journal for Light and Electron Optics* 132 (2017), pp. 39–45. ISSN: 00304026. DOI: 10.1016/j.ijleo.2016.12.006.

[79] Jun Dong and Ken-ichi Ueda. "Longitudinal-mode competition induced instabilities of Cr4+,Nd3+:Y3Al5O12 self-Q-switched two-mode laser." In: *Applied Physics Letters* 87.15 (2005), p. 151102. ISSN: 0003-6951. DOI: 10.1063/1.2089153.

[80] J. Dong, A. Shirakawa, and K. Ueda. "Switchable pulses generation in passively Q-switched multilongitudinal-mode microchip laser." In: *Laser Physics Letters* 4.2 (2007), pp. 109–116. ISSN: 16122011. DOI: 10.1002/lapl.200610077.

[81] Tim Kellner. "Nd-dotierte Grundzustandslaser : Frequenzverdopplung im kontinuierlichen und modensynchronisierten Betrieb." Dissertation. Universität Hamburg, 1999.

[82] Jonathan E Guyer, Daniel Wheeler, and James A Warren. "FiPy: Partial Differential Equations with Python." In: *Computing in Science & Engineering* 11.3 (2009), pp. 6–15. ISSN: 1521-9615. DOI: 10.1109/MCSE.2009.52.

[83] John J Zayhowski, Colby Dill III, Chris Cook, and John L Daneu. "Mid- and High-Power Passively Q-Switched Microchip Lasers." In: *Advanced Solid State Lasers*. Vol. 26. Washington, D.C.: OSA, 2001, TuC1. DOI: 10.1364/ASSL.1999.TuC1.

[84] Jun Dong, Ken-ichi Ueda, and Peizhi Yang. "Multi-pulse oscillation and instabilities in microchip self-Q-switched transverse-mode laser." In: *Optics express* 17.19 (2009), pp. 16980–16993. ISSN: 1094-4087. DOI: 10.1364/OE.17.016980.

[85] A. Agnesi, P. Dallocchio, F. Pirzio, and G. Reali. "Sub-nanosecond single-frequency 10-kHz diode-pumped MOPA laser." In: *Applied Physics B* 98.4 (2010), pp. 737–741. ISSN: 0946-2171. DOI: 10.1007/s00340-009-3813-4.

[86] Jun Dong, Ken-Ichi Ueda, Akira Shirakawa, Hideki Yagi, Takagimi Yanagitani, and Alexander a Kaminskii. "Composite Yb:YAG/Crˆ4+:YAG ceramics picosecond microchip lasers." In: *Optics Express* 15.22 (2007), p. 14516. ISSN: 1094-4087. DOI: 10.1364/OE.15.014516.

[87] Igor Martial, François Balembois, Julien Didierjean, and Patrick Georges. "Nd:YAG single-crystal fiber as high peak power amplifier of pulses below one nanosecond." In: *Optics Express* 19.12 (2011), p. 11667. ISSN: 1094-4087. DOI: 10.1364/OE.19.011667.

[88] Aleksej M. Rodin, Aidas Aleknavicius, Andrejus Michailovas, and Aleksandr S. Dementjev. “Beam quality investigation in Nd:YAG crystal fiber amplifier pumped at >110w.” In: *Proceedings of SPIE - The International Society for Optical Engineering*. Ed. by W. Andrew Clarkson and Ramesh K. Shori. Vol. 9342. 2015, p. 934207. ISBN: 9781628414325. DOI: 10.1117/12.2079294.

[89] B. C. Stuart, M. D. Feit, S. Herman, A. M. Rubenchik, B. W. Shore, and M. D. Perry. “Nanosecond-to-femtosecond laser-induced breakdown in dielectrics.” In: *Physical Review B* 53.4 (1996), pp. 1749–1761. ISSN: 0163-1829. DOI: 10.1103/PhysRevB.53.1749.

[90] Lee M. Frantz and John S. Nodvik. “Theory of Pulse Propagation in a Laser Amplifier.” In: *Journal of Applied Physics* 34.8 (1963), pp. 2346–2349. DOI: 10.1063/1.1702744. eprint: https://doi.org/10.1063/1.1702744.

[91] Petras V. Avizonis and Ronald L. Grotbeck. “Experimental and Theoretical Ruby Laser Amplifier Dynamics.” In: *Journal of Applied Physics* 37.2 (1966), pp. 687–693. ISSN: 0021-8979. DOI: 10.1063/1.1708238.

[92] J. Dong, A. Shirakawa, S. Huang, Y. Feng, K. Takaichi, M. Musha, Kenichi Ueda, and A. A. Kaminskii. “Stable laser-diode pumped microchip sub-nanosecond Cr,Yb:YAG self-Q-switched laser.” In: *Laser Physics Letters* 2.8 (2005), pp. 387–391. ISSN: 1612-2011. DOI: 10.1002/lapl.200510018.

[93] Y. Kalisky, A. Ben-Amar Baranga, Y. Shimony, Z. Burshtein, S.A. Pollack, and M.R. Kokta. “Cr4+ doped garnets: their properties as non-linear absorbers.” In: *Optical Materials* 6.4 (1996), pp. 275–280. ISSN: 09253467. DOI: 10.1016/S0925-3467(96)00053-5.

[94] Z. Burshtein, P. Blau, Y. Kalisky, Y. Shimony, and M. R. Kokta. “Excited-state absorption studies of Cr4+ ions in several garnet host crystals.” In: *IEEE Journal of Quantum Electronics* 34.2 (1998), pp. 292–299. ISSN: 00189197. DOI: 10.1109/3.658716.

[95] B. Lipavsky, Y. Kalisky, Z. Burshtein, Y. Shimony, and S. Rotman. “Some optical properties of Cr4+-doped crystals.” In: *Optical Materials* 13.1 (1999), pp. 117–127. ISSN: 09253467. DOI: 10.1016/S0925-3467(99)00020-8.

[96] Guohua Xiao, Jin Hong Lim, Sidney Yang, Eric Van Stryland, Michael Bass, and Lou Weichman. “Z-scan measurement of the ground and excited state absorption cross sections of Cr4+ in yttrium aluminum garnet.” In:

IEEE Journal of Quantum Electronics 35.7 (1999), pp. 1086–1091. ISSN: 00189197. DOI: 10.1109/3.772180.

[97] Alphan Sennaroglu, Umit Demirbas, Sarper Ozharar, and Fatih Yaman. "Accurate determination of saturation parameters for Cr^4+-doped solid-state saturable absorbers." In: *Journal of the Optical Society of America B* 23.2 (2006), p. 241. ISSN: 0740-3224. DOI: 10.1364/JOSAB.23.000241.

[98] Masaki Tsunekane and Takunori Taira. "Direct measurement of temporal transmission distribution of a saturable absorber in a passively Q-switched laser." In: *IEEE Journal of Quantum Electronics* 52.5 (2016). ISSN: 00189197. DOI: 10.1109/JQE.2016.2541922.

[99] G. Arisholm, R. Paschotta, and T. Sudmeyer. "Limits to the power scalability of high-gain optical parametric oscillators and amplifiers." In: *Conference on Lasers and Electro-Optics Europe - Technical Digest* 21.3 (2003), p. 262. ISSN: 0740-3224. DOI: 10.1109/CLEOE.2003.1312323.

[100] N.M. Wannop, M.R. Dickinson, a. Charlton, and T.a. King. "Q-switching the Erbium-YAG Laser." In: *Journal of Modern Optics* 41.December 2014 (1994), pp. 2043–2053. ISSN: 0950-0340. DOI: 10.1080/09500-349414-551921.

[101] E. a. Arbabzadah, C. C. Phillips, and M. J. Damzen. "Free-running and Q-switched operation of a diode pumped Er:YSGG laser at the 3 μm transition." In: *Applied Physics B* 111 (2013), pp. 333–339. ISSN: 0946-2171. DOI: 10.1007/s00340-013-5337-1.

[102] Serban Georgescu, Octavian Toma, and H. Totia. "Intrinsic limits of the efficiency of erbium 3um lasers." In: *IEEE Journal of Quantum Electronics* 39.6 (2003), pp. 722–732. ISSN: 00189197. DOI: 10.1109/JQE.2003.811598.

[103] S. Maier, N.-O. Hansen, S. Kruber, T. Gosau, D. Eggert, A. Gliese, H. Petersen, H. Schlüter, and R. J. D. Miller. "Wound Healing Study and Ablation Rate Measurements with the Novel Picosecond Infrared Laser (PIRL)." In: *Conference on Lasers and Electro-Optics*. Optical Society of America, 2017, ATu3A.5. DOI: 10.1364/CLEO_AT.2017.ATu3A.5.

[104] M. Wurlitzer, E. Hessling, K. Rinas, M. Fuh, Dr. H. Petersen, Dr. F. Ricklefs, Dr. K. Lamszus, Dr. J. Regelsberger, S. Maier, S. Kruber, Dr. N. Hansen, Dr. RJ D. Miller, and Dr. H. Schlüter. "Mass Spectrometric Lipid Profiles of Picosecond Infrared Laser Generated Tissue Aerosols Discrim-

inate Different Brain Areas." In: *Journal of Lipid Research* (submitted 2018).

[105] Frederik Busse, Sebastian Kruber, Wesley D Robertson, and R J Dwayne Miller. "Digital Interference Microscopy and Density Reconstruction of Picosecond Infrared Laser Desorption at the Water-Air Interface." In: *Journal of Applied Physics* (submitted 2018).

[106] R.J. Dwayne Miller, Stephanie Maier, Sebastian Kruber, and Nils-Owe Hansen. *Laser Surgery Apparatus For Contact Laser Surgery*. 2017, EP3067005B1.

[107] J. A. Fülöp, Zs Major, A. Henig, S. Kruber, R. Weingartner, T. Clausnitzer, E-B Kley, A. Tünnermann, V. Pervak, A. Apolonski, J. Osterhoff, R. Hörlein, F. Krausz, and S. Karsch. "Short-pulse optical parametric chirped-pulse amplification for the generation of high-power few-cycle pulses." In: *New Journal of Physics* 9.12 (2007), pp. 438–438. DOI: 10.1088/1367-2630/9/12/438.

[108] Marvin Weber. *Handbook of Optical Materials*. Vol. 19. 2002. ISBN: 978-0-8493-3512-9. DOI: 10.1201/9781420050196.

[109] Linus Pauling and M. D. Shappell. "8. The Crystal Structure of Bixbyite and the C-Modification of the Sesquioxides." In: *Zeitschrift für Kristallographie - Crystalline Materials* 75.1 (1930). ISSN: 2196-7105. DOI: 10.1515/zkri-1930-0109.

[110] Frank Träger, ed. *Springer Handbook of Lasers and Optics*. New York, NY: Springer New York, 2007. ISBN: 978-0-387-95579-7. DOI: 10.1007/978-0-387-30420-5.

[111] Shuxian Wang, Hengjiang Cong, Kui Wu, Zhongben Pan, Haohai Yu, Junhai Liu, Robert I. Boughton, and Huaijin Zhang. "Composition characterization in YSGG garnet single crystals for ytterbium laser." In: *Optical Materials Express* 3.9 (2013), p. 1408. ISSN: 2159-3930. DOI: 10.1364/OME.3.001408.

[112] Ramona Becker, Helga Hartwig, Herbert Köppe, Hans Vanecek, Paul Velić, Rudolf Warncke, and Anna Zelle. *Gmelin Handbuch der Anorganischen Chemie*. Ed. by Rudolf Warncke. Vol. 976. Berlin, Heidelberg: Springer Berlin Heidelberg, 1978. ISBN: 978-3-662-06226-5. DOI: 10.1007/978-3-662-06224-1.

[113] Thomas Jensen. "Upconversion-Prozesse und Wirkungsquerschnitte in Er3+ dotierten 3um Flourid- und Granat-Lasern, gepumpt mit cw und quasi-cw Dioden-Arrays." PhD thesis. Universität Hamburg, 1996.

[114] Eric Mix. "Kristallzüchtung , Spektroskopie und Lasereigenschaften Yb-dotierter Sesquioxide." PhD thesis. Universität Hamburg, 1999.

[115] Sebastian Bär. *Crystalline Rare Earth Doped Sesquioxide PLD-films on A-alumina [alpha-alumina]: Preparation and Characterization*. Cuvillier Verlag, 2004.

[116] J. P. Hurrel. "Optical Phonons of Yttrium Aluminum Garnet." In: *Physical Review* 173.3 (1968), pp. 851–856. DOI: 10.1103/PhysRev.173.851.

[117] D E Zelmon, D L Small, and R Page. "Refractive-Index Measurements of Undoped Yttrium Aluminum Garnet from 0.4 to 5.0 mum." In: *Applied optics* 37.21 (1998), pp. 4933–4935. ISSN: 0003-6935. DOI: 10.1364/AO.37.004933.

[118] Dhiraj K. Sardar, William M. Bradley, John J. Perez, John B. Gruber, Bahram Zandi, J. Andrew Hutchinson, C. Ward Trussell, and Milan R. Kokta. "Judd-Ofelt analysis of the Er3+ (4f11) absorption intensities in Er3+ doped garnets." In: *Journal of Applied Physics* 93.2003 (2003). ISSN: 00218979. DOI: 10.1063/1.1543242.

[119] Norman P. Barnes and Donald J. Gettemy. "Temperature variation of the refractive indices of yttrium lithium fluoride." In: *Journal of the Optical Society of America* 70.10 (1980), p. 1244. ISSN: 0030-3941. DOI: 10.1364/JOSA.70.001244.

[120] David E Zelmon, Jessica M Northridge, Nicholas D Haynes, Dan Perlov, and Klaus Petermann. "Temperature-dependent Sellmeier equations for rare-earth sesquioxides." In: *Appl. Opt.* 52.16 (2013), pp. 3824–3828. ISSN: 15394522. DOI: 10.1364/AO.52.003824.

[121] R. L. Aggarwal, D. J. Ripin, J. R. Ochoa, and T. Y. Fan. "Measurement of thermo-optic properties of Y3Al5O12, Lu3Al5O12, YAIO3, LiYF4, LiLuF4, BaY2F8, KGd(WO4)2, and KY(WO4)2 laser crystals in the 80–300 K temperature range." In: *Journal of Applied Physics* 98.10 (2005), p. 103514. ISSN: 00218979. DOI: 10.1063/1.2128696.

Eidesstattliche Versicherung / Declaration on oath

Hiermit versichere ich an Eides statt, die vorliegende Dissertationsschrift selbst verfasst und keine anderen als die angegebenen Hilfsmittel und Quellen benutzt zu haben.

Die eingereichte schriftliche Fassung entspricht der auf dem elektronischen Speichermedium.

Die Dissertation wurde in der vorgelegten oder einer ähnlichen Form nicht schon einmal in einem früheren Promotionsverfahren angenommen oder als ungenügend beurteilt.

Hamburg, den 24.05.2018

Sebastian Kruber